UNIVERSITÀ DEGLI STUDI DI PADOVA

UNIVERSITA' DEGLI STUDI DI PADOVA

Department of Industrial Engineering

Master's degree course in Electrical Engineering

Development and Validation of Impedance Matching Adapters for Magnetic Diagnostics in Fusion Plasma Devices

Supervisor:
Ing. Nicolò Marconato
Co-Supervisor:
Dott. Roberto Cavazzana

Candidate:
Gianluca Gallio (mat. 2156482)

Academic Year 2025/2026

CONSORZIO RFX
Ricerca Formazione Innovazione

To Crash,

my brother of a different species.

Abstract

Magnetic measurements are a fundamental element for the operation of current experimental devices and future commercial fusion reactors. High-performance plasma control requires signal precision and noise immunity. This thesis project focuses on the dimensioning, design, and laboratory characterization of specialized line termination adapters. These components are extremely critical for ensuring signal integrity throughout the entire measurement chain, comprising magnetic sensors (probes), long-distance transmission lines, and front-end acquisition electronics. The activity will involve in modeling and simulating the transmission line behavior, design the matching network, with experimental validation through laboratory testing of the full measurement chain.

This dissertation is basically divided into two main parts: a first, more theoretical, introduction and a second, more practical, description of the laboratory experience.

The first chapter is a concise recall on plasma physics, eventually introducing also the main aspects of nuclear fusion and plasma instabilities during discharge. The second and third chapters explain the function of the two main components in magnetic measurements and their application in fusion devices: inductive sensors and integrators, respectively.

The fourth chapter, which effectively starts the second part of the thesis, shows the measured impedance values of the transmission line and the inductance values of the coils, after discussing the importance of impedance matching. The fifth chapter is on the electrical design of the adapter circuits for the entire acquisition chains. Finally, the sixth chapter is a demonstration of the function of the digital integrator and answers why it is mandatory.

A summary of the experimental results is reported in the concluding chapter.

Contents

List of Figures

List of Tables

Chapter 1

Elements of nuclear fusion

1.1 Plasma physics

A plasma [1] is a collection of free charged particles moving in random directions that is, on the average, electrically neutral. They are often called a "*fourth state of matter*". At a sufficiently high temperature, the molecules in a gas decompose to form a gas of atoms that move freely in random directions, except for infrequent collisions between atoms. If the temperature is further increased, the atoms decompose into freely moving charged particles and the substance enters the plasma state.
This state is characterized by a common charged particle density $n_e \approx n_i \approx n$ (which unit of measure is in particles/m^3) and an equilibrium temperature $T_e = T_i = T$, where the required temperature in order to form a plasma spans from 4000 K for easy-to-ionize elements like cesium to 20000 K for hard-to-ionize elements like helium.
Let us consider a plasma composed by the same type of neutral particles, ions and electrons, the ionization state of a gas in thermal equilibrium is described by the Saha ionization equation [2]:

$$f(T) = \frac{n_e n_i}{n_n} = \frac{2(2\pi m_e T)^{3/2}}{h^3} \exp\left(-\frac{E_i}{T}\right) = 3 \times 10^{27} T^{3/2} \exp\left(-\frac{E_i}{T}\right) \tag{1.1}$$

where n_e, n_i, n_n are the densities of each particle in m^{-3} and E_i is the ionizing energy for atoms in eV (the same unit of measure is also used for the temperature T).
If we indicate with $n_0 = n_i + n_n$ the total density for heavy particles, the ionization parameter is defined:

$$\chi = \frac{n_e}{n_i + n_n} = \frac{n_e}{n_0} \tag{1.2}$$

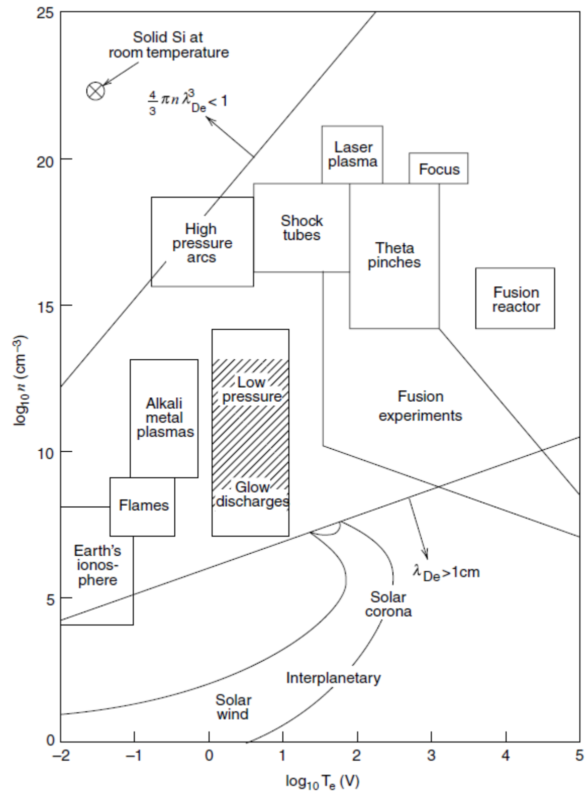

Figure 1.1: Space and laboratory plasmas on a $\log n$ versus $\log T_e$ diagram.

1.1.1 Debye length

The characteristic length scale in a plasma is the electron Debye length λ_{De}, which is the distance scale over which significant charge densities can spontaneously exist.

Let us introduce a sheet of negative charge having surface charge density $\rho_S < 0\ \frac{C}{m^2}$ into an infinitely extended plasma having equilibrium densities $n_e = n_i = n_0$: a perturbation is introduced as the negative sheet repels all the nearby electrons, leading to a reduction of electron density near the sheet. The potential and density variation can be described with the Poisson's equation:

$$\frac{d^2\Phi}{dx^2} = -\frac{e}{\varepsilon_0}(n_i - n_e) = \frac{en_0}{\varepsilon_0}\left(e^{\Phi/T_e} - 1\right) \tag{1.3}$$

where $n_e = n_0 \exp(\Phi/T_e)$ comes from the Boltzmann relation.

The term $\exp(\Phi/T_e)$ can be expanded in a Taylor series to the lowest order for $\Phi \ll T_e$, thus

$$\frac{d^2\Phi}{dx^2} = \frac{en_0}{\varepsilon_0}\frac{\Phi}{T_e} \tag{1.4}$$

which symmetric solution is

$$\Phi = \Phi_0 e^{-|x|/\lambda_{De}} \tag{1.5}$$

where

$$\lambda_{De} = \sqrt{\frac{\varepsilon_0 T_e}{e n_0}} \approx 743 \sqrt{\frac{T_e}{n_e}} \quad [cm] \tag{1.6}$$

Then, the Debye number, which is the average number of electrons in a plasma contained within a sphere of Debye length radius, can be defined:

$$N_{De} = \frac{4\pi}{3} n_e \lambda_{De}^3 = \frac{1}{3}\Lambda \tag{1.7}$$

where the dimensionless quantity $\Lambda = 4\pi n_e \lambda_{De}^3$ is called plasma parameter.

1.2 Fusion reactions

The thermonuclear fusion [3] consists in a reaction between two light nuclei (isotopes of hydrogen, helium or lithium are typically considered) in order to form a nucleus heavier than the starting ones. It is an exoenergetic[1] process since the total rest mass of the reacting nuclei is greater than that of the reaction products, including any particles released by the reaction itself, and the difference in mass is transformed into energy, which is the kinetic energy of the reaction products.
Several fusion reactions can in principle be exploited, but most relevant reactions use a mixture which includes deuterium (${}^2_1$H or D), a virtually infinite fuel source, and tritium (${}^3_1$H or T), both isotopes of hydrogen.

Fusion reaction	Probability
$\mathrm{D} + \mathrm{D} \longrightarrow {}^3\mathrm{He} + \mathrm{n} + 3.27\,\mathrm{MeV}$	50 %
$\mathrm{D} + \mathrm{D} \longrightarrow \mathrm{T} + \mathrm{p} + 4.03\,\mathrm{MeV}$	50 %
$\mathrm{D} + \mathrm{T} \longrightarrow \mathrm{He}^{2+} + \mathrm{n}$	100 %
$\mathrm{D} + {}^3\mathrm{He} \longrightarrow \mathrm{He}^{2+} + \mathrm{p} + 18.3\,\mathrm{MeV}$	100 %

Table 1.1: Most relevant fusion reactions and their branch probabilities.

In order for a fusion reaction to take place, two nuclei must have enough energy to overcome the repulsive Coulomb force acting between the nuclei, because of their positive charge. A fundamental parameter for the analysis of nuclear reactions is the cross-section (σ), usually measured in "*barns*"[2], which measures the probability of the reaction per pair of particles: if the incident particle passes through the area σ, then the distance is small enough and the force exerted on it by the target particle is sufficiently strong that a nuclear reaction takes place.

[1] That releases energy to its environment
[2] $1\ b = 10^{-28}\ m^2$.

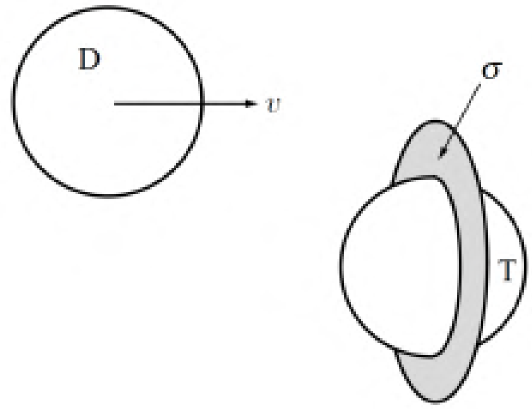

Figure 1.2: Graphical representation of the cross-section σ, where D is the projectile particle and T the target particle.

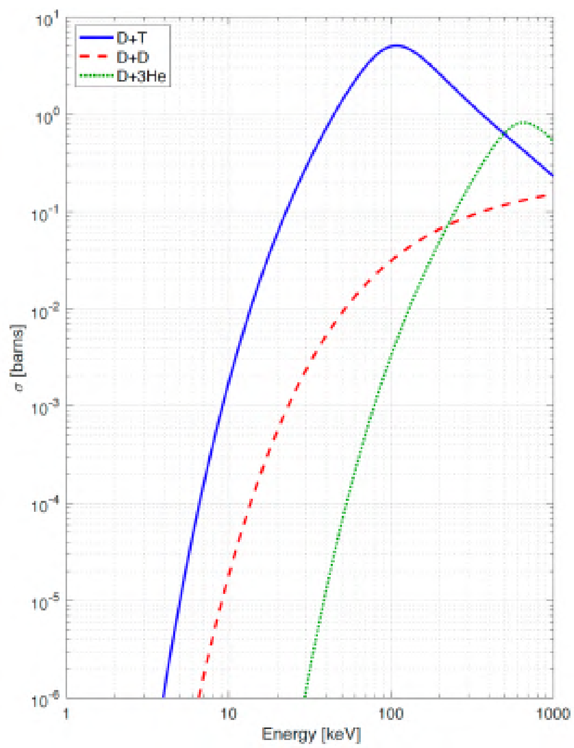

Figure 1.3: Cross-section in function of the particle energy of three different types of fusion reactions.

1.2.1 Lawson criterion

A simple and widely used index of thermonuclear gain is provided by the Lawson criterion [4]: it compares the rate of energy being generated by fusion reactions to the rate of energy losses to the environment. When the rate of production is higher than the rate of loss, the system will become self-sustaining (or "*ignited*") and it will produce net energy.

Let us consider the thermonuclear power per unit volume generated by a D-T reactor and assume to be in steady state conditions: the fusion power associated to the alpha particles is large enough to balance bremsstrahlung and transport losses without any auxiliary power. So, the power balance is

$$p_{\alpha}^{DT} = p_{transport} + p_{bremsstrahlung} \tag{1.8}$$

Expanding the terms

$$\frac{n^2}{4} \langle \sigma v \rangle E_{\alpha} = \frac{3k_B nT}{\tau_E} + c_{brems} n^2 Z^2 \sqrt{T} \tag{1.9}$$

and substituting with numerical values

$$1.4 \times 10^{-13} n^2 \langle \sigma v \rangle = 4.8 \times 10^{-16} \frac{nT}{\tau_E} + 5.35 \times 10^{-37} n^2 Z^2 \sqrt{T} \quad \left[\frac{W}{m^3}\right] \tag{1.10}$$

where $\langle \sigma v \rangle$ is the reactivity and τ_E the energy confinement time.

The Lawson criterion for ignition is obtained:

$$n\tau_E > \frac{4.8T}{1.4 \times 10^3 \langle \sigma v \rangle - 5.35 \times 10^{-37} Z^2 \sqrt{T}} \tag{1.11}$$

It is known that the reactivity in the case of D-T mixture fuel (a 50/50 mixture is typically used) is $\langle \sigma v \rangle_{DT} \approx 1.1 \times 10^{-24} T^2$, and so, substituting the value in the ignition condition and neglecting the bremsstrahlung losses term, the triple product is obtained:

$$n\tau_E T \approx 3.12 \times 10^{21} \quad \left[\frac{keV \cdot s}{m^3}\right] \tag{1.12}$$

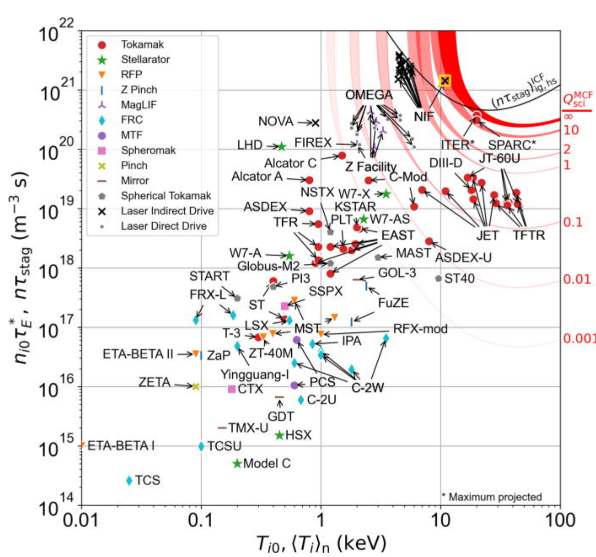

Figure 1.4: The Lawson criterion for ignition in different fusion reactors [5].

1.2.2 Plasma confinement

Hot plasmas have to be kept from contact with walls so that from the outset magnetic fields have been used to contain plasma in controlled thermonuclear fusion experiments. No material can withstand contact with such an energetic plasma, in case of contact the walls are sputtered, releasing impurities inside the plasma that lead to radiation losses, and plasma cools down.
In gravitational confinement the charged particle confined by gravitation, so it is possible only in stars, while in inertial confinement a small solid pellet of deuterium or tritium fuel, which is rapidly heated up by high power light lasers, expanding over a period determined by the mass of the fuel ions.
The most developed and promising approach is the magnetic confinement fusion (MCF), which utilizes the electromagnetic behavior of charged plasma particles to confine them within a specially designed magnetic field configuration. Charged particles, when immersed in a magnetic field, execute a spiral motion around field lines, thus being confined in the directions perpendicular to the field line. The radius of motion is called Larmor radius:

$$r_L = \frac{mv_\perp}{qB} \tag{1.13}$$

where q is the charge of the particle and $v_\perp = \sqrt{\frac{8T}{\pi m}}$ is the component of its velocity perpendicular to induction magnetic field B. In the radial configuration it is possible to increase the magnetic field at

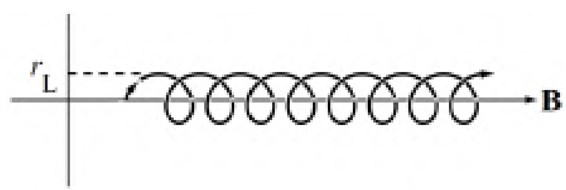

Figure 1.5: Particle confinement along the induction magnetic field line B.

the plasma column ends in order to to reflect the particles at the mirrors, but particles with velocities almost parallel to the magnetic field lines are not confined. The most effective solution is to make the magnetic field close on themselves in order to form a toroidal configuration, so the losses at the extremes of the plasma column are eliminated.
Different components of the magnetic field are involved in the toroidal field configuration:

- the **poloidal field** provides confinement;
- the **toroidal field** provides stability;
- the **additional vertical field** provides equilibrium and shape;
- the **additional radial field** provides shape and stability.

Additional poloidal magnetic field is produced by external coils or by toroidal plasma current.

1.2.3 Plasma heating

A continuous plasma heating [6] is required to balance the radiative and transport losses since a temperature of about 20 keV is required in D-T fusion reactions.

Ohmic heating is the result of passing an electric current through the plasma, which has an intrinsic resistivity. It is particularly effective during the initial phase of plasma formation, helping to increase the thermal energy required. Energy is then dissipated in the form of heat, but as the plasma temperature rises, its resistivity decreases significantly, reducing the efficiency of Ohmic heating.

Neutral Beam Injection heating is also widely used due to its relatively high efficiency: beams of high energy, neutral deuterium or tritium atoms are injected into the plasma, transferring their energy to the plasma via collisions with the plasma ions.

Another method is the Radio-Frequency heating, where external antennas are used to generate electromagnetic waves, of a frequency matched to the ions or electrons, propagating in the plasma.

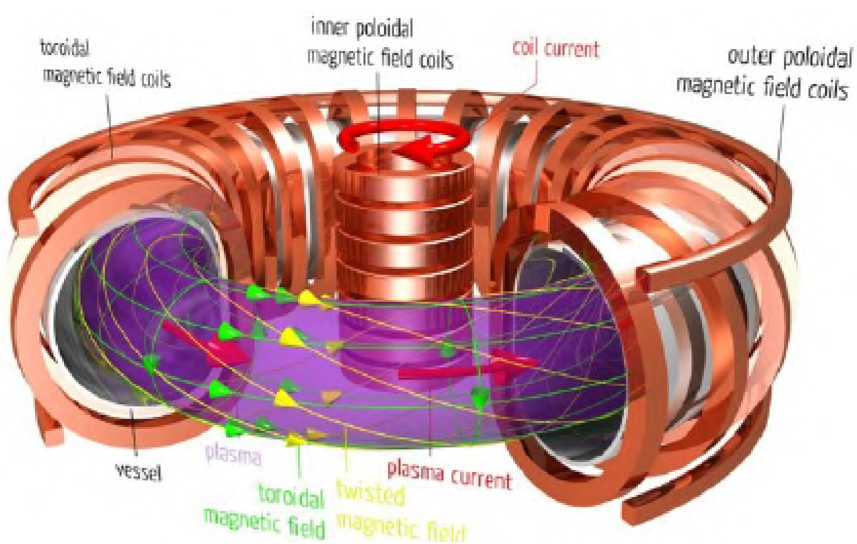

Figure 1.6: Magnetic confinement in the toroidal field configuration.

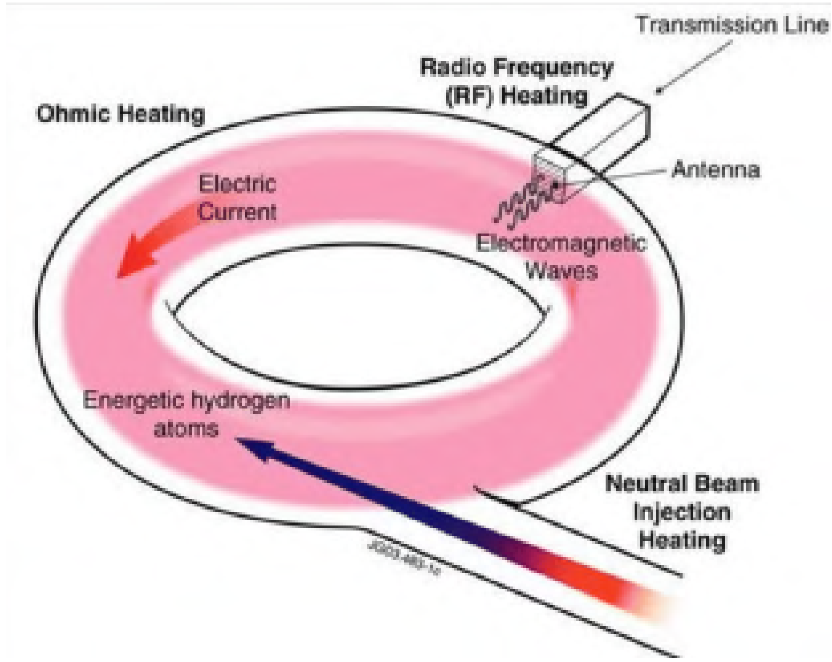

Figure 1.7: Various mechanisms for plasma heating.

1.3 Plasma instabilities

In a toroidal fusion reactor, the plasma is confined by means of a magnetic field. There exist an equilibrium between outward forces due to the pressure gradient in the plasma and inward forces due to the interaction between currents flowing inside the plasma and the magnetic field. The equilibrium magnetic field is characterized by helical field lines that lie on nested toroidal surfaces of constant flux. Plasma instabilities arise because under certain circumstances field lines for which the ratio of the number of toroidal transits to the number of poloidal transits is rational can be easily displaced. Due to finite resistivity the field lines reconnect so that the topology of nested toroidal flux surfaces is changed and nested helical flux surfaces appear. The safety factor [7] represents the number of toroidal transits m of the field lines (called "tearing modes"), for each poloidal transits n on a given magnetic flux surface ψ:

$$q(\psi) = \frac{m}{n} \tag{1.14}$$

Higher values of $q(\psi)$ provide greater stability against tearing modes.

Magnetic instabilities will arise whenever $q(\psi)$ is not a rational number: this means that the field lines will not reconnect on the next turns, resulting in a change of the structure of the flux surface.

Helical structures with nested flux surfaces are thus created, these "magnetic islands" [8] affect radial heat transport profoundly, causing increased heat loss from the plasma such that they are an obstacle in obtaining the high central temperatures needed for fusion. The helical island structures rotate mainly in the toroidal direction because poloidal rotation requires energy to compress and expand them. These structures can sometimes cause a disruption, especially if they lock to external magnetic stray fields.

Knowledge of the precise nature of these modes is essential in improving the performance of tokamaks, for this reason magnetic measures (along with the other diagnostic methods) are necessary in order to evaluate instabilities and reconstruction of plasma equilibrium.

The Grad-Shafranov equation [9] is the equilibrium equation in ideal magnetohydrodynamics (MHD) which describes plasma equilibrium, transport phenomenon and MHD stability in a two dimensional plasma, for example the symmetric toroidal plasma in a Reverse Field Pinch (RFP) device:

$$\Delta^*\psi = R\frac{\partial}{\partial R}\left(\frac{1}{R}\frac{\partial\psi}{\partial R}\right) + \frac{\partial^2\psi}{\partial Z^2} = -\mu_0 R J_\phi = -\mu_0 R^2\frac{\partial P}{\partial\psi} - F\frac{\partial F}{\partial\psi} \tag{1.15}$$

where $\psi(R,Z)$ is the poloidal flux per length unit towards toroidal direction, R is the major radius of the toroid, J_ϕ is the toroidal plasma current density, P is the thermal pressure and F is a flux function associated to the poloidal current in the system [10].

The determination of magnetic equilibrium inside the plasma, using magnetic probes located outside the plasma, can be divided into two parts: by solving the homogeneous Grad-Shafranov equation in the vacuum region surrounding the plasma, the plasma boundary is determined such that the solution matches the measurements, then the complete Grad-Shafranov equation must be solved in the plasma region, such that the solution matches the previous solution at the plasma boundary.

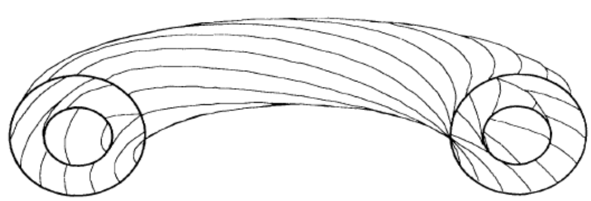

Figure 1.8: Magnetic field lines under ideal equilibrium condition.

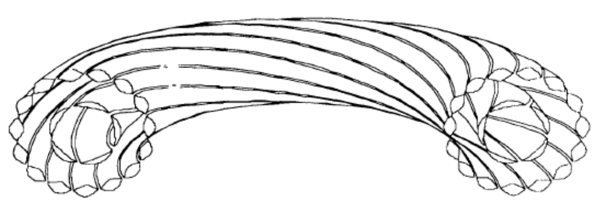

Figure 1.9: Magnetic field lines after a perturbation. Magnetic islands are visible near plasma surfaces.

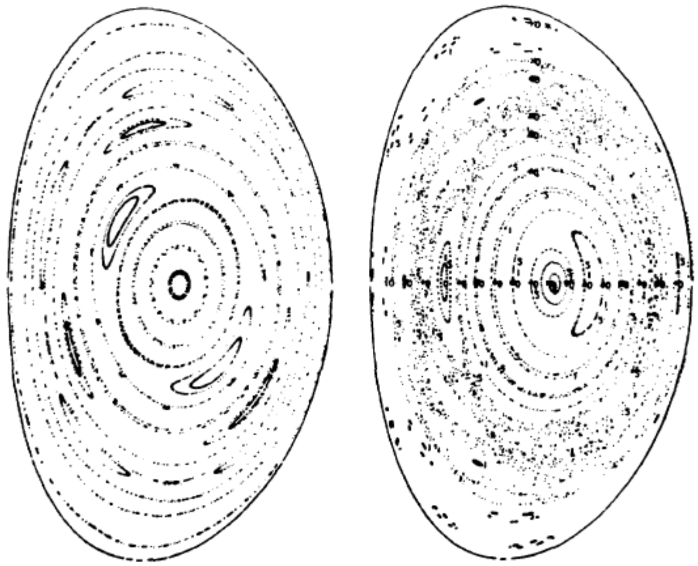

Figure 1.10: Poincaré plot of magnetic field lines in a poloidal cross-section. The left-hand figure shows how islands appear following to a perturbation, while the right-hand figure shows that islands grow and overlap as the perturbation amplitude increases.

Chapter 2

Magnetic measurements

2.1 Hall effect sensors

Consider a thin plate of conductive material, such as copper, that is carrying a current, for example supplied by a voltage generator: if the probes of a voltmeter are connected to the sides of this plates, as shown in 2.1, the measured voltage is zero. Otherwise, if a magnetic field is applied to the plate so that it is at right angles to the current flow, a small voltage appears across the plate. This is due to the concentration of electrons on a side of the plate and holes in the other one since the field lines deviate the charge path due to the Lorentz force [11].

The Hall effect transducer, typically realized with semiconductor materials, such as gallium-arsenide or germanium, rather than conducting materials due to higher carrier concentration, exploit the homonymous effect in order to provide a voltage signal in presence of an incident magnetic field for diagnostics.

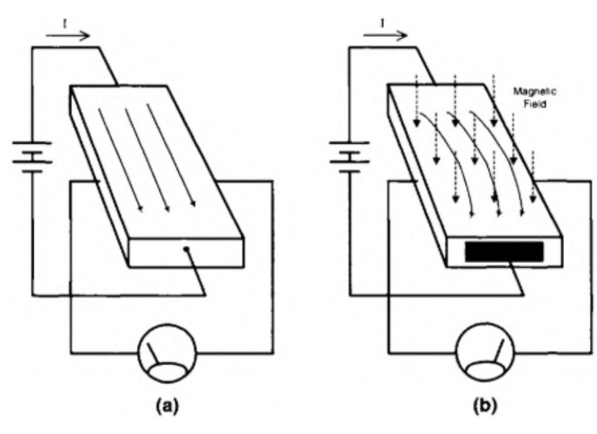

Figure 2.1: The Hall effect in a conductive sheet.

Initially proposed in RFX, they were rapidly discarded, since they are particularly sensitive to temperature variations and thus impossible to install them inside the vacuum chamber. In addition, the fact that they are active devices means that they need a dedicated supply, dramatically increasing the complexity of the system.

2.2 Inductive sensors

Widely spread in fusion plasma diagnostics, inductive sensors [12] are used to measure the magnetic fields inside and outside the vacuum chamber. Since they need to be placed very close to the plasma source, often inside the chamber, they must be designed to work at high temperatures and low pressures, within a range of few hundreds of kHz without introducing intense disturbances or noise in the obtained signal. They consist in different forms of conductive loops, making the design simple and inexpensive.

The voltage across the loop, induced by a changing magnetic field is measured. According to the Faraday's law

$$V = -n\frac{d\Phi}{dt} \tag{2.1}$$

so, by knowing the initial condition for Φ_0, a direct measurement of the magnetic flux is obtained by integrating the voltage difference V:

$$\Phi = \Phi_0 - \int V dt \tag{2.2}$$

Size and shape affect the frequency response of the probe. The self-inductance of a coil increases quadratically with the number of turns N. Consider an air core coil, the general expression is

$$L = \frac{\mu_0 N^2 A_c}{l} K \tag{2.3}$$

where A_c is the cross-section of the coil, l is the axial length and K is a constant factor which depends on the shape of the coil.

Empirical formulae are used for different shapes, but it is worth to report the rectangular coil formula since it is the most common shape in pick-up coils:

$$L_{rect} = \frac{\mu_0}{\pi}\left[-2(a+b) + 2\sqrt{a^2+b^2} - a\ln\frac{a+\sqrt{a^2+b^2}}{b} - b\ln\frac{b+\sqrt{a^2+b^2}}{a} + a\ln\frac{2a}{\frac{d}{2}} + b\ln\frac{2b}{\frac{d}{2}}\right] \tag{2.4}$$

where a and b are cross dimensions and d is the wire diameter.

It is obvious that the inductance value strongly depends on the dimensions of the coil, but, even if it is well known that larger the equivalent area the higher the coil sensitivity (means that frequency magnetic fields in the order of mHz can be detected), it is necessary to do a compromise between this parameter and the available space: as already said, these coils are often installed inside the vacuum chamber, so their geometry must interfere as less as possible with the with other components of the system.

An important negative aspect to consider is the thermal dependence of the probe electrical parameters. Coil inductance and cable resistance tend to increase with the temperature. Moreover, the thermal expansion of the support (made of Torlon, a thermoplastic polymer with excellent thermal and mechanical properties) may further change these electrical characteristics with the consequent loss of calibration.

2.2.1 Rogowski coil

The Rogowski coil is an air-core coil, which measures both alternating and high speed impulse currents. It consists of a toroidal form windings, encircling the current path. In order to eliminate unwanted magnetic field components parallel to the current direction and obtain a correct measure, the coil must be installed all around the torus, and one of the terminal is winded inside the coil. Although, the Rogowski coil is not equipped in RFX-mod2 due to installation issues.

According to Ampere's law [13], the current flowing through the coil along the axis of the torus is as follows:

$$I(t) = \frac{1}{\mu_0} \oint \overrightarrow{B}(t) \cdot d\overrightarrow{l} \tag{2.5}$$

where l is the distance along the torus. Magnetic field variations induces voltage across the winding, and the relation between the induced voltage and the flowing current is given by the Faraday's lawn, independently from current distribution:

$$u(t) = \frac{d\phi}{dt} = \int \frac{d\overrightarrow{B}(t)}{dt} \cdot d\overrightarrow{A} = \frac{A}{n}\mu_0 \frac{dI(t)}{dt} \tag{2.6}$$

considering a constant cross-section A for windings and constant number of turns per unit length n.

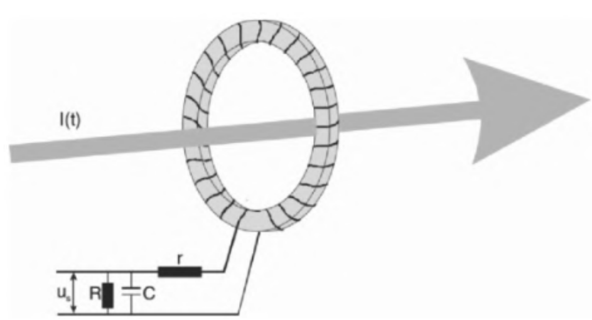

Figure 2.2: A sample Rogowski coil with an RC integrator.

An integrator block is always necessary at the coil output terminal in order to derive the current from the induced voltage. A simple RC circuit, as shown in 2.2, can acts as integrator block, then:

$$u(t) = \frac{d\phi}{dt} = Ri + L\frac{di}{dt} + \frac{1}{C}\int_0^t idt' \tag{2.7}$$

where R and C are respectively the resistance and the capacitance of the integrator circuit, while L is the self-inductance of each winding.

2.2.2 Flux gates

An applied field H to the core induces a magnetic flux $B = \mu H$. For high B the material saturates and μ is very small. There is hysteresis, and the path is different for increasing and decreasing H: when the core is not saturated the core acts as a low impedance path to lines of magnetic flux in the surrounding space. Otherwise, when the core is saturated the magnetic field lines are no more affected by the core. Each time the core passes from saturated to unsaturated and backwards, there is a change to the magnetic field lines. A pick-up coil around the core will generate a spike. Flux lines drawn out of core implies positive spike, lines drawn into core, a negative spike. The amplitude of the spike is proportional to the intensity of the flux vector parallel to the sensing coil. The pulse polarity gives the field direction [14].
This is typically intended for weak fields applications. Toroidal core flux gates with a drive winding inside a cylindrical sensor coil are used.

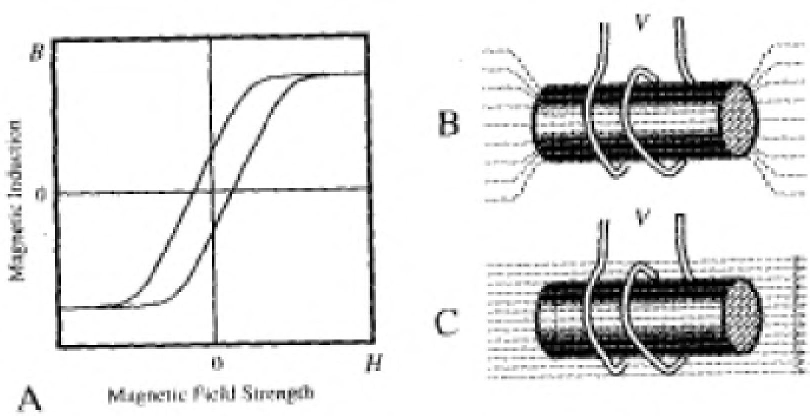

Figure 2.3: Driven flux gate with the relative hysteresis curve: a non-saturated core is shown in the figure B, while a saturated core is shown in the figure C.

2.2.3 Pick-up coils

Already present in RXF for poloidal and toroidal field measures, the new magnetic probes for RFX-mod2 were designed to measure also the radial component, making the installation of the Rogowski coil superfluous.

They consist in three enamelled copper coils winded around a Torlon support, enclosed in a metallic cover in order to mount them inside (or outside) the vacuum chamber shell. The two coils measuring the field component tangential to the plasma boundary have an effective sensing area of about 250 cm^2, while the radial one has an effective sensing area of 2000 cm^2. There are four different typologies [15]:

- **internal triaxial sensors**, all the three components (radial, poloidal and toroidal) are measured inside the shell;
- **external biaxial sensors**, just the poloidal and toroidal components are measured outside the shell;
- **internal biaxial HF sensors**, for high frequency measure of poloidal and toroidal components;
- **internal uniaxial HF sensors**, only one measure for the toroidal component.

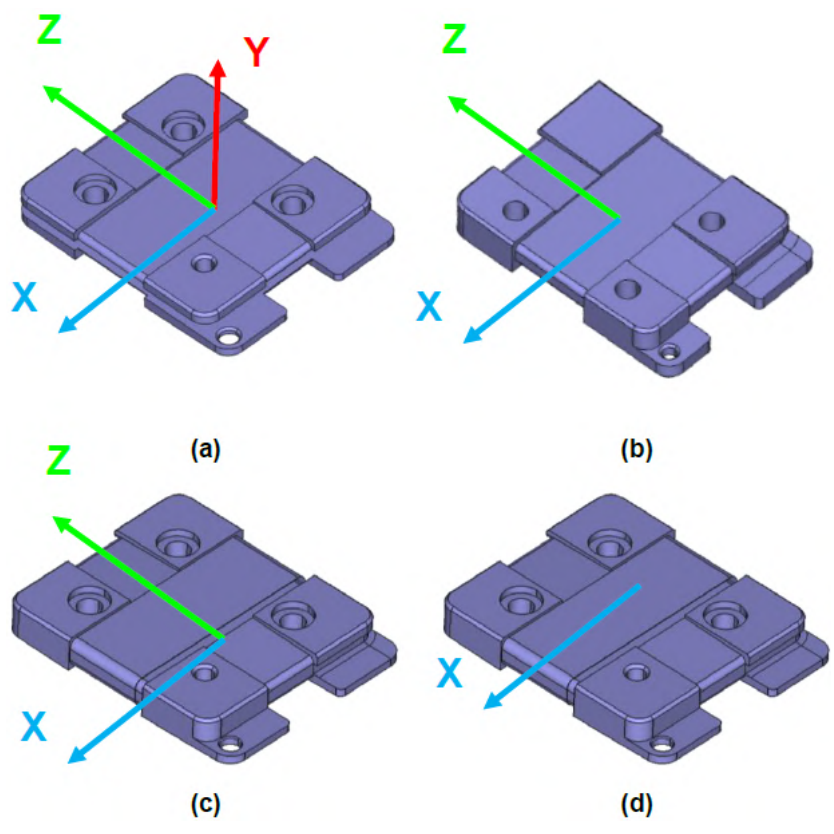

Figure 2.4: Sets of axes for each type of sensor: (a) triaxial pick-up coil reel, (b) biaxial external coil reel, (c) biaxial HF coil reel, (d) uniaxial HF coil reel.

As already reported, the magnetic flux variation induces voltage across the coil which is the derivative of the magnetic field with respect to the time $\frac{dB}{dt}$, then the signal must be integrated in order to obtain a measure of the magnetic field.

2.3 Magnetic diagnostic in RFX-mod2

Magnetic confined fusion machines demand sophisticated real-time feedback control systems to maintain plasma stability and protect machine integrity. These systems must operate with response times on the order of 1 ms, a requirement driven by the need to study fast physics phenomena and mitigate instabilities. RFX has established itself as a foundational test bench in this field, capable of operating in both Reversed Field Pinch (RFP) and Tokamak configurations. Its flexibility allows for the exploration of RFP plasmas with dominant helical shapes (creating a bridge to stellarator geometry) as well as stable, low q Tokamak plasmas. This versatility is made possible by an advanced network of 192 independently driven saddle coils and a comprehensive diagnostic suite that counteracts plasma instability growth.

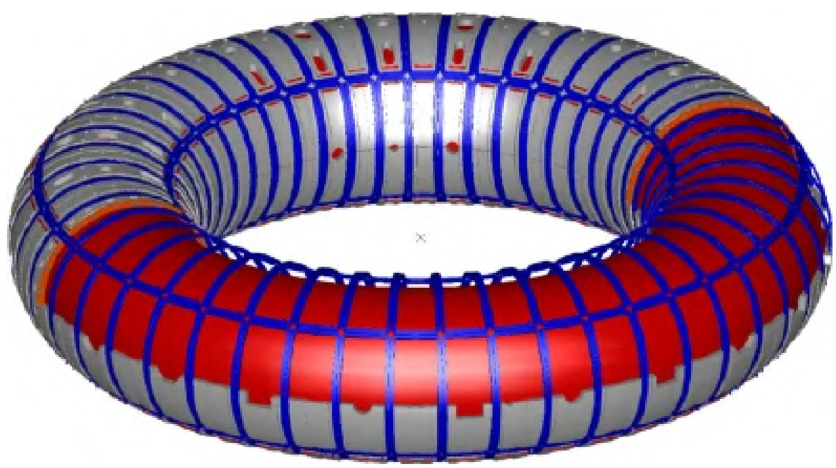

Figure 2.5: The RFX 192 saddle coils in blue, 48 in the toroidal direction, 4 in the poloidal one.

In the original RFX configuration, the magnetic diagnostic system was strategically divided into two distinct sections to overcome the electromagnetic shielding properties of the Inconel (a superalloy with excellent shielding properties composed mainly of nickel, chromium, and iron) vacuum vessel:

- **External sensors**, pick-up coils were housed inside the vacuum vessel alongside electrostatic and calorimetric sensors. This internal placement was essential for measuring turbulence and rapid magnetic field variations that would otherwise be attenuated by the vessel's walls;
- **Internal sensors**, located between the vacuum vessel and the copper stabilizing shell, these probes measured magnetic field variations in the kHz range, which are critical for determining

plasma equilibrium.

The signal processing system relied on analog integration based on operational amplifiers. The architecture was characterized by a clear separation between two subsystems: transient recorder, high sampling resolution requires longer processing times, and real-time control, lower resolution but optimized for high-speed processing to meet feedback requirements. The hardware consisted of 400 conditioning channels, distributed across 25 circuit boards with 16 channels each. Each channel featured differential amplifiers, low-drift analog integrators, and programmable gain stages. While effective, this setup required significant physical space and manual configuration.
The transition to RFX-mod2 involves a fundamental modification of the machine assembly to improve RFP confinement. This upgrade has provided an opportunity to completely renew the magnetic diagnostic system. A major innovation in RFX-mod2 is the adoption of triaxial pick-up coils. These sensors were selected for their compact dimensions and their ability to compensate for alignment errors. In a significant structural shift, all probes are now moved inside the vacuum vessel, protected behind 2,016 graphite tiles (72×28) that line the machines internal surface.

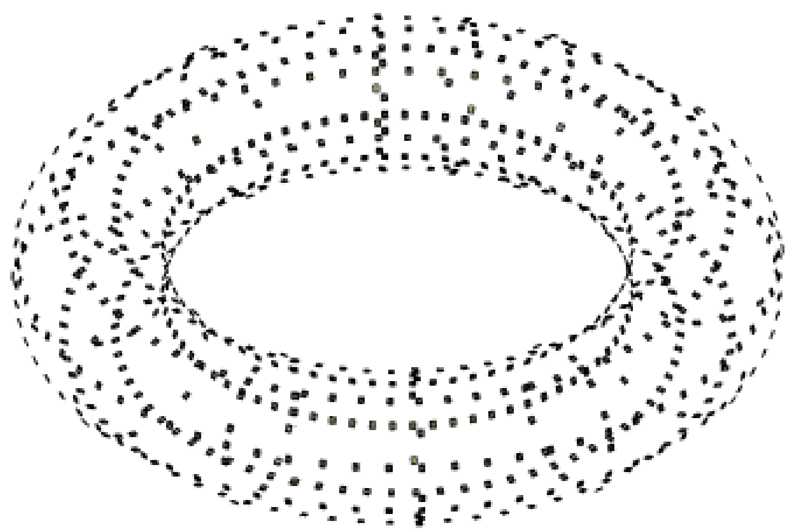

Figure 2.6: Layout of the arrays of pick-up coil sensors (8 toroidal and 13 poloidal).

The number of magnetic sensors is then dramatically increased (724 pick-up probes for 1088 signals), allowing an improved characterization of the spatial harmonic structure of the plasma in both RFP and Tokamak configurations.
The other most significant technical leap in RFX-mod2 was the adoption of purely numerical integration. Unlike the previous analog system, the new architecture utilizes the Xilinx Zynq platform, which integrates an ARM processor with an FPGA on a single chip. The system is now very simple to manage and significantly reduces physical space requirements. It is organized into 12 channels per

6U rack, totaling 144 boards housed within just two cabinets.

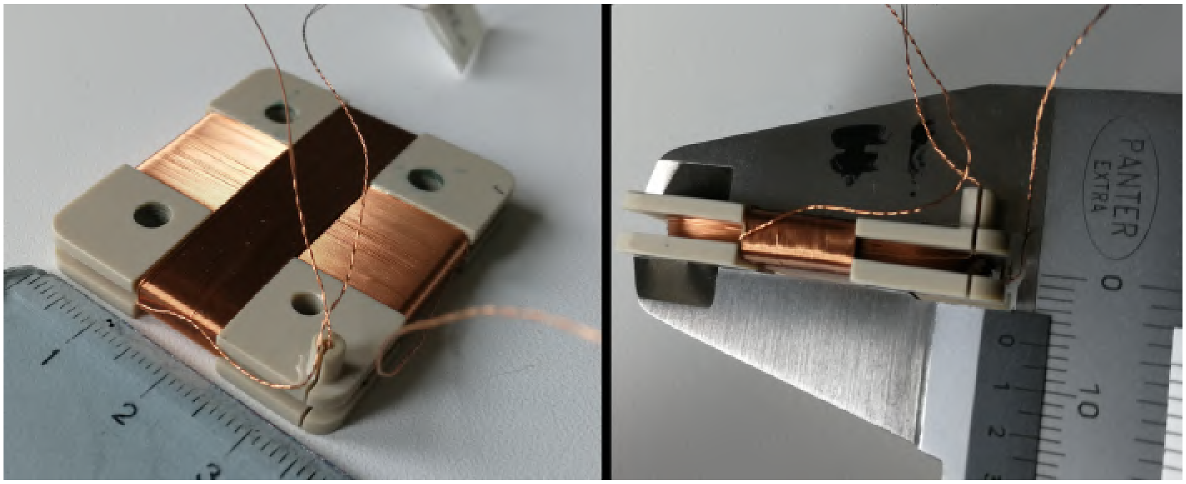

Figure 2.7: Dimensions of a triaxial pick-up sensor used in RFX-mod2.

Chapter 3

Integration methods

3.1 Analog integration

Since the inductive sensors produce a voltage signal proportional to the rate of change of the magnetic flux ($\frac{dB}{dt}$), the signal must be integrated over time in order to reconstruct the actual magnetic field. While conceptually simple, achieving high-precision integration over long timescales presents significant issues, primarily due to electronic drift and noise.

The most simple model is obtained with a passive RC circuit, shown in 3.1, ideal for high frequency signals. The transfer function between output and input signal voltages is given by:

$$V_{out} = \frac{1}{1 + j\omega\tau} V_{in} \approx \frac{1}{\tau} \int V_{in} dt \tag{3.1}$$

where $\tau = RC$ is the characteristic integration time and $\omega\tau \gg 1$. However, increasing the integration time constant to handle longer pulses significantly attenuates the output signal.

To solve this, active integrators (often called Miller Integrators, also shown in 3.1) utilize operational amplifiers. By placing a capacitor in the feedback loop, the integration timescale is effectively multiplied by the amplifiers open-loop gain. Now the transfer function becomes:

$$V_{out} = -\frac{G}{1 + j\omega\tau + Gj\omega\tau} V_{in} \approx -\frac{1}{\tau} \int V_{in} dt \tag{3.2}$$

where $G = 10^5 \div 10^6$ is the amplifiers open-loop gain and $G\omega\tau \gg 1$. This allows the integration of sensor signals in experiments with typical pulse lengths up to 10 seconds.

As already said, the primary issue of active integrator is the drift introduced by any small differential DC offset on the integrator input that are integrated along with it, becoming particularly significant when the measurement requires long lasting pulses: the longer is the pulse, the greater is the rate of drift divergence, becoming greater than linear. Voltage offset are mainly caused by intrinsic imperfections of electronics (present in every real components), electromagnetic interferences and thermoelectric voltages (due to the Seebeck effect).

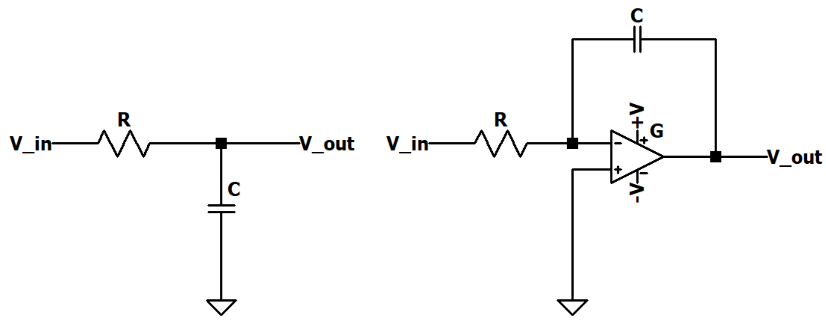

Figure 3.1: The left-hand figure shows a simple passive RC circuit, while an active Miller integrator is shown on the right-hand figure.

3.2 Digital integration

To overcome the inherent limitations of analog integrators, specifically capacitor leakage and signal drift, modern systems leverage hybrid and full-digital integration architectures. Hybrid schemes utilize dual analog integrators: one processing the sensor input and another connected to a dummy load to measure drift. By digitally combining these signals and periodically reversing the integrators' roles, the system eliminates drift errors regardless of pulse length. Full-digital integration technique completely eliminate the "*droop*" error during constant magnetic field interval, but new significant errors are introduced.

Voltage saturation of the ADC tends to produce large derivative of the magnetic field ($\frac{dB}{dt}$), for this reason two or more parallel input channels with different gains are used: high-gain channel is normally selected and it is changed when saturated. Low-pass RC filters are also used in order to limit the peak voltage and smooth fast transients.

Also low bit resolution introduces a significant error which increases in time when the signal is constant and sampling rates must be chosen fast enough with respect to the phenomena to be observed in order to limit the error introduced by finite time resolution.

3.3 Noise in acquisition chain

Noise is an unwanted signal disturbance that can cause important variations in the acquired data, a critical parameter in the integration process since its effects add up and make an important distortion of the resulting signal, especially if the acquisition lasts for several seconds. Several sources of noise, such as imperfections of the components and shielding or interference of various nature, generally add up background white noise with a constant power spectral density across the frequency spectrum and so easy to filter.

Although, flicker ($1/f$) noise is way more insidious, its power spectral density is inversely proportional to frequency ($S(f) \propto \frac{1}{f}$, as the name implies) and affects almost all the electronic components. This type of noise is particularly harmful and difficult to eliminate even with post acquisition processing because there is no simple relationship between the noise level and the standard deviation of the integrated signal. $1/f$ disturbances manifest final drift errors that grow at least linearly over time. Therefore, the design of a data acquisition (DAQ) system must prioritize high-performance electronic components with ultra-low noise floors.

The relative amount of signal and noise present in a waveform is usually quantified by the signal-to-noise ratio (SNR), which specifies the relative magnitudes of the signal power to the existing noise power, both measured in root mean squared amplitudes. The SNR is often expressed in decibel:

$$SNR_{dB} = 20 \log \left(\frac{P_{signal}}{P_{noise}} \right) \quad [dB] \tag{3.3}$$

When expressed in dB, a positive number means the signal is greater than the noise and a negative number means the noise is greater than the signal.

Ensuring the highest signal to-noise ratio of the acquired signal is essential in order to perform correct integration.

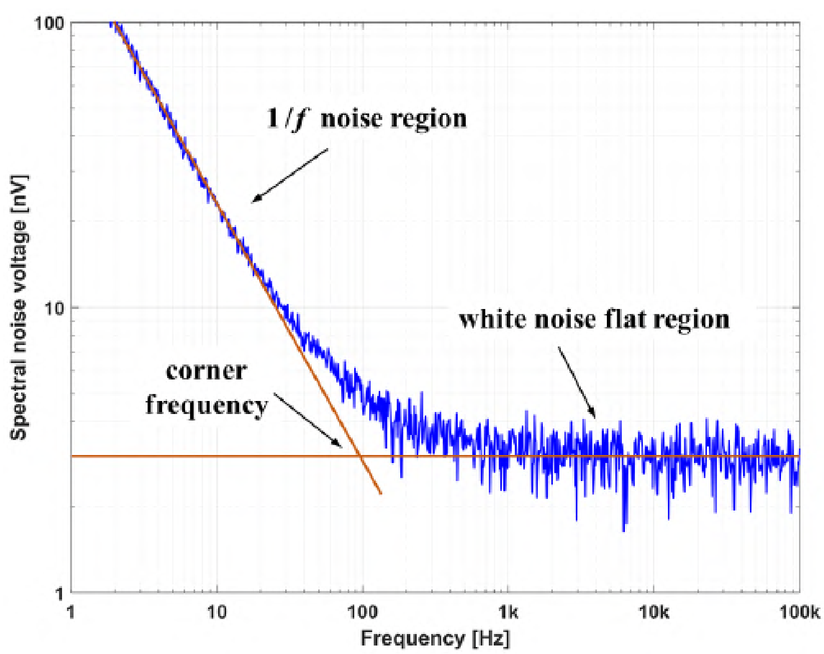

Figure 3.2: Flicker noise in a differential amplifier.

3.3.1 Zero-drift amplifiers

Zero-drift amplifiers [16] provide ultra-low input offset voltage, near-zero input offset voltage drift over temperature and time, and, most importantly, no $1/f$ flicker noise, low broadband noise and low distortion. They are suitable for a wide variety of precision applications that benefit from stability in the signal path. System performance can be optimized by using standard continuous-time amplifiers plus an auto-calibration mechanism. The offset of the amplifier is corrected through internal periodic calibration, so the magnitude of the offset transition and the crossover distortion is greatly diminished. However, this additional auto-calibration requires complicated hardware and software.
It is preferred to use the chopping zero-drift amplifier structure: the input and output of the first stage has a set of switches that inverts the input signal every calibration cycle. In the first half-cycle, both sets of switches are configured to flip the input signal twice, but the offset flips once. This keeps the input signal in phase but the offset error polarity is reversed. In the second half-cycle, both sets of switches are configured to pass the signal and offset error through unaltered. The input signal is never out of phase, remaining unchanged, while the offset error, which is opposite in polarity in the second half-cycle, it is averaged to zero. A synchronous notch filter is used at the same frequency of switching to attenuate any residual error.

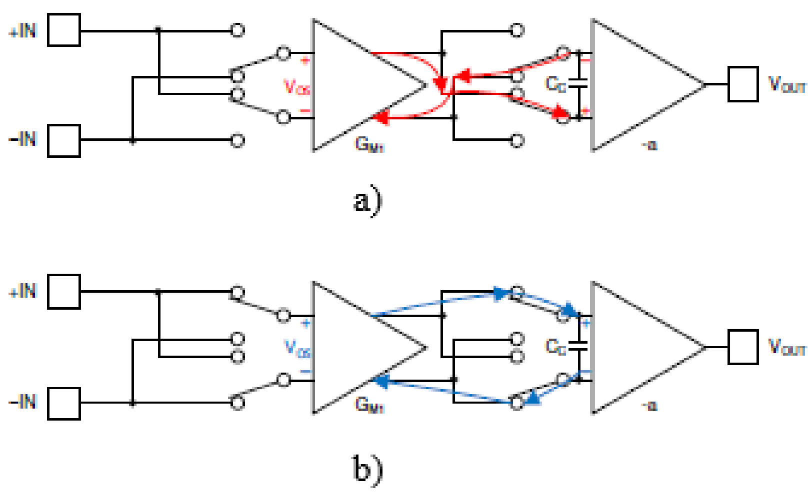

Figure 3.3: The first half-cycle is represented in the upper schematic, while the second one is reported in the bottom figure. It is clear that the input signal is never out of phase, while the offset error polarity is reversed during the second half-cycle.

Auto-zeroing is a similar technique, but requires different topology: it has less distortion at the output, while chopping results in lower broadband noise. In general, zero-drift amplifiers offer the lowest 1/f noise.

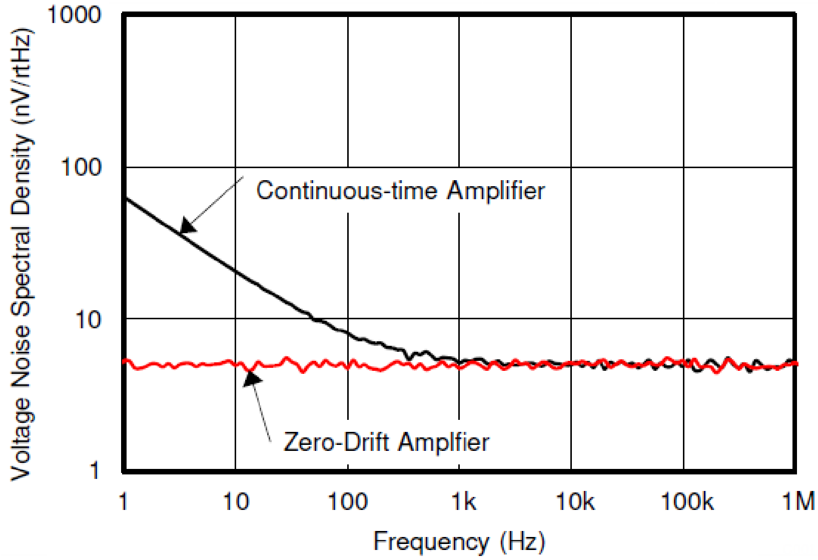

Figure 3.4: Noise comparison between continuous-time and zero-drift amplifiers.

3.4 Data acquisition system in RFX-mod2

In the original RFX machine, data acquisition was performed by analog components and the acquisition systems were doubled after the integration block, in order to make available both the integrated and derived signals.

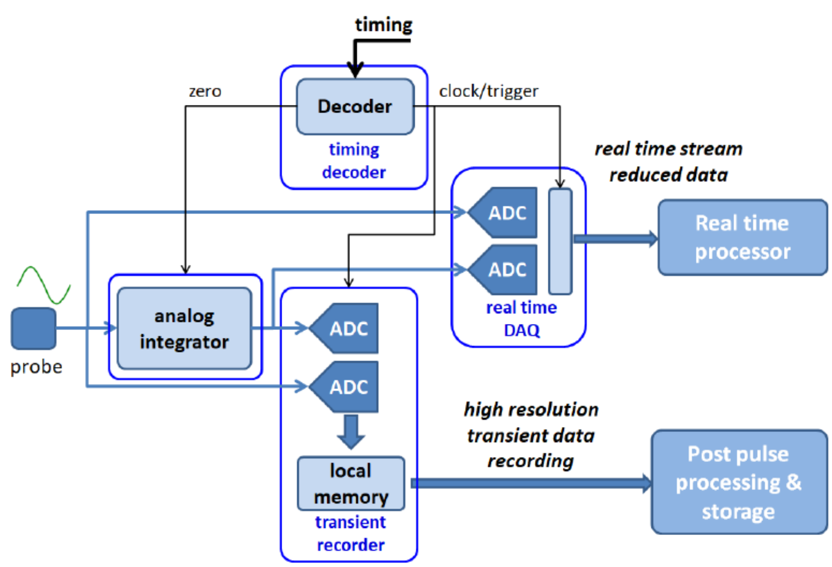

Figure 3.5: Traditional block diagram for magnetic measurements acquisition in RFX.

However, this system was particularly complex from the point of view of wiring and maintenance, and, consequently, very bulky and delicate. For these reasons, also the data acquisition systems were substantially upgraded in RFX-mod2, opting for System-on-Chip (SoC) components, which integrate an FPGA and a microprocessor system onto the same chip, drastically reducing the hardware dimensions. This enables the streamlined management and integration of typical FPGA tasks (hardware interfacing with ADCs, filtering, compensation, and numerical integration) on one hand, and standard CPU tasks (data storage, network transmission, and system monitoring) on the other [17]. The ADC-FPGA interface also allows for the implementation of galvanic isolation on the inputs. This offers intrinsic noise immunity, fundamentally eliminating problems caused by ground loops. Of course, all the magnetic signals are available in both integrated and derivative forms, like in the previous system.

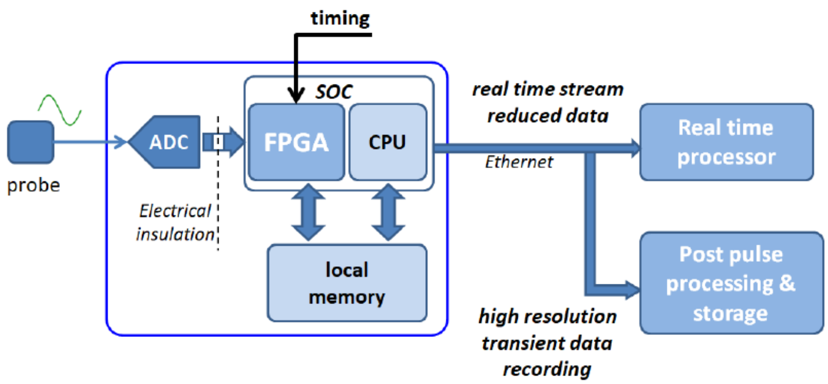

Figure 3.6: New block diagram for magnetic measurements acquisition in RFX-mod2.

The proposed "*rack*" structure is composed by 12 boards with 12 ADC modules each (so 144 channels in total per rack, as shown in 3.8). For each board is present a system-on-module (SoM) Xilinx Zynq, which operates the ADC module and manages external communications, timing, memory and interface. Each acquisition channel is managed on an independent module, featuring a 20-bit ADC with a sampling rate of 1 $\frac{MS}{s}$, and it is galvanically insulated from the local ground (insulation must withstand 1 kV_{rms} in AC and 2.5 kV impulses).

The network and USB connections are organized on the front side of the rack, while the rear side presents all the input interfaces.

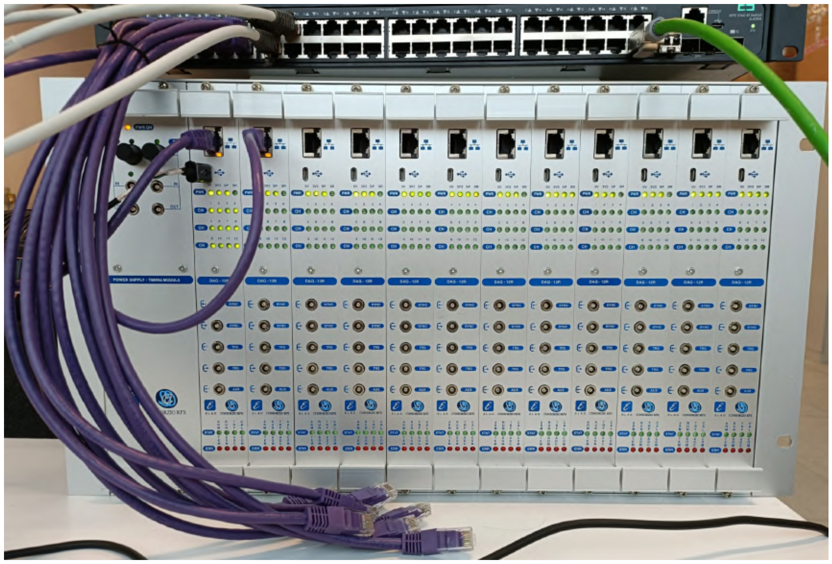

Figure 3.7: Front side of the rack.

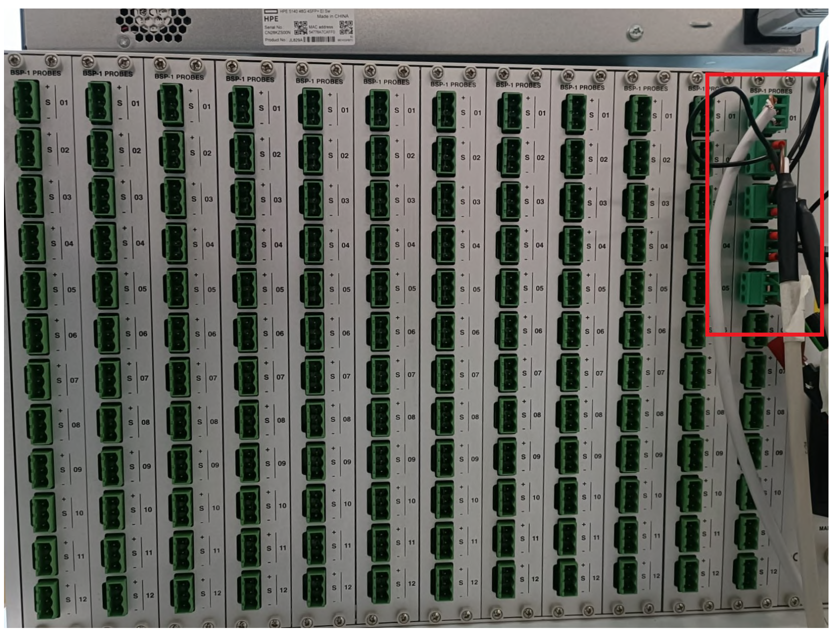

Figure 3.8: Rear side of the rack. The highlighted input channels were used in this thesis work.

Chapter 4

Acquisition chain characterization

4.1 Transmission line with uniformly distributed parameters

Consider a transmission line in sinusoidal regime with uniformly distributed parameters [18], as shown in 4.1, each infinitesimal element dx can be qualified by four kilometric or "*per unit length*" parameters:

- r is the longitudinal kilometric resistance in $\left[\frac{\Omega}{km}\right]$;
- l is the longitudinal kilometric inductance in $\left[\frac{H}{km}\right]$;
- c is the transversal kilometric capacitance in $\left[\frac{F}{km}\right]$;
- g is the transversal kilometric conductance in $\left[\frac{S}{km}\right]$.

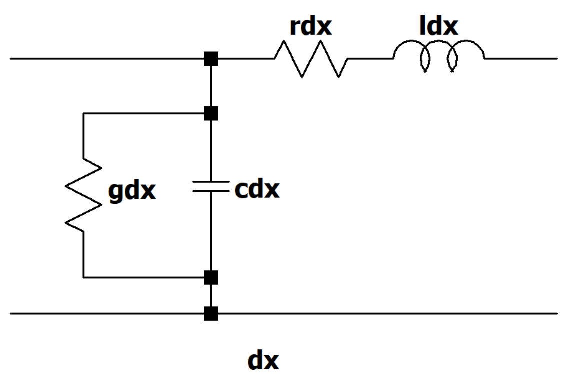

Figure 4.1: Infinitesimal element of a transmission line with kilometric parameters.

In steady-state regime, at a given ω angular frequency, each infinitesimal length dx of the line is characterized by:

$$\begin{cases} \underline{z}dx = (r + j\omega l)dx \\ \underline{y}dx = (g + j\omega c)dx \end{cases} \tag{4.1}$$

where $\underline{z}$ is the kilometric series impedance in $\left[\frac{\Omega}{km}\right]$ and $\underline{y}$ is the kilometric shunt admittance in $\left[\frac{S}{km}\right]$.
The voltage drop across the kilometric series impedance $\underline{z}$ is given by the voltage increase $d\underline{E}_x$ on the infinitesimal element dx:

$$d\underline{E}_x = \underline{I}_x \underline{z} dx \tag{4.2}$$

while the current derived by the kilometric shunt admittance $\underline{y}$ is given by the current variation $d\underline{I}_x$ between the two ports of the element:

$$d\underline{I}_x = (\underline{E}_x + d\underline{E}_x)\underline{y} dx \tag{4.3}$$

The term $d\underline{E}_x \underline{y} dx$ can be neglected, so 4.2 and 4.3 can be rewritten as it follows:

$$\begin{cases} \frac{d\underline{E}_x}{dx} = \underline{I}_x \underline{z} \\ \frac{d\underline{I}_x}{dx} = \underline{E}_x \underline{y} \end{cases} \tag{4.4}$$

This is a set of two coupled, linear partial differential equations that model voltage and current along a linear electrical transmission line and they are named "*telegrapher's equations*".
The Laplace transform of a function's derivative is well-known,

$$\mathcal{L}\left\{\frac{df(x)}{dx}\right\} = s\mathcal{L}\{f(x)\} - f(0) \tag{4.5}$$

and so, the following system arises from 4.4:

$$\begin{cases} s\mathcal{L}\{\underline{E}_x\} - \underline{E}_a = \underline{z}\mathcal{L}\{\underline{I}_x\} \\ s\mathcal{L}\{\underline{I}_x\} - \underline{I}_a = \underline{y}\mathcal{L}\{\underline{E}_x\} \end{cases} \tag{4.6}$$

where $\underline{E}_a$ and $\underline{I}_a$ are the receiving-end voltage and current phasors, *i.e.*, at $x = d$, where d is the transmission line length.
Then, using the Cramer's rule and defining the two new quantities $\underline{k}$ and $\underline{Z}_c$, the following system is obtained:

$$\begin{cases} \mathcal{L}\{\underline{E}_x\} = \frac{s\underline{E}_a + \underline{k}\underline{Z}_c\underline{I}_a}{s^2 - \underline{k}^2} \\ \mathcal{L}\{\underline{I}_x\} = \frac{s\underline{I}_a + \frac{\underline{k}}{\underline{Z}_c}\underline{E}_a}{s^2 - \underline{k}^2} \end{cases} \tag{4.7}$$

where $\underline{Z}_c = \sqrt{\frac{\underline{z}}{\underline{y}}}$ is the characteristic impedance in $[\Omega]$, while $\underline{k} = \sqrt{\underline{z}\underline{y}} = k' + jk''$ is the propagation constant in $\left[\frac{rad}{km}\right]$ (the real part k' is called "*attenuation constant*", while the imaginary part k'' is the "*phase constant*").

Applying the inverse Laplace transform on 4.7 and consider $\underline{E}_p$, $\underline{I}_p$ to be the sending-end voltage and current phasors, *i.e.*, at $x = 0$, the relation between the sending-end and receiving-end phasors respectively is finally obtained:

$$\begin{cases} \underline{E}_p = \underline{A}\underline{E}_a + \underline{B}\underline{I}_a \\ \underline{I}_p = \underline{C}\underline{E}_a + \underline{D}\underline{I}_a \end{cases} \tag{4.8}$$

or, in matrix form,

$$\underbrace{\begin{bmatrix} \underline{E}_p \\ \underline{I}_p \end{bmatrix}}_{\underline{W}_p} = \underbrace{\begin{bmatrix} \underline{A} & \underline{B} \\ \underline{C} & \underline{D} \end{bmatrix}}_{\underline{M}} \cdot \underbrace{\begin{bmatrix} \underline{E}_a \\ \underline{I}_a \end{bmatrix}}_{\underline{W}_a} \tag{4.9}$$

where $\underline{A} = \cosh(\underline{k}d)$, $\underline{B} = \underline{Z}_c \sinh(\underline{k}d)$, $\underline{C} = \frac{\sinh(\underline{k}d)}{\underline{Z}_c}$, $\underline{D} = \cosh(\underline{k}d)$ are the transmission hybrid parameters.

$\underline{W}_p$ and $\underline{W}_a$ are called hybrid vectors, while $\underline{M}$ is the transmission matrix.

$\underline{M}$ is symmetrical since the line has uniformly distributed parameters, and so $\underline{A} \equiv \underline{D}$. In fact:

$$\det(\underline{M}) = \underline{A}\underline{D} - \underline{B}\underline{C} = [\cosh(\underline{k}d)]^2 - [\sinh(\underline{k}d)]^2 = 1 \tag{4.10}$$

i.e., the matrix is reciprocal since it is symmetrical.

4.1.1 Propagation phenomenon

Starting from the sending-end voltage phasor:

$$\underline{E}_p = \underline{A}\underline{E}_a + \underline{B}\underline{I}_a = \cosh(\underline{k}d)\underline{E}_a + \underline{Z}_c \sinh(\underline{k}d)\underline{I}_a \tag{4.11}$$

the hyperbolic functions can be expressed also with exponential definitions,

$$\begin{aligned} \underline{E}_p &= \left(\frac{e^{\underline{k}d} + e^{-\underline{k}d}}{2}\right)\underline{E}_a + \underline{Z}_c\left(\frac{e^{\underline{k}d} - e^{-\underline{k}d}}{2}\right)\underline{I}_a = \\ &= \left(\frac{\underline{E}_a + \underline{Z}_c\underline{I}_a}{2}\right)e^{\underline{k}d} + \left(\frac{\underline{E}_a - \underline{Z}_c\underline{I}_a}{2}\right)e^{-\underline{k}d} = \\ &= \underline{U}_1 e^{\underline{k}d} + \underline{U}_2 e^{-\underline{k}d} \end{aligned} \tag{4.12}$$

The first term represents a sinusoidal wave that travels in the time domain from left to right and it is called "*incident wave*", while the second term, on the contrary, represents a sinusoidal wave that travels from right to left in the time domain and it is called "*reflected wave*", all at the same angular frequency ω.

Now consider, in the case of an ideal line (lossless means that $k' = 0$), the wavelength between two successive maxima with the rotation of the voltage phasor equal to 2π:

$$\lambda = \frac{2\pi}{k''} = \frac{2\pi}{\omega\sqrt{lc}} \tag{4.13}$$

From this, the propagation velocity of the wave is given:

$$v = \frac{\lambda}{T} = \lambda f = \frac{2\pi f}{k''} = \frac{2\pi f}{\omega\sqrt{lc}} = \frac{1}{\sqrt{lc}} \tag{4.14}$$

4.2 Impedance matching

Impedance matching is crucial in data transmission because it ensures maximum power transfer from a signal source to its load while preventing signal degradation. When high-frequency data travels down a transmission line, any mismatch between the source, line, and termination impedances causes a portion of the electrical wave to reflect backward toward the sender. These signal reflections interfere with incoming data, creating standing waves and signal distortion that can corrupt transmitted signals. Consider to have a transition point M where there is an abrupt change of circuit constants, for example two different surge impedances Z_1 and Z_2 in the case of a transmission line: an incident step wave v_i is impinging on the point M, giving rise to a reflected wave v_r, which travels on Z_1 to the left, and a transmitted wave v_t, which travels on Z_2 to the right, like in 4.2.

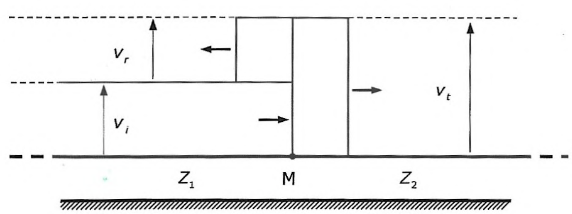

Figure 4.2: Incident, reflected and transmitted step waves at the transition point M.

At the boundary, voltage and current must be continuous:

$$\begin{cases} v_i + v_r = v_t \\ i_i + i_r = i_t = \frac{v_i}{Z_1} - \frac{v_r}{Z_1} = \frac{v_t}{Z_2} \end{cases} \tag{4.15}$$

in fact, current must be equal before and after the point M in absence of any shunt element. By combining the voltage and current conditions and solve for v_t:

$$v_t = \frac{2Z_2}{Z_1 + Z_2} v_i = \tau v_i \tag{4.16}$$

where the "*transmission coefficient*" τ is defined.

Furthermore, solving for v_r:

$$v_r = \frac{Z_2 - Z_1}{Z_1 + Z_2} v_i = \rho v_i \tag{4.17}$$

where the "*reflection coefficient*" ρ is defined.

These two coefficients are related by the following fundamental expression:

$$1 + \rho = \tau \tag{4.18}$$

The system is effectively matched whenever the condition $Z_2 = Z_1$ is satisfied, therefore $\rho = 0$ and $\tau = 1$. In fact, in a matched system, there is no reflected current since there is no reflected voltage and so the transmitted current is equal to the incident one.

4.2.1 Maximum power transfer

The maximum active power transfer [19] theorem (or impedance matching theorem) states that an affine symbolic voltage generator, with source voltage $\overline{E}$ and internal impedance $\dot{Z}_i$, delivers the maximum active power when connected to a passive two-port network with an equivalent impedance $\dot{Z}_u$ equal to the complex conjugate of $\dot{Z}_i$:

$$\dot{Z}_u = \dot{Z}_i^* \implies P_{max} = \frac{E^2}{4\mathfrak{Re}\{\dot{Z}_i\}} \tag{4.19}$$

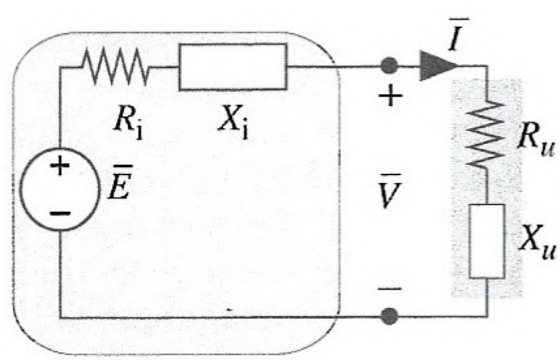

Figure 4.3: Simple circuit where output and input impedances are represented.

In fact, starting from the circuit in 4.3, the current flowing through the two impedances is:

$$\overline{I} = \frac{\overline{E}}{\dot{Z}_i + \dot{Z}_u} = \frac{\overline{E}}{(R_i + R_u) + j(X_i + X_u)} \tag{4.20}$$

The active power leaving the affine generator and entering $\dot{Z}_u$:

$$P = \mathfrak{Re}\{\dot{Z}_u\}I^2 = \frac{R_u E^2}{(R_i + R_u)^2 + (X_i + X_u)^2} \tag{4.21}$$

The maximum value for $P = P(R_u, X_u)$ is then obtained with the following condition:

$$(X_i + X_u)^2 = 0 \implies X_i = -X_u \tag{4.22}$$

therefore when the magnitudes of the internal impedance of the active network and the load impedance are equal $R_i = R_u$.

When attempting to maximize active power across a load whose impedance does not satisfy the previous condition, a transformer with a transformation ratio n can be placed between the active network and the load. In this case:

$$\dot{Z}_{eq} = n^2 \dot{Z}_u \tag{4.23}$$

where a suitable choice for the transformation ratio is $n = \sqrt{\frac{R_i}{R_u}}$.

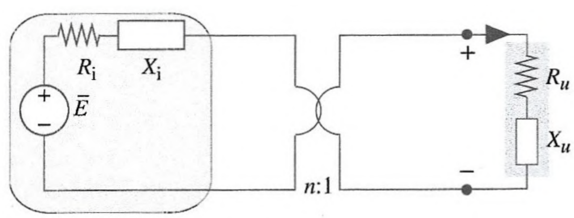

Figure 4.4: Ideal transformer between input and output impedances.

An efficiency η, which is the ratio of the power dissipated by the load resistance R_u to the total power dissipated by the circuit, can be defined:

$$\eta = \frac{I^2 R_u}{I^2(R_i + R_u)} = \frac{1}{1 + \frac{R_i}{R_u}} \tag{4.24}$$

4.2.2 Acquisition chain model

The components of the acquisition chain are shown in 4.6.

The magnetic sensor model is attached at the sending-end of the transmission line and it is schematized as a variable voltage source, a series impedance Z_s which represents the strong inductive behavior of the probe and a parallel impedance Z_p in order to take in account any capacitive effect between the turns of the coil or on the shield.

The transmission line is realized by a twisted pair of shielded cables in order to minimize the cables

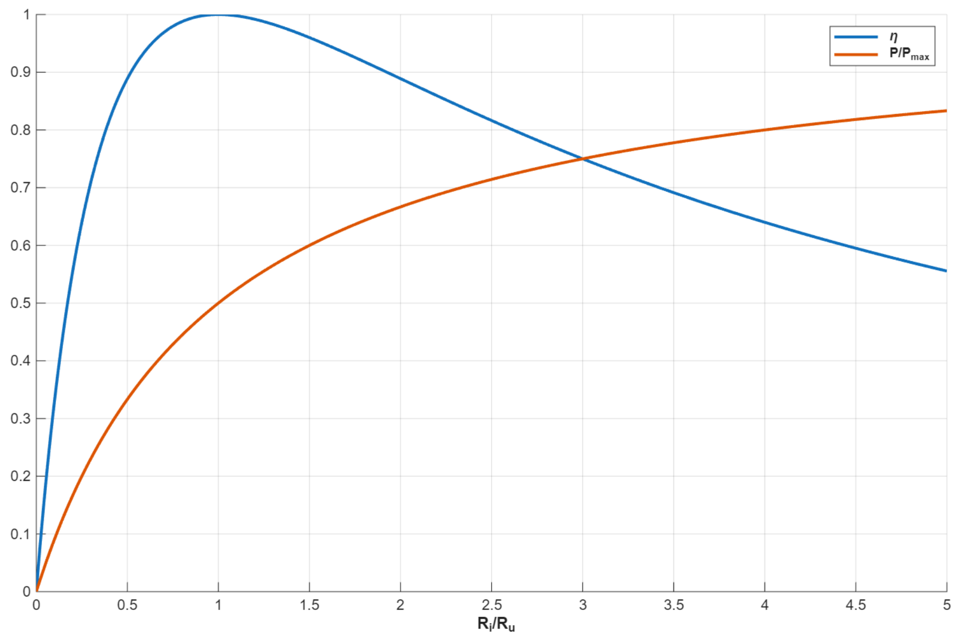

Figure 4.5: Efficiency and power dissipated by load. Note that the power curve reaches its maximum at $R_i = R_u$.

contribution to the total magnetic flux intercepted by the circuit. In the scheme it is simply represented by the impedance Z_L, but it is important to take it in account since it can introduce reflection phenomena.

The entire chain is then attached to the electronic part, made up of amplifier and integrator, but it must be loaded at the receiving-end of the transmission line by an adapter Z_X, which normally is smaller than the electronics input impedance Z_D.

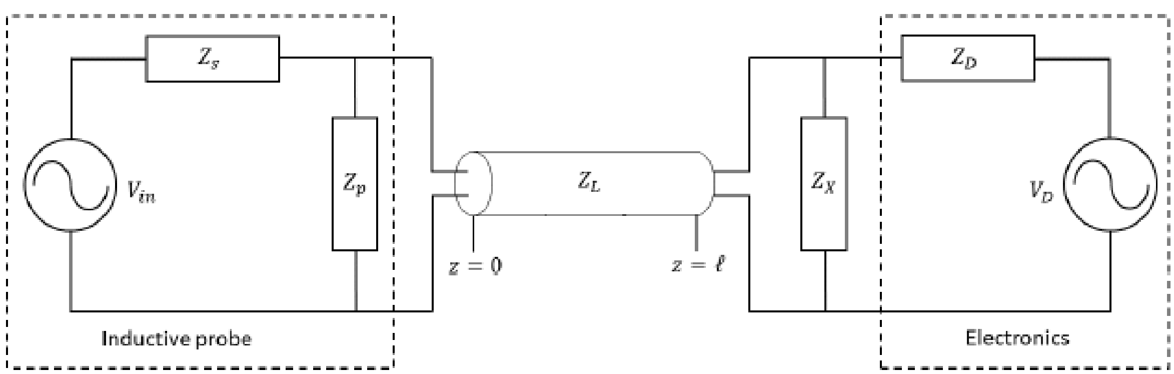

Figure 4.6: Model of the entire acquisition chain.

4.3 Inductive sensor equivalent model

All the models and simulations in this dissertation were realized using LTspice, an high-reliability simulation software that allows users to design analog circuit schematics using an immense number of existing device models. The simulations were performed under AC analysis mode, which performs a small-signal analysis of the circuit by linearizing it around its operating point.

The ideal model in 4.7 consists basically in a sinusoidal current generator and a transformer: the primary winding represents the magnetic field source (the plasma current), while the secondary one represents the probe of course. In LTspice, the transformation ratio is given by the square of the inductance ratio. The coupling between the primary and secondary coils is defined by the coefficient K_1. However, in LTspice, this coefficient is limited to be less than one: for this reason a current of 10 A and an inductance of 0.1 H were used instead.

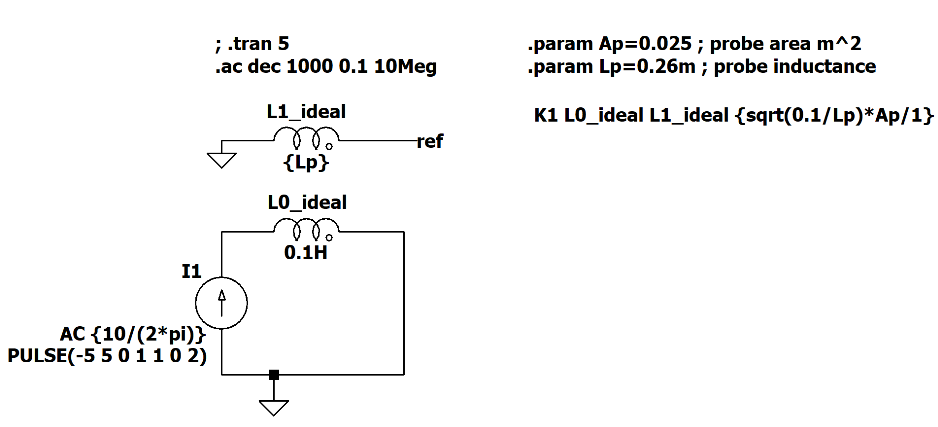

Figure 4.7: Ideal model of the probe.

In the real model, the parasitic components of the probe are taken into account. Those are due to the resistivity of the copper wire and the stray capacitive effect between each turn. The introduction of these parasitic components gives rise to resonance effect at a specific frequency value, calculated as it follows:

$$f_c = \frac{1}{2\pi\sqrt{L_1 C_1}} \tag{4.25}$$

The real model is shown in 4.8.

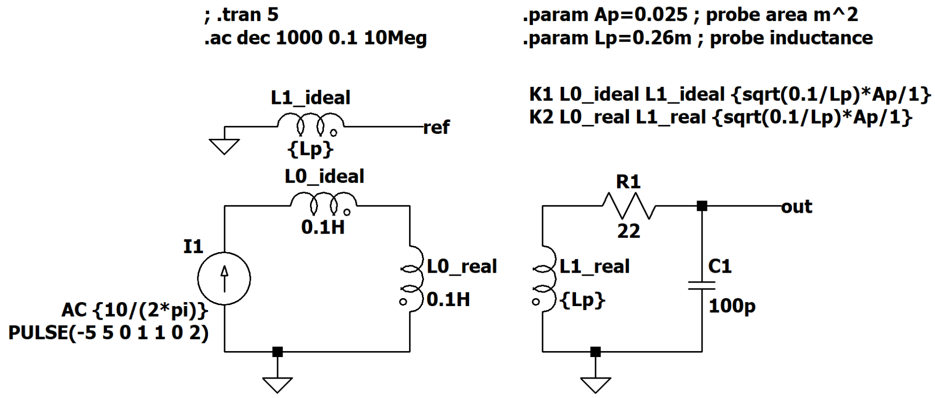

Figure 4.8: Real model of the probe.

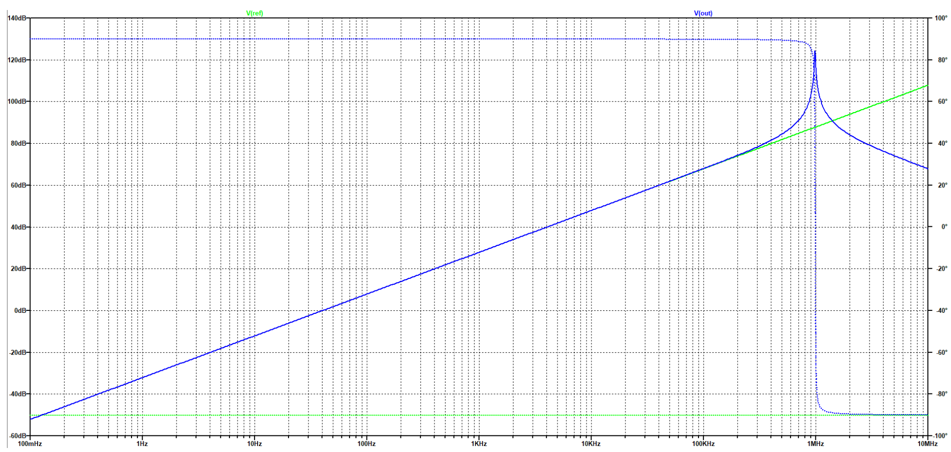

Figure 4.9: Magnitude and phase of the induced voltage on the probe obtained from the simulation in the frequency domain of the ideal model (in green) and the real model (in blue). Note that the resonance peak appears at $\sim 1\ MHz$.

In addition, an impedance measurement was performed for each coil of the sensor by using the impedance analyzer HP4194A shown in 4.10. This instrument is used to plot the magnitude and phase of a load performing a sweep over a large range of frequencies (from 100 Hz to 40 MHz).

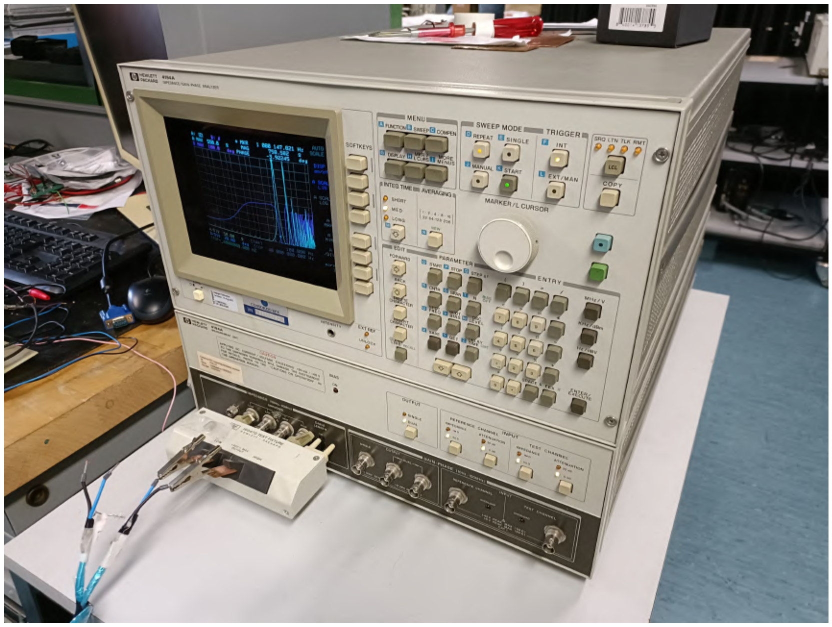

Figure 4.10: Impedance analyzer HP4194A. Note the four-wire connection (Kelvin connection) in order to eliminate the lead and contact resistance from the measurement.

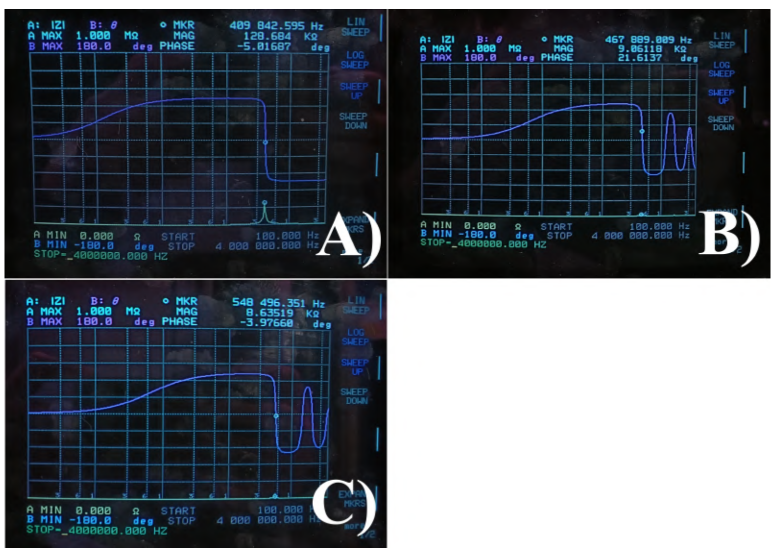

Figure 4.11: Magnitude and phase plotted for each coil of the sensor: remember, A) radial, B) poloidal, C) toroidal.

4.3.1 Equivalent coupling model

However, the installation of the sensors and the saddle loops (including the poloidal flux difference loops) on the vacuum vessel gives rise a mutual magnetic coupling between the coils and the copper shell of the vessel. Then, the measured inductance values of the coils will be different from their reference values, in a bandwidth from 100 Hz to 100 kHz. This is also due to a geometric coupling coefficient k, which depends on the "*footprint*" of the saddle loop installed on the shell.

Consider the equivalent model of a coil [20] with reference value L_c, coupled with the conducting shell with L_s self inductance and R_s resistance. $M = M_{12} = M_{21}$ is the mutual coupling between them. Remember that the mutual inductance between two generic circuits C_1 and C_2 is defined by the Neumann's formula:

$$M_{12} = \frac{\mu_0}{4\pi} \oint_{C_1} \oint_{C_2} \frac{d\bar{l}_1 \cdot d\bar{l}_2}{|\bar{r}_1 - \bar{r}_2|} \tag{4.26}$$

where μ_0 is the vacuum magnetic permeability, $d\bar{l}_1$ and $d\bar{l}_2$ are the infinitesimal increments of conductor segments, $\bar{r}_1$ and $\bar{r}_2$ are the positions of the segments in the space. The self inductance L is obtained by assuming $C_1 = C_2$ in the same formula.

The equation matrix is:

$$\begin{bmatrix} V_c \\ V_s \end{bmatrix} = \begin{bmatrix} j\omega L_c & j\omega M \\ j\omega M & R_s + j\omega L_s \end{bmatrix} \cdot \begin{bmatrix} I_c \\ I_s \end{bmatrix} \tag{4.27}$$

Assuming $V_s = 0$ since the conducting shell is short-circuited, the induced current will be

$$I_s = -\frac{j\omega M}{R_s + j\omega L_s} I_c \tag{4.28}$$

and the impedance seen from the coil

$$Z_{eff} = \frac{V_c}{I_c} = j\omega L_c - \frac{(j\omega M)^2}{R_s + j\omega L_s} \tag{4.29}$$

By separating real and imaginary parts of the impedance:

$$R_{eff} = \frac{\omega^2 M^2 R_s}{R_s^2 + (\omega L_s)^2}, \qquad L_{eff}(\omega) = L_c - \frac{\omega^2 M^2 L_s}{R_s^2 + (\omega L_s)^2} \tag{4.30}$$

Knowing that $R_s \ll \omega L_s$, the imaginary part becomes

$$L_{eff} \approx L_c - \frac{M^2}{L_s} \tag{4.31}$$

Finally, by introducing the geometric coupling coefficient:

$$k = \frac{M}{\sqrt{L_c L_s}} \tag{4.32}$$

the overall simplified relation is

$$L_{eff} \approx L_c(1 - k^2) \tag{4.33}$$

For this reason it is necessary to measure the series inductance of each sensor before and after the installation on the vacuum vessel.

4.3.2 LCR meter measurements

The LCR meter is a test equipment that basically measures the resistive, inductive and capacitive components of a given impedance. The instrument used in this experience is the GW Instek LCR-6300 shown in 4.12.

This instrument is used to evaluate both the longitudinal and shunt reactive components over a wide range of frequencies (from 10 Hz to 300 kHz) [21] by choosing the right equivalent circuit configuration, as shown in 4.13. Of course, before performing the measurement, the instrument must be calibrated in order to correct the stray admittance and residual impedance: short-circuit for the series components and open-circuit for the shunt ones.

Since the inductance values vary due to the mutual coupling with the vessel, the measurement must be performed when the coils are installed on a section of the conducting shell, as shown in 4.14. The inductance-resistance series configuration (L_s-R_s) is used.

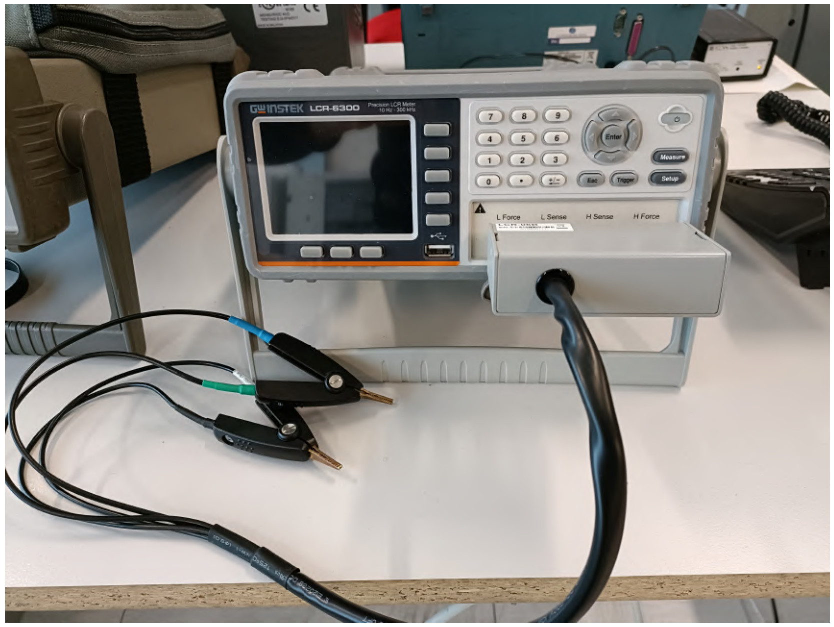

Figure 4.12: LCR meter instrument used in this experience.

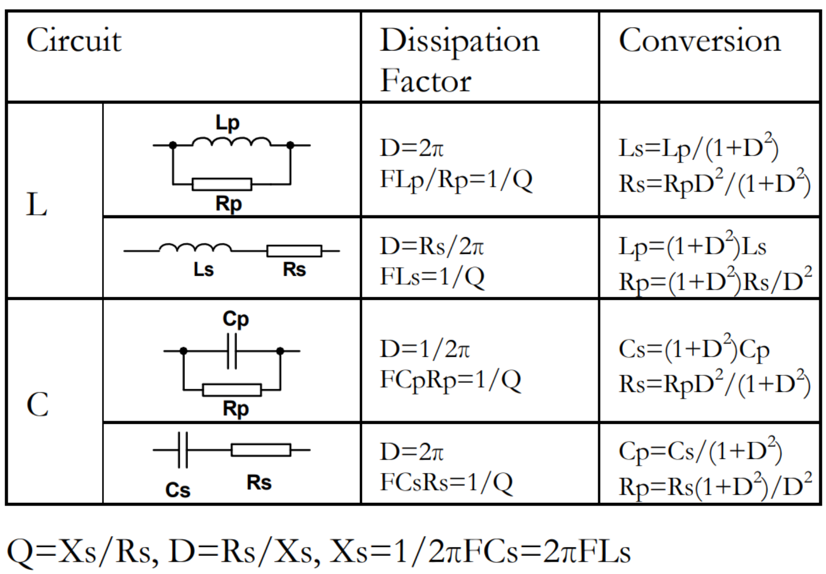

Circuit		Dissipation Factor	Conversion
L	Lp, Rp	D=2π FLp/Rp=1/Q	Ls=Lp/(1+D^2) Rs=RpD^2/(1+D^2)
	Ls, Rs	D=Rs/2π FLs=1/Q	Lp=(1+D^2)Ls Rp=(1+D^2)Rs/D^2
C	Cp, Rp	D=1/2π FCpRp=1/Q	Cs=(1+D^2)Cp Rs=RpD^2/(1+D^2)
	Cs, Rs	D=2π FCsRs=1/Q	Cp=Cs/(1+D^2) Rp=Rs(1+D^2)/D^2

Q=Xs/Rs, D=Rs/Xs, Xs=1/2πFCs=2πFLs

Figure 4.13: Possible circuit configurations evaluated by the LCR. Quality factor and dissipation factor are reported below the table.

From the following tables it is clear that the inductance of each coil decreases as the frequency increases.

Frequency $[Hz]$	Radial L_c $[mH]$
100.0	1.90844
150.0	1.78746
200.0	1.70550
300.0	1.60262
500.0	1.50578
1000.0	1.42751
2000.0	1.37802
5000.0	1.32087
10000.0	1.28899

Table 4.1: Measured series inductance values of the radial coil.

Frequency $[Hz]$	Saddle L_c $[\mu H]$
100.0	1.07972
150.0	1.00586
200.0	0.95920
300.0	0.90967
500.0	0.86080
1000.0	0.80105
2000.0	0.76139
5000.0	0.71182
10000.0	0.68107

Table 4.2: Measured series inductance values of the saddle coil.

Frequency $[Hz]$	Poloidal L_c $[\mu H]$
100.0	239.728
200.0	228.758
500.0	222.680
1000.0	219.842
2000.0	218.056
5000.0	216.092
10000.0	214.957
20000.0	214.187
50000.0	214.158
100000.0	217.236

Table 4.3: Measured series inductance values of the poloidal coil.

Frequency $[Hz]$	Toroidal L_c $[\mu H]$
100.0	184.924
200.0	180.806
500.0	174.670
1000.0	170.885
2000.0	168.263
5000.0	165.366
10000.0	163.682
20000.0	162.507
50000.0	161.874
100000.0	163.304

Table 4.4: Measured series inductance values of the toroidal coil.

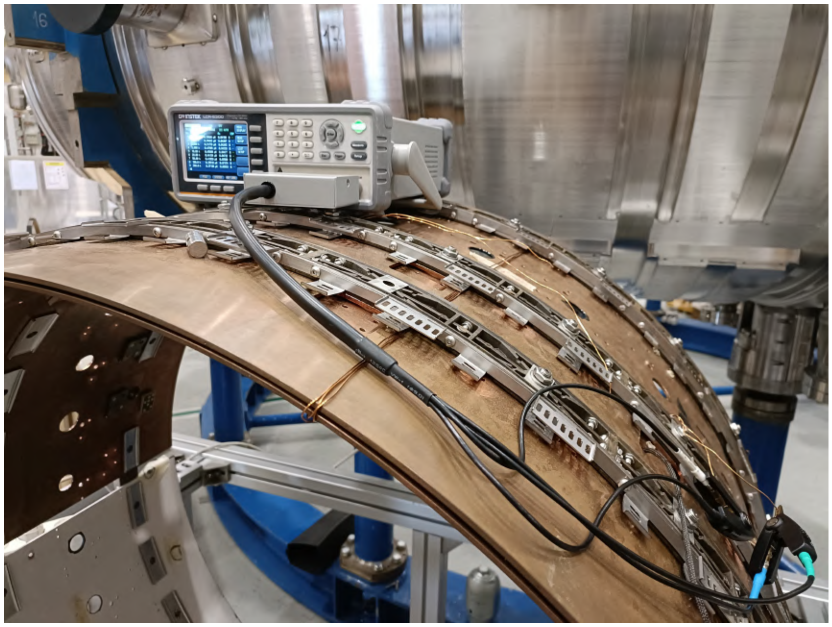

Figure 4.14: Coil inductance measurement setup.

4.4 Transmission line model

The transmission line connects the probes directly to the electronics input stage and it consists of a thin twisted pair cable, possibly with individual pair shielding. In the real application the lines typically have variable lengths (from tens to hundreds of meters) and, since the probes are installed inside the vacuum chamber, the cable must have good electrical and mechanical properties in order to sustain the harsh operating conditions. At high frequencies, the parasitic effects of the cable may introduce important inhomogeneities due to wave propagation and reflection effects.

An ideal transmission line can be modeled by means of a lumped parameters model with a series impedance $Z_s = R_s + j\omega L_s$ and a shunt impedance towards the ground, *i.e.*, the shield in the case of a cable, $Z_p = \frac{1}{j\omega C_p}$ (considering the conductance $G_p = 0$). The transmission line model exists in LTspice and it is shown in 4.15. The characteristic impedance of the transmission line can be calculated with the following expression:

$$Z_c = \frac{Z_0}{\pi\sqrt{\varepsilon_r}} \arccos\left(\frac{d}{\phi}\right) \tag{4.34}$$

where Z_0 is the characteristic impedance of free space ($\sim 376.73\ \Omega$), ε_r is the dielectric constant of the cable insulation, d is the distance between the conductors and ϕ is the diameter of the conductor. A much easier expression is based on the knowledge of the inductance and capacitance of the line:

$$Z_c = \sqrt{\frac{L_s}{C_p}} \tag{4.35}$$

If the Heaviside's condition is satisfied when $\frac{r}{l} = \frac{g}{c}$, the characteristic impedance becomes real and equal to that of an ideal line: this is the condition for a transmission line to be distortion-less.
In this thesis three different lengths for the transmission line were considered: (12.23 ± 0.02) $[m]$, (36.69 ± 0.06) $[m]$ and (61.15 ± 0.10) $[m]$.

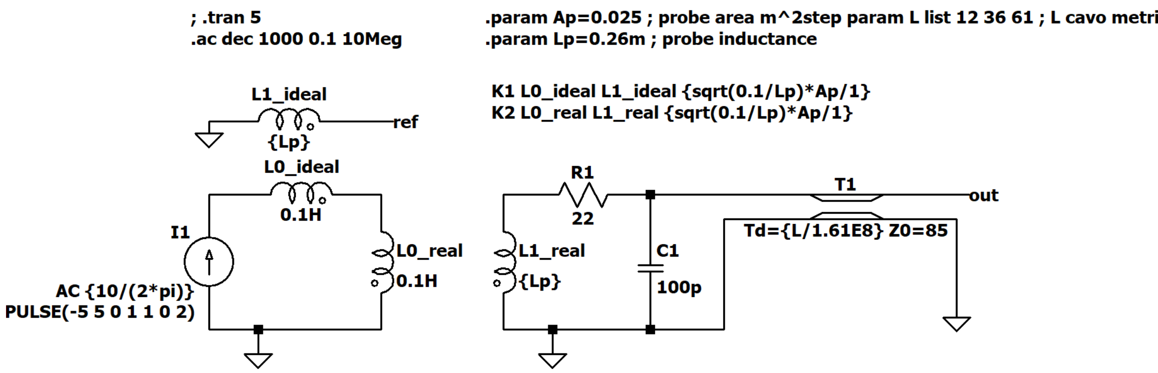

Figure 4.15: Transmission line model connected to the real probe model.

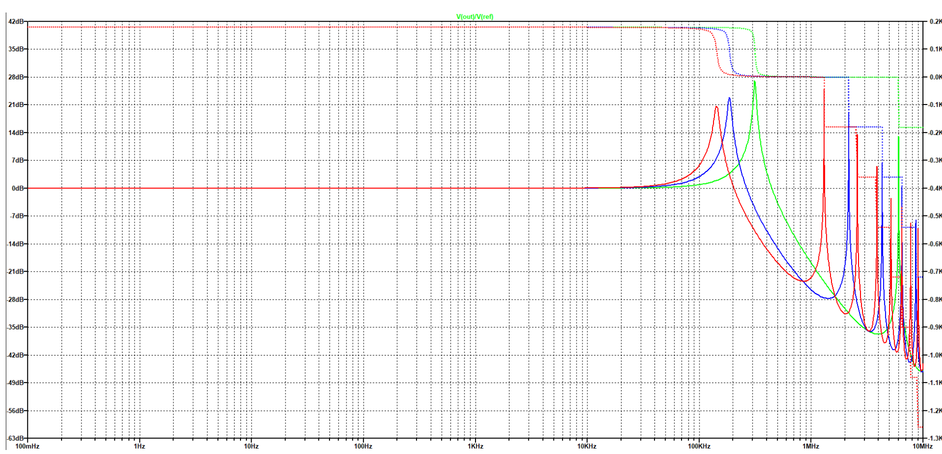

Figure 4.16: Frequency response of the unmatched line: the green plot represents the 12 m long cable, the blue one for the 36 m length and the red one for the 61 m length. Note that the plot is normalized to the reference voltage value of the ideal sensor.

However, in the LTspice simulations, a model with lumped parameters is adopted for the transmission line, thus the losses will be concentrated exclusively on the resistive and capacitive components external to the model.
Another simplification introduced is to consider the characteristic impedance Z_c of the transmission line to be constant: in fact, this hypothesis is consistent only up to 50 kHz (with an error lower than 5%); above 100 kHz, the error rapidly grows, exceeding 10% at 200 kHz. Therefore, the characteristic impedance is frequency-dependent.

4.4.1 LCR meter measurements

As already noted three different lengths for the transmission line were considered and they were obtained by connecting in series the conductors of the cable with a screwed terminal strip. The multi-conductor cable section is long 12 m, so three conductors connected in series in order to obtain 36 m and five for 61 m.

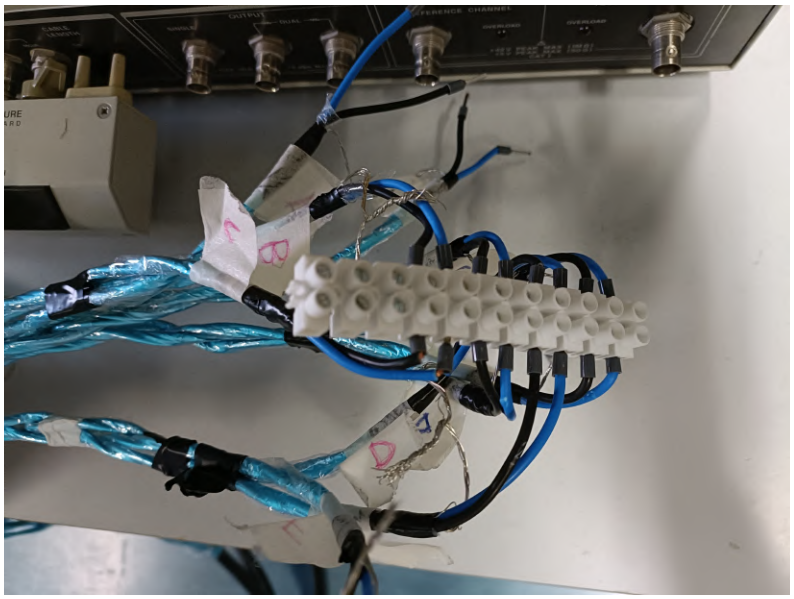

Figure 4.17: Terminal strip used to connect more cable sections in series.

Several measures were done with the LCR meter by considering two conductors per line, one conductor and the shield and both conductors and the shield. The LCR meter is set in L_s-R_s series configuration while the line is short-circuited in order to measure the inductance, and in C_p-R_p parallel configuration while the line is open-circuited in order to measure the stray capacitance.
After the data acquisition and plotting, the propagation time has been calculated for each length of cable, starting from the cut-off frequency.

Cable length d $[m]$	Cut-off frequency f_{cut} $[Hz]$	Propagation velocity v_{prop} $\left[\frac{km}{s}\right]$	Propagation time $[\mu s]$
12.23	3076250	150490.15	0.325
36.69	1005000	147493.80	0.995
61.15	620000	151652.00	1.613

Table 4.5: Propagation parameters for each length.

The propagation time is simply obtained with

$$t_{prop} = \frac{1}{f_{cut}} \tag{4.36}$$

while the propagation velocity is

$$v_{prop} = \frac{4 \cdot d \cdot f_{cut}}{1000} \tag{4.37}$$

Note that for this type of cable the propagation velocity is always equal to half the speed of light ($c \simeq 300.000\ \frac{km}{s}$), more or less.

The impedance analysis of the cable is shown in the following figures and a simulation was made by importing LTspice data into the Python script. This was made for each length of cable.

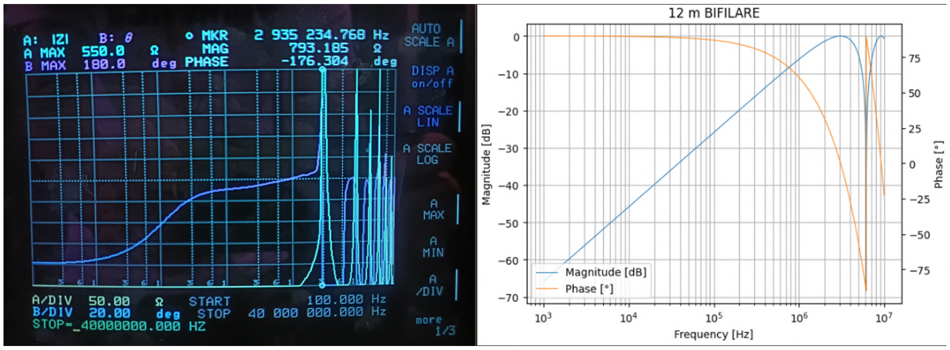

Figure 4.18: Impedance analysis performed with the HP4194A (on the left) and the Python simulation (on the right) for the 12 m long cable section.

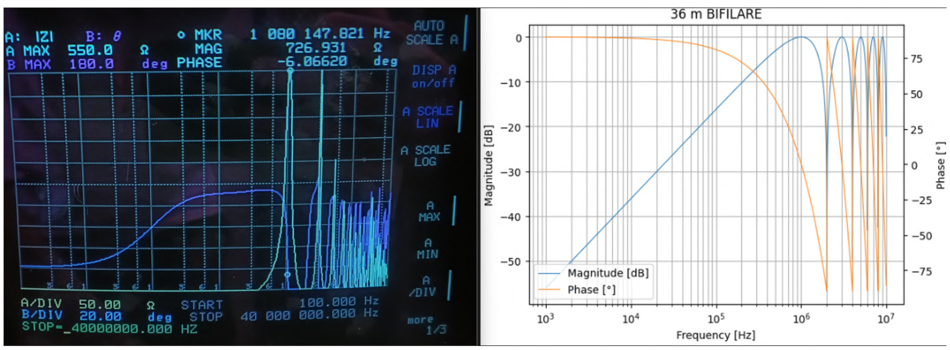

Figure 4.19: Impedance analysis and the Python simulation for the 36 m long cable section.

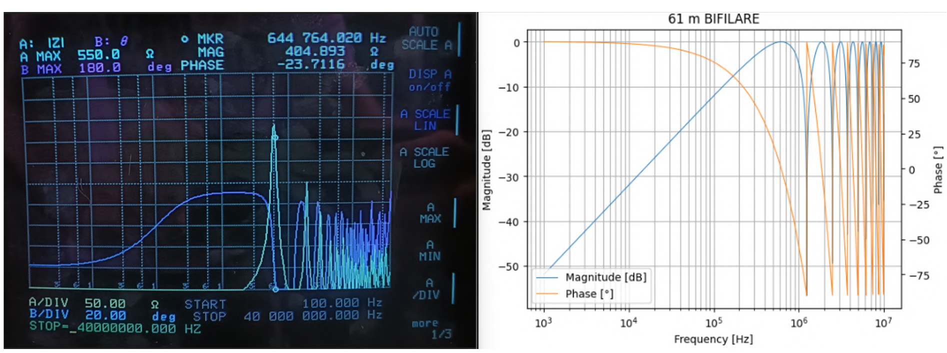

Figure 4.20: Impedance analysis and the Python simulation for the 61 m long cable section.

Frequency $[Hz]$	C_p $[nF]$	L_s $[\mu F]$	D $[-]$	Z_c $[\Omega]$	Configuration
500	1.139	9.019	0.00895	88.985	Double-wired
1000	1.137	8.812	0.00654	88.035	Double-wired
2000	1.137	8.823	0.00516	88.090	Double-wired
5000	1.131	8.798	0.00410	88.198	Double-wired
10000	1.128	8.819	0.00247	88.421	Double-wired
20000	1.126	8.643	0.00081	87.612	Double-wired
50000	1.125	8.201	0.00080	85.380	Double-wired
100000	1.126	7.391	0.00159	81.018	Double-wired
200000	1.135	6.521	0.00157	75.798	Double-wired
500	2.264	6.365	0.00796	53.023	Single-wired to shield
1000	2.557	6.361	0.00759	49.877	Single-wired to shield
2000	2.248	6.362	0.00786	53.198	Single-wired to shield
5000	2.239	6.346	0.00733	53.238	Single-wired to shield
10000	2.233	6.293	0.00676	53.087	Single-wired to shield
20000	2.227	6.105	0.00676	52.358	Single-wired to shield
50000	2.221	5.344	0.00696	49.052	Single-wired to shield
100000	2.216	4.429	0.00765	44.706	Single-wired to shield
200000	2.218	3.647	0.00870	40.550	Single-wired to shield
500	4.319	4.081	0.00871	30.739	Double-wired to shield
1000	4.307	4.079	0.00871	30.774	Double-wired to shield
2000	4.293	4.077	0.00715	30.817	Double-wired to shield
5000	4.276	4.062	0.00681	30.821	Double-wired to shield
10000	4.264	4.013	0.00634	30.678	Double-wired to shield
20000	4.253	3.842	0.00650	30.056	Double-wired to shield
50000	4.242	3.184	0.00697	27.397	Double-wired to shield
100000	4.236	2.490	0.00781	24.245	Double-wired to shield
200000	4.246	1.998	0.00999	21.692	Double-wired to shield

Table 4.6: Measured series inductance and shunt capacitance considering the 12 m cable section. The dissipation factor and characteristic impedance for each configuration are then calculated.

Frequency $[Hz]$	C_p $[nF]$	L_s $[\mu F]$	D $[-]$	Z_c $[\Omega]$	Configuration
500	3.555	26.884	0.00794	86.962	Double-wired
1000	3.543	26.876	0.00735	87.096	Double-wired
2000	3.531	26.874	0.00652	87.240	Double-wired
5000	3.519	26.826	0.00593	87.311	Double-wired
10000	3.510	26.757	0.00501	87.310	Double-wired
20000	3.505	26.428	0.00454	86.834	Double-wired
50000	3.508	24.940	0.00427	84.318	Double-wired
100000	3.535	22.740	0.00602	80.205	Double-wired
200000	3.641	20.407	0.01485	74.865	Double-wired
500	6.928	18.841	0.00896	52.149	Single-wired to shield
1000	6.901	18.840	0.00836	52.250	Single-wired to shield
2000	6.876	18.835	0.00760	52.338	Single-wired to shield
5000	6.849	18.793	0.00731	52.382	Single-wired to shield
10000	6.828	18.637	0.00696	52.245	Single-wired to shield
20000	6.814	18.085	0.00731	51.518	Single-wired to shield
50000	6.809	15.843	0.00930	48.237	Single-wired to shield
100000	6.846	13.210	0.01407	43.927	Single-wired to shield
200000	7.020	11.142	0.02619	39.839	Single-wired to shield
500	12.903	12.022	0.00882	30.524	Double-wired to shield
1000	12.858	12.013	0.00822	30.566	Double-wired to shield
2000	12.813	12.011	0.00741	30.617	Double-wired to shield
5000	12.763	11.975	0.00719	30.631	Double-wired to shield
10000	12.726	11.842	0.00698	30.505	Double-wired to shield
20000	12.701	11.369	0.00747	29.919	Double-wired to shield
50000	12.700	9.494	0.01016	27.342	Double-wired to shield
100000	12.776	7.413	9.91669	24.088	Double-wired to shield
200000	13.120	5.939	0.03293	21.276	Double-wired to shield

Table 4.7: Measured series inductance and shunt capacitance considering the 36 m cable section.

Frequency $[Hz]$	C_p $[nF]$	L_s $[\mu F]$	D $[-]$	Z_c $[\Omega]$	Configuration
500	6.039	44.416	0.00863	85.760	Double-wired
1000	6.018	44.420	0.00769	85.914	Double-wired
2000	5.999	44.421	0.00694	86.051	Double-wired
5000	5.977	44.385	0.00647	86.174	Double-wired
10000	5.962	44.236	0.00598	86.137	Double-wired
20000	5.956	43.726	0.00618	85.683	Double-wired
50000	5.982	41.466	0.00830	83.257	Double-wired
100000	6.107	38.382	0.01531	79.277	Double-wired
200000	6.624	36.118	0.04229	73.842	Double-wired
500	11.543	31.095	0.00946	51.909	Single-wired to shield
1000	11.499	31.081	0.00876	51.987	Single-wired to shield
2000	11.458	31.084	0.00793	52.081	Single-wired to shield
5000	11.411	31.013	0.00772	52.135	Single-wired to shield
10000	11.378	30.758	0.00766	51.989	Single-wired to shield
20000	11.364	29.861	0.00860	51.270	Single-wired to shield
50000	11.414	26.222	0.01366	47.939	Single-wired to shield
100000	11.640	22.036	0.02735	43.510	Single-wired to shield
200000	12.533	19.273	0.06885	39.219	Single-wired to shield
500	21.366	20.323	0.00889	30.841	Double-wired to shield
1000	21.290	20.318	0.00828	30.892	Double-wired to shield
2000	21.218	20.318	0.00750	30.945	Double-wired to shield
5000	21.138	20.257	0.00748	30.957	Double-wired to shield
10000	21.082	20.034	0.00775	30.827	Double-wired to shield
20000	21.063	19.255	0.00906	30.235	Double-wired to shield
50000	21.172	16.136	0.01618	27.607	Double-wired to shield
100000	21.597	12.639	0.03497	24.191	Double-wired to shield
200000	23.132	10.272	0.08661	21.073	Double-wired to shield

Table 4.8: Measured series inductance and shunt capacitance considering the 61 m cable section.

Chapter 5

Electrical design of the matching circuit

5.1 Adapter circuits

Now that the transmission line has been inserted into the model, a matching circuit must be sized to ensure minimal attenuation for signals in the acquisition bandwidth and maximum attenuation for the resonance peaks at high frequencies. The simplest solution is to place a shunted termination resistor after the transmission line with the value equal to the characteristic impedance: in this way, the line is certainly matched, but the acquired signal is significantly attenuated, as shown in 5.2.

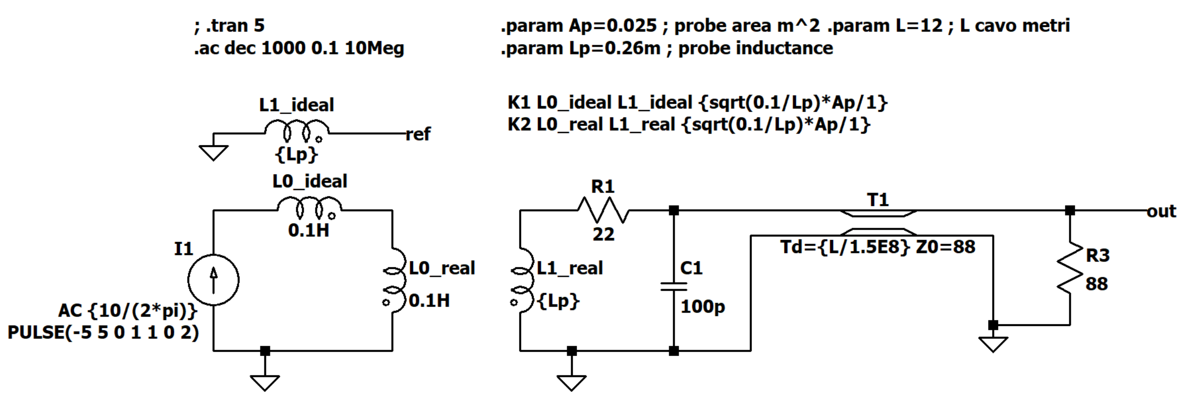

Figure 5.1: Model with 88 Ω termination resistance, considering the 12 m transmission line.

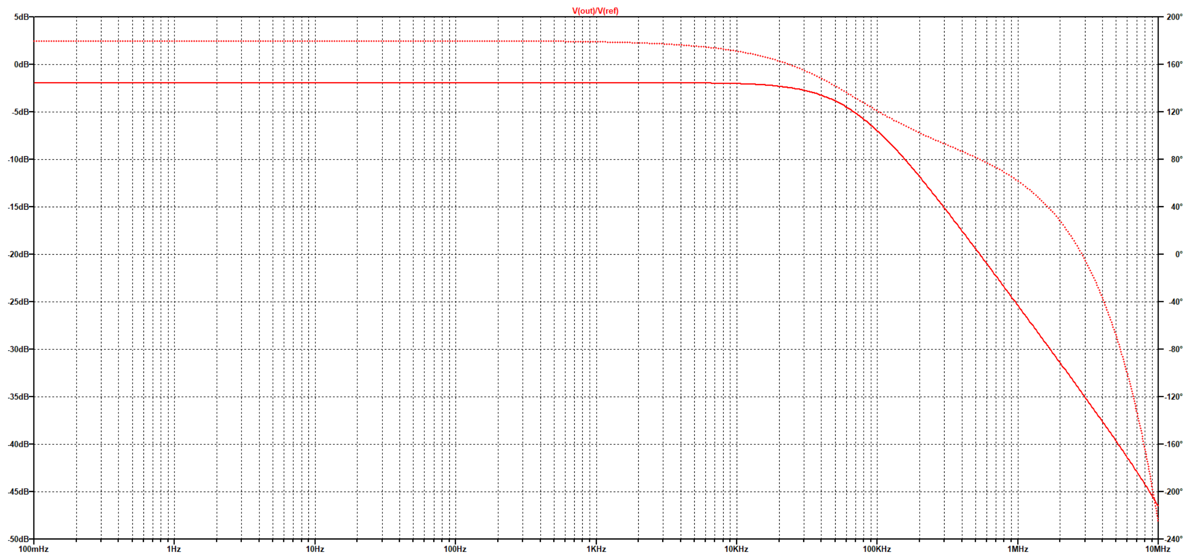

Figure 5.2: Frequency response of the line with the simple resistance matching, the peaks at high frequencies are eliminated but the signals are significantly attenuated in the acquisition bandwidth.

A more appropriate solution involves using a larger shunted resistance as termination (for example, a 2.2 $k\Omega$ resistance has been used in 5.3): in this way, it is possible to reduce the resonance effect and minimize the attenuation within the measurement band.
In the first solution, different values of termination resistance must be used for each length of the transmission line and it would create a resistive voltage divider with an unpredictable value, resulting in an excessive workload, while the second solution, minimizing the attenuation in the measurement bandwidth, reduces effects on the signal due to variations and tolerances in the line impedance. However, the termination resistance value varies with temperature, so, perfect matching is not guaranteed in any case.

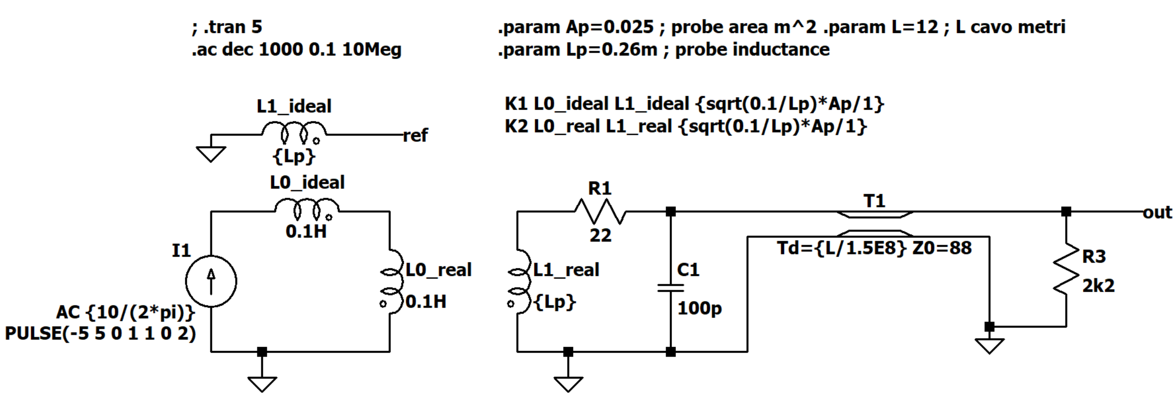

Figure 5.3: Model with 2.2 $k\Omega$ termination resistance, always considering the 12 m transmission line.

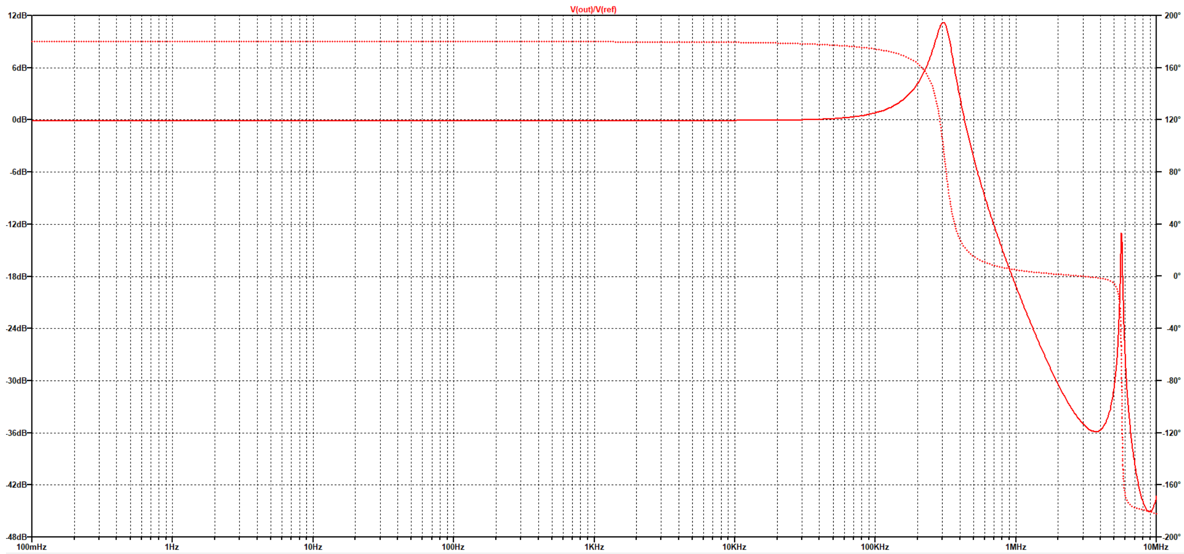

Figure 5.4: In this case, the resonance effect reappears but with lower magnitude, making it more manageable. On the other hand, the signal within the acquisition band is less attenuated.

5.1.1 Snubbers

Although, the best solution involves simple snubber circuits (resistance-capacitor series). In this way, the impedance is high at low frequencies, while at high frequencies it will be equal to the value of the resistance, which is sized in order to be as close as to the impedance to match. For this thesis, it has been decided to use two snubber circuits in parallel connection, tuned at different cut-off frequencies: the one with lower cut-off frequency eliminates the main resonant peak in the measurement bandwidth, while the other one attenuates residual peaks at very high frequencies. The cut-off frequency of a snubber is simply given by the following relation:

$$f_c = \frac{1}{2\pi RC} \tag{5.1}$$

The same components were chosen for the toroidal and poloidal adapters since the two sensors share quite similar electrical and geometrical parameters: for the first snubber $R_1 = 180\ \Omega$ and $C_1 = 1.5\ nF$, resulting in $f_{c_1} \simeq 589.46\ kHz$, while for the second one $R_2 = 180\ \Omega$ and $C_2 = 180\ nF$, resulting in $f_{c_2} \simeq 4.912\ kHz$. These parameters work for all the three cable lengths previously considered.

For the radial adapter only the two capacitor values must be changed, and so the cut-off frequencies: $C_1 = 47\ nF$ and $C_2 = 470\ nF$, resulting in $f_{c_1} \simeq 18.813\ kHz$ and $f_{c_2} \simeq 1.881\ kHz$.

For the saddle coil adapter just one snubber to attenuate high frequency peaks is needed: $R = 90\ \Omega$ and $C = 100\ nF$, tuned at $f_c \simeq 17.684\ kHz$.

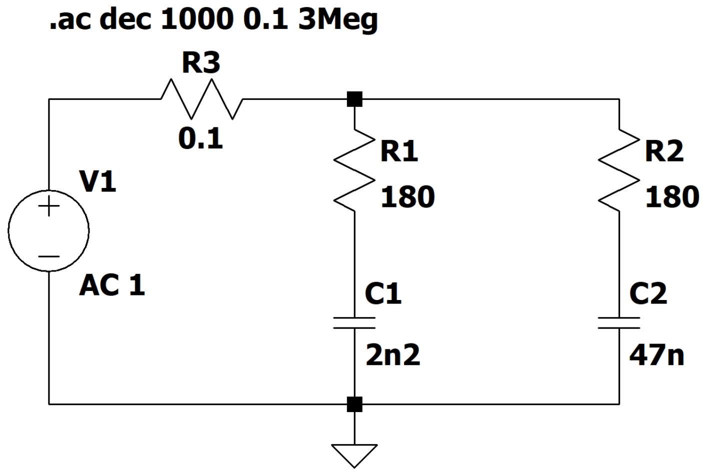

Figure 5.5: Basic circuit with two RC snubbers for the toroidal and poloidal components.

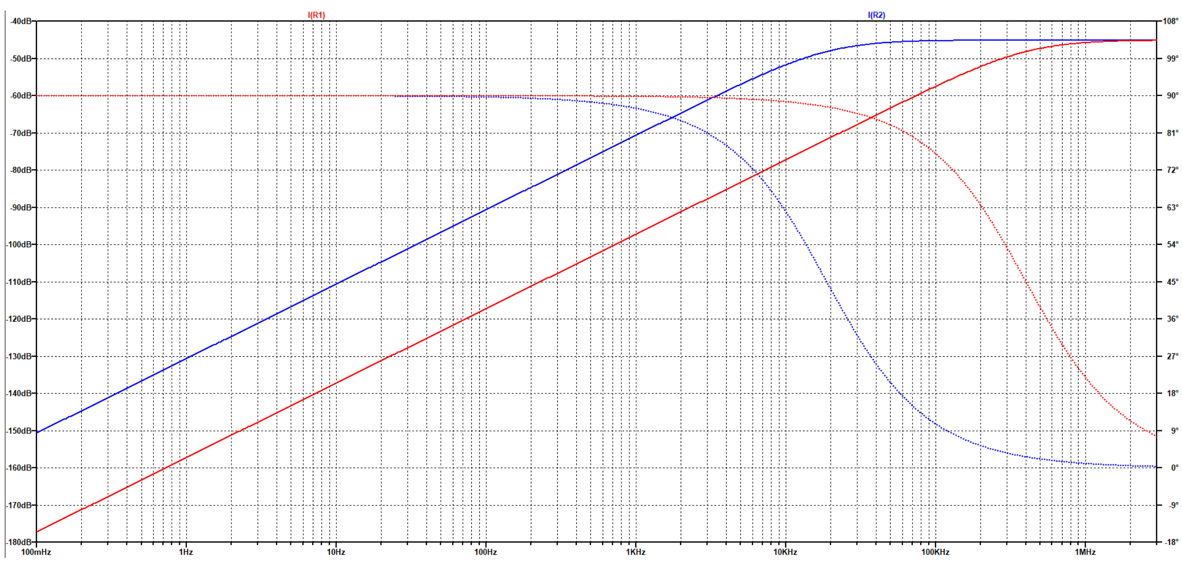

Figure 5.6: Magnitude and phase of the currents flowing in the snubbers. Note that the cut-off frequencies coincide to the ones calculated before.

As shown in 5.8, the two RC snubbers eliminates almost totally the resonance peaks, without introducing any attenuation on the measurement bandwidth. However, the frequency response is not as smooth as in 5.2, where a termination resistor with the same value of the characteristic impedance has been used: this is due to the choice of standard commercial values for resistors and capacitors, which do not perfectly match the characteristic impedance of the transmission line. A more precise sizing would be possible using variable components.

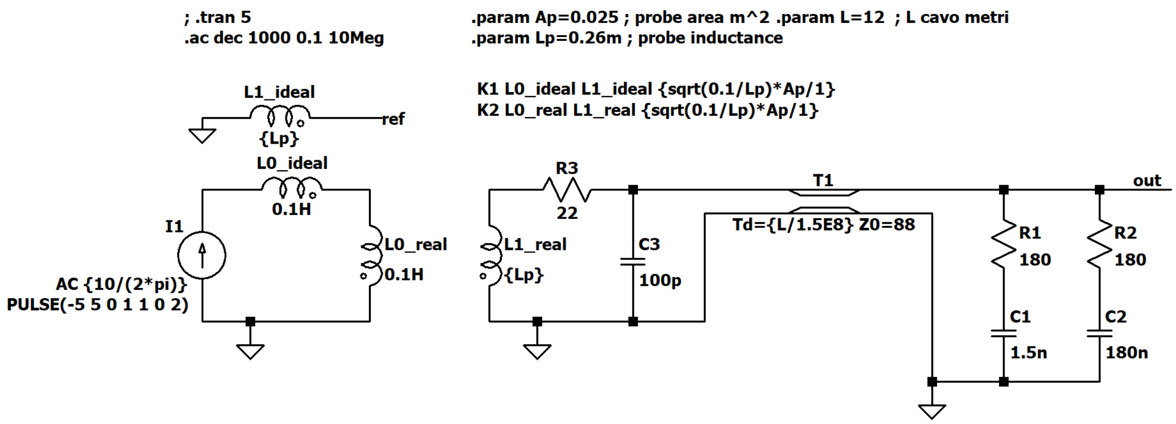

Figure 5.7: Previous toroidal and poloidal model after the connection of the snubbers.

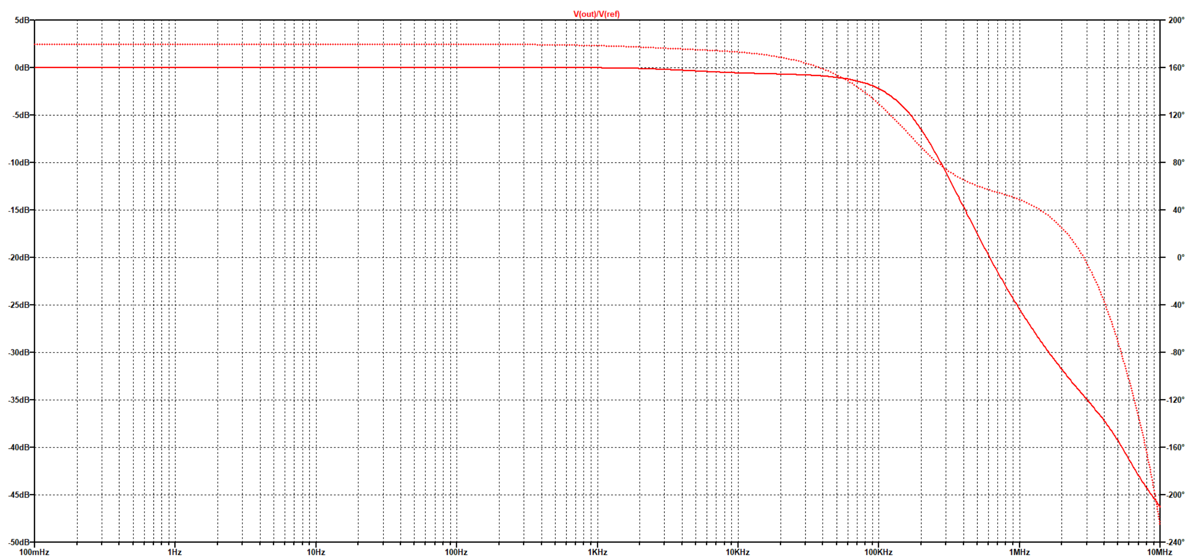

Figure 5.8: Effect of the snubbers on the resonance peaks.

5.1.2 Attenuator

After the snubber section, the signal experiences a voltage amplification phenomenon near the cut-off frequency, showed in 5.22. For this reason the two low-pass filters in 5.9 have been designed: differently from the high-level channel, the low-level channel gives a further contribution in the attenuation of $\sim 6\ dB$.

Since the signal is amplified just before the cut-off frequency, the filter must attenuate with a rate of $\sim 20\ \frac{dB}{dec}$ in the decade between 1 kHz and 10 kHz. Then, the gain will be flat again. The low-pass filter contribution on the overall frequency response is very clear in 5.14 and 5.15.

For the radial component and saddle coils a mere voltage divider is sufficient, as shown in 5.12 and 5.13, respectively.

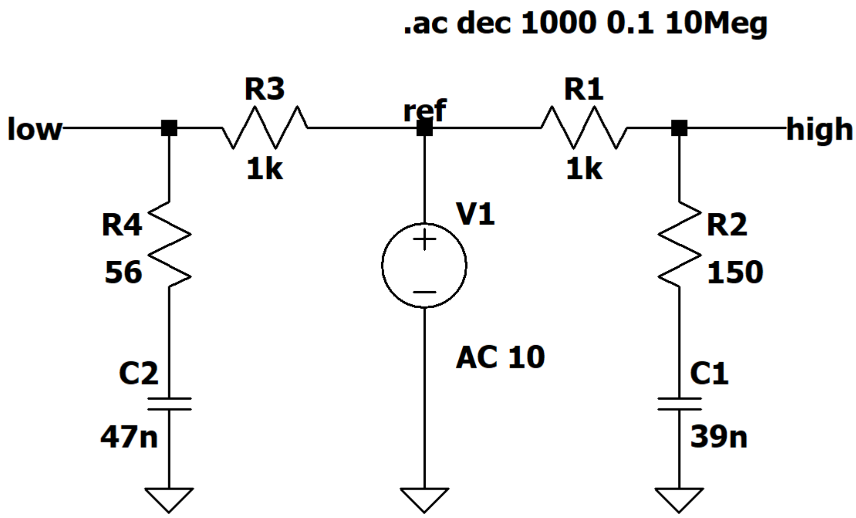

Figure 5.9: Low level low-pass filter on the left branch and high level low-pass filter on the right branch.

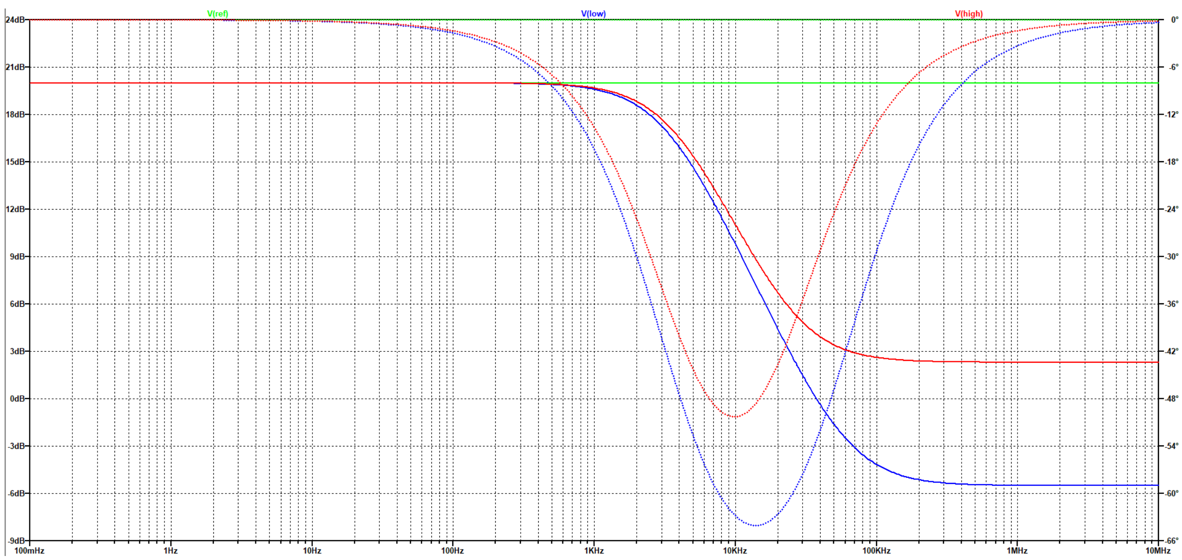

Figure 5.10: The attenuation introduced by the low level low-pass filter is plotted in blue, while the high level one is plotted in red.

In the LTspice models, for each type of adapter circuit, a channel selector has been added just after the attenuators, at the very end of the complete acquisition chain: the downstream load can be switched between 1 $k\Omega$, in order to simulate the integrator input impedance, and 0.1 $G\Omega$ for an open circuit.

5.1.3 Complete adapter models

Some sensor and transmission line parameters have been changed in order to obtain a result closer to the real model of the acquisition line.

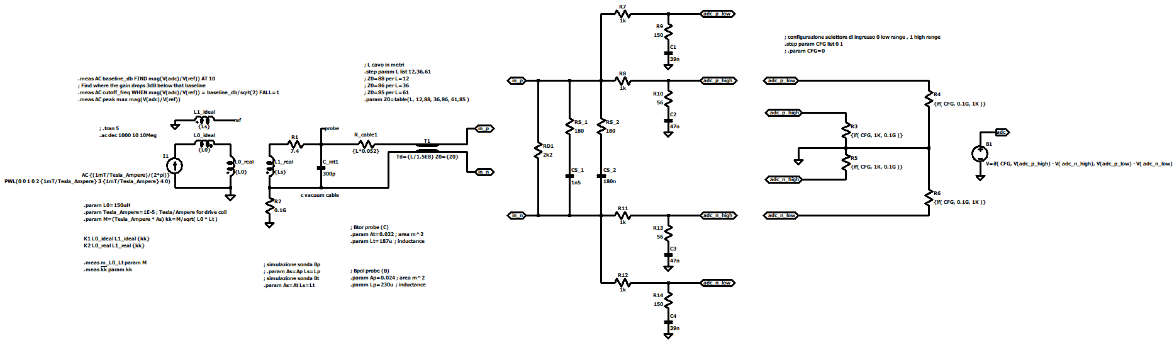

Figure 5.11: Complete scheme of the adapter circuit for both toroidal and poloidal sensors. In order to change the sensor parameters from toroidal to poloidal (or vice versa) the values directives must be commented or changed.

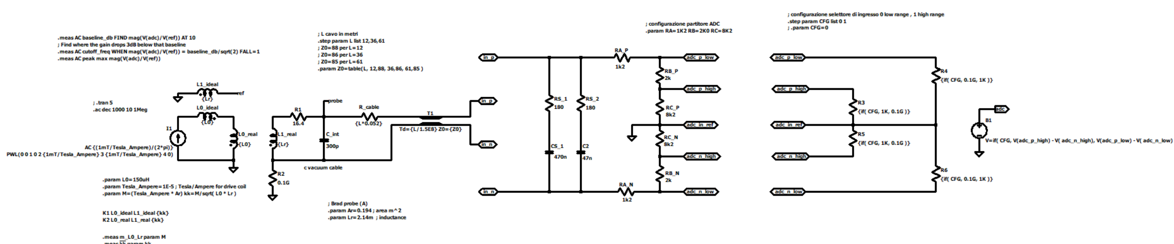

Figure 5.12: Complete scheme of the adapter circuit for the radial component sensor. Note that the low-pass filter has been changed with a voltage divider.

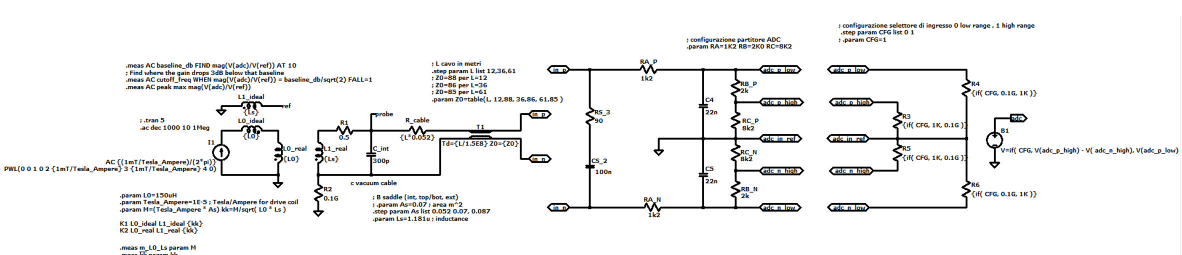

Figure 5.13: Complete scheme of the adapter circuit for the saddle coils. Note that two 22 nF capacitors have been placed in parallel to the attenuators (both low and high level input channels) in order to obtain a cut-off frequency of ~ 10 kHz in the response.

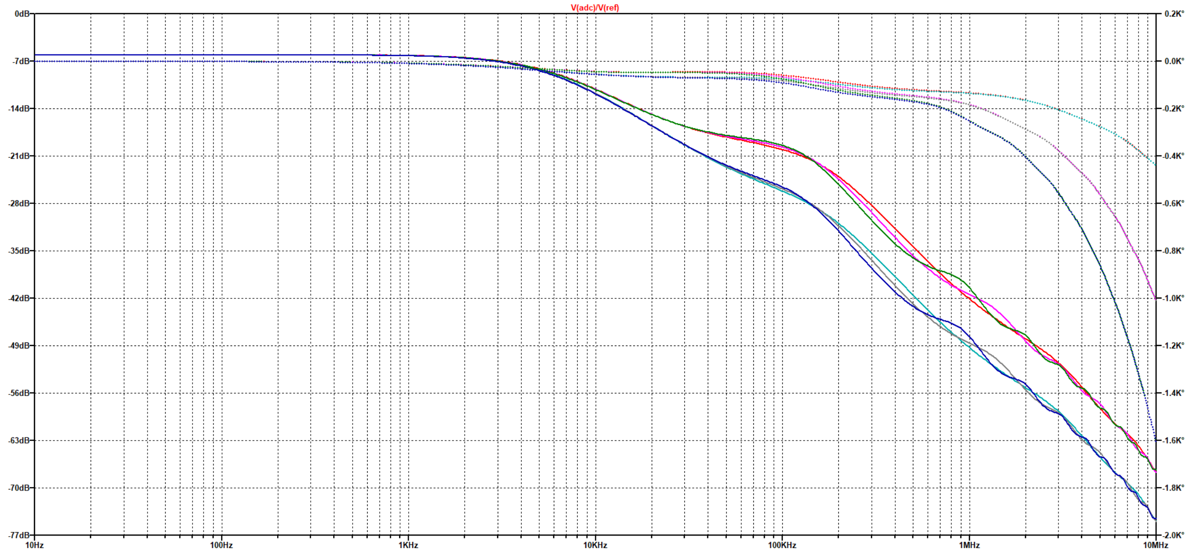

Figure 5.14: Frequency response for the toroidal component sensor complete chain, a first attenuation of the measurement bandwidth becomes at $\sim 10\ kHz$, while the cut-off frequency is at $\sim 100\ kHz$. Note that this adapter model works well with all the three analyzed cable lengths.

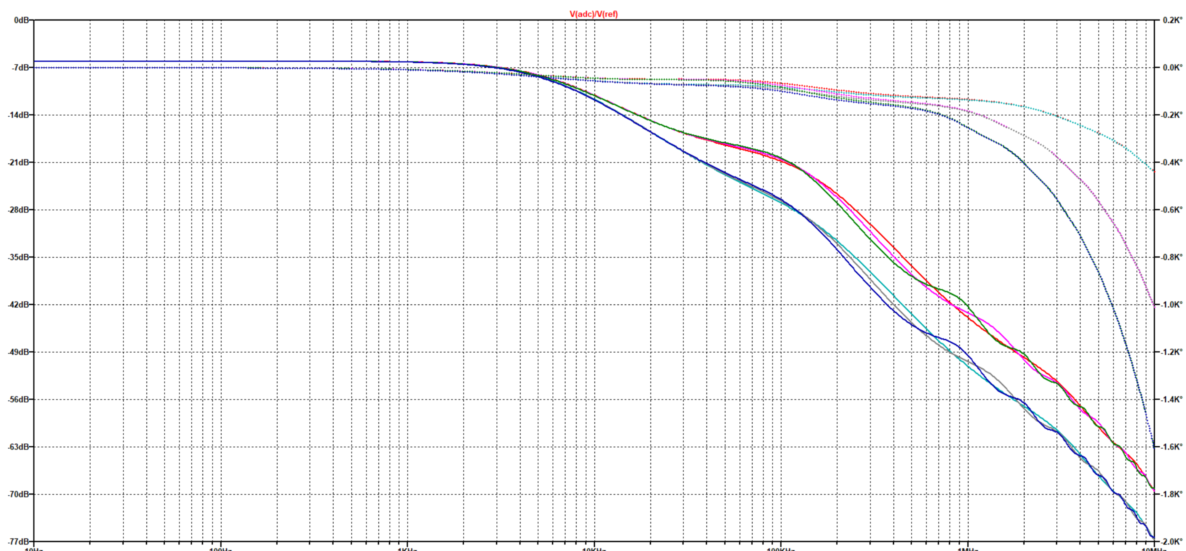

Figure 5.15: Frequency response for the poloidal component sensor complete chain, very similar to the toroidal one.

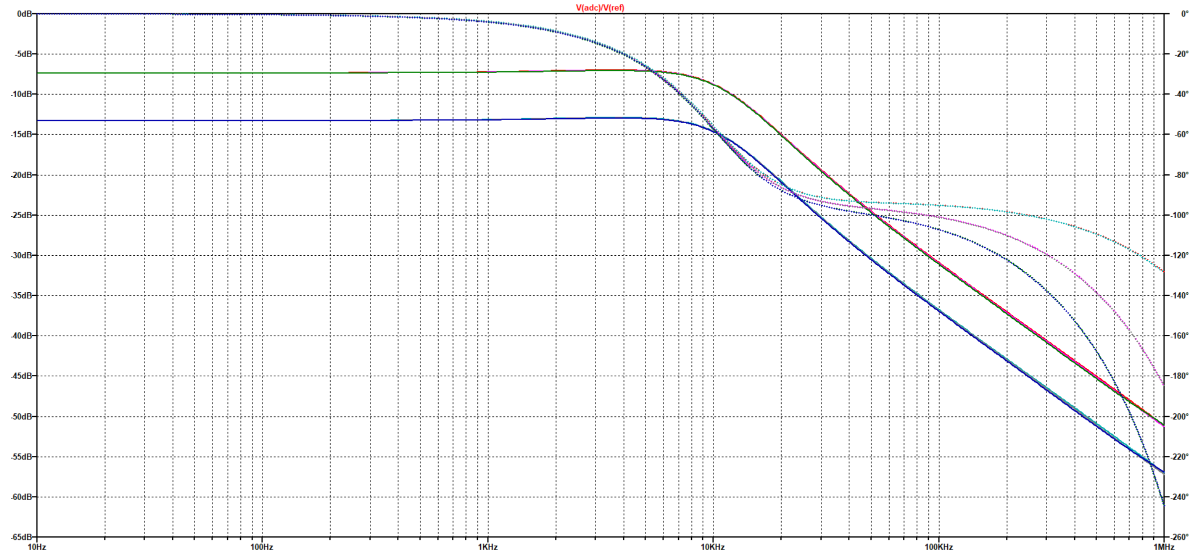

Figure 5.16: Frequency response for the radial component sensor complete chain.

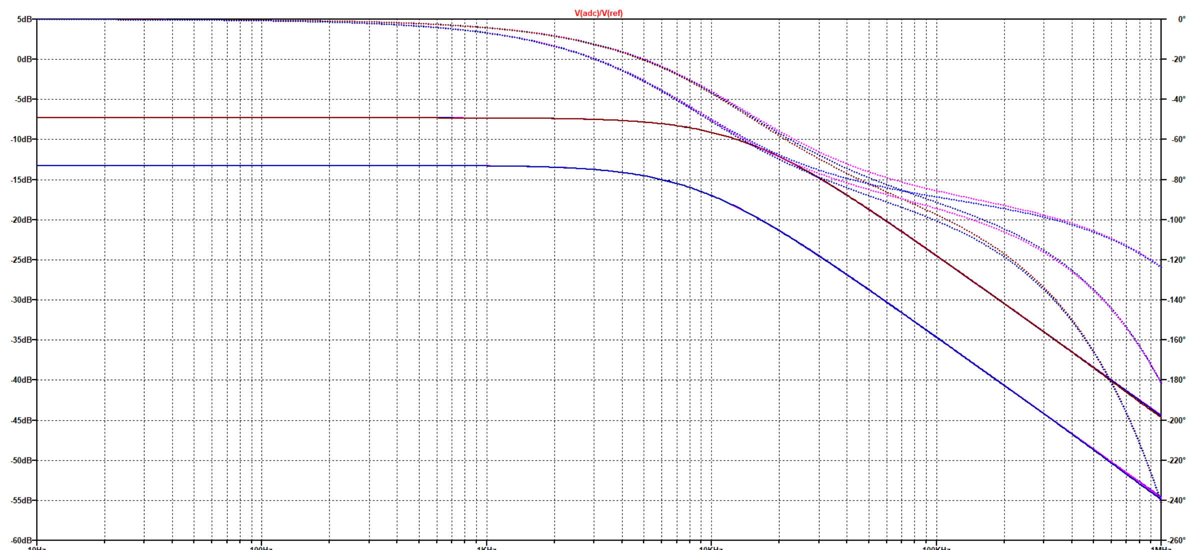

Figure 5.17: Frequency response for the saddle coil complete chain.

For this thesis work, a measurement bandwidth of 100 kHz was requested for the toroidal and poloidal components, with an initial attenuation of ~ 10 dB starting from 10 kHz. A smaller bandwidth is sufficient for the radial component and saddle coils, so the cut-off frequency is now at 10 kHz. The low level channel further attenuates the signal by 6 dB with respect to the high level one.

5.2 Results using a sampled plasma current signal

Consider the toroidal and poloidal adapter in 5.11, the ideal current generator that simulates an alternating current ranging from 10 Hz to 10 MHz induced in the inductive sensor is now replaced with a toroidal component of sampled plasma current signal, as shown in 5.18. LTspice can also generate voltage waves from WAV (Wave Audio File Format) audio files.

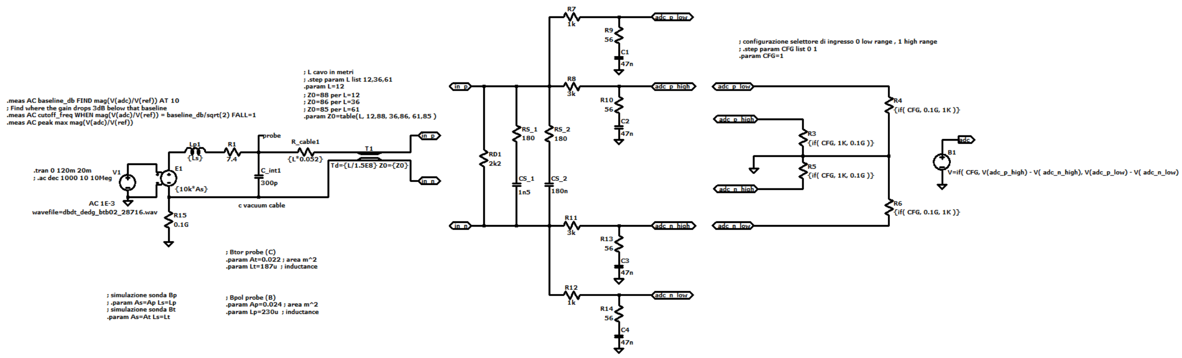

Figure 5.18: The ideal current source has been changed with a sampled plasma current signal in WAV audio format.

As shown in 5.19, the voltage induced across the inductive sensor can reach peaks of $\sim 80\ V$ or even higher. The peaks can damage the components inside the integration device downstream the entire acquisition chain, for this reason the design of an attenuator circuit is mandatory in order to bring the voltage signal at a reasonable level and compatible with the electronics, without being distorted.

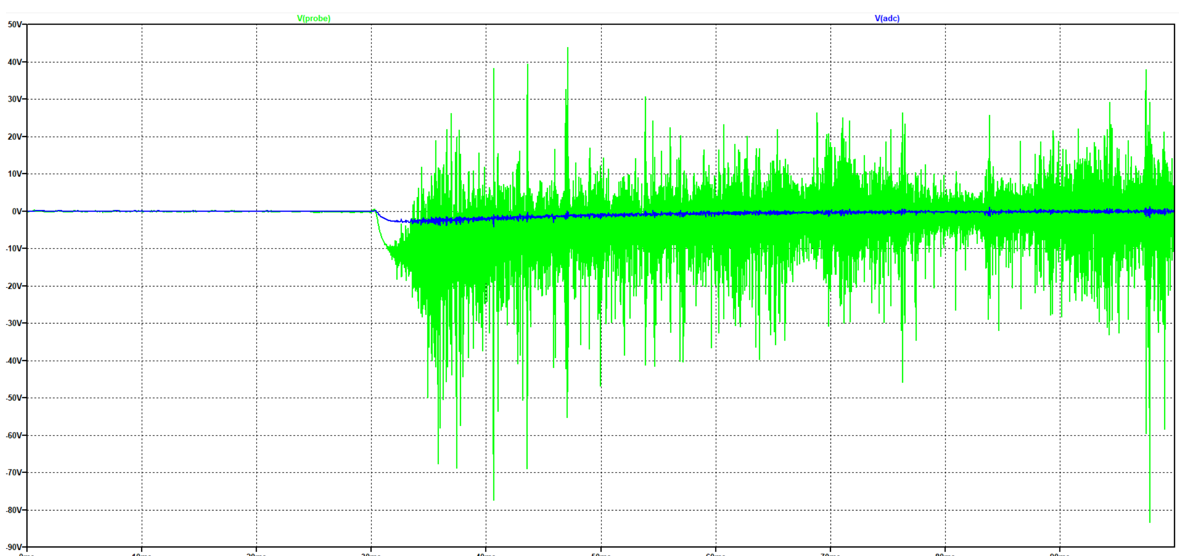

Figure 5.19: The sampled signal (in green) presents dangerous peaks for the downstream electronics, it must be attenuated (in blue) before integration.

Using a Python script to extract the LTspice simulation results, the following plots were made. The three voltage waveforms in 5.21 show that the output signal after the attenuator stage is now in a $\pm 5\ V$ range, resulting compatible with the integrator electronics. In 5.22 a spectral density analysis has been made: it is clear that the signal experiences a voltage amplification at high frequencies, just before the cut-off frequency at $\sim 100\ kHz$. However the spectral density of the signal after the attenuator stage appears to be more constant until the cut-off frequency.

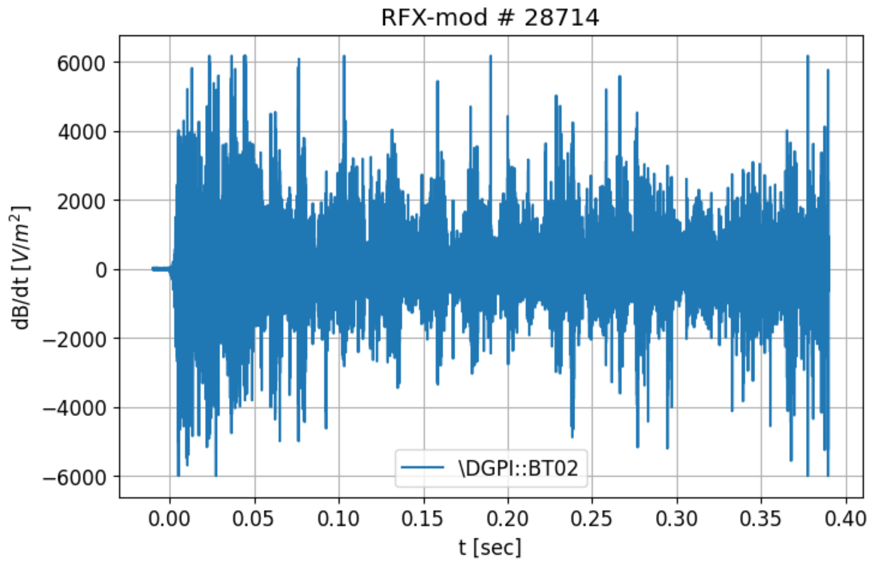

Figure 5.20: Magnetic field variation over time measured across the inductive sensor. This is a sampled signal of the toroidal component of the magnetic field, generated by plasma current.

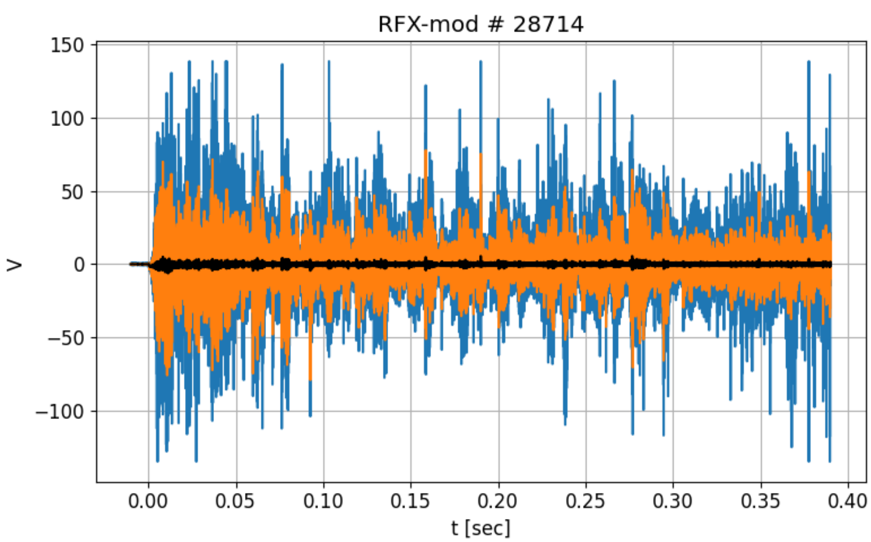

Figure 5.21: In blue, the voltage measured on the inductive sensor. In orange, the signal magnitude after the two snubbers. In black, the output signal after the attenuator stage.

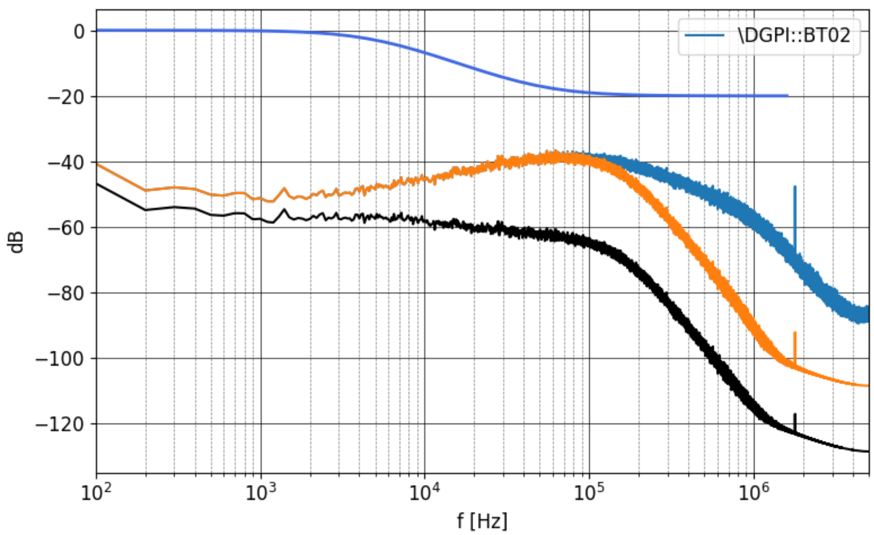

Figure 5.22: Spectral densities of the three signals just presented in the previous figure. Note that the attenuator eliminates the amplification of the signal just before the cut-off frequency.

5.3 Realization and validation of the adapter circuit

After the electrical design, the entire adapter circuit must be finally realized on a circuit board and connected between the transmission line termination and the integrator electronics. The circuit board, shown in 5.23, is a small sized chip with pins installed in a dedicated slot inside the integration device case, where SMD (Surface-Mount Device) components will be soldered on its surface in order to save space.

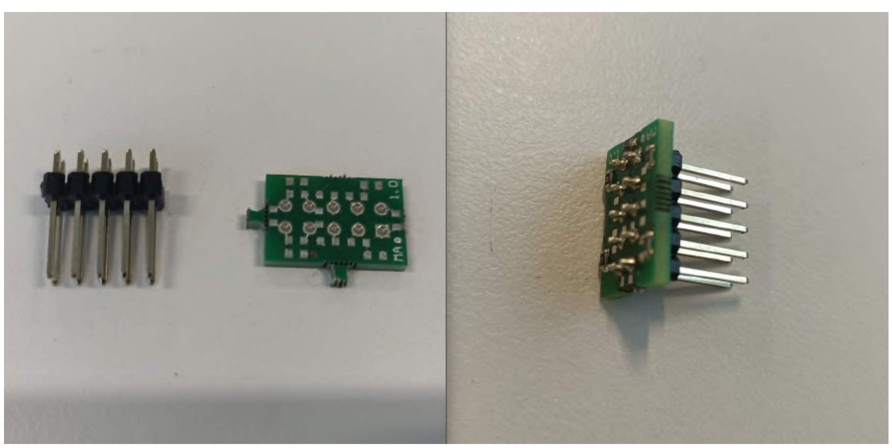

Figure 5.23: Circuit board for the SMD components. On the right another example of the board with pins already soldered.

For sake of simplicity, the same circuit has been realized by soldering 1/2 W components on a larger board, like in 5.25, where also the transmission line ends (with the inductive sensor connected on the opposite ends) and output BNC connections will be be soldered on the rear of the circuit in order to perform the final measure with the HP4194A impedance analyzer.

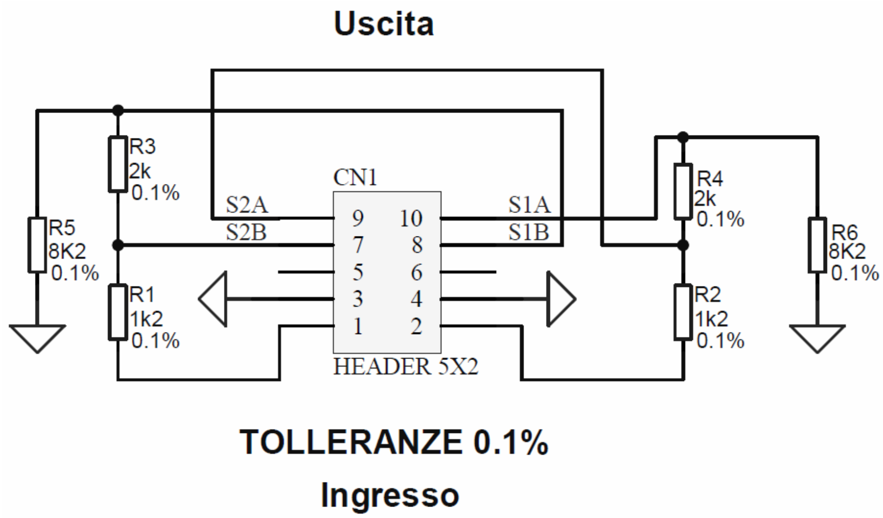

Figure 5.24: Pinout of the circuit board with the attenuator stage resistors.

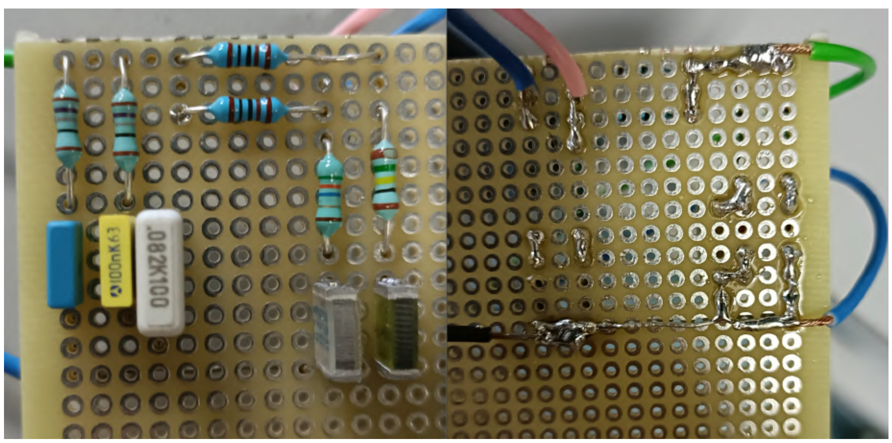

Figure 5.25: Front side (on the left) and back side (on the right) of the adapter circuit for the toroidal component on a larger circuit board.

Finally, 5.27 shows that the expected results are obtained for the physically realized adapter circuit: the frequency response starts flat and then the attenuator stage introduces a small attenuation of the signal in the decade between 10 kHz and 100 kHz.

However, it is clear that some resonance peaks are still present at very high frequencies: these are due to a minor reflection phenomenon introduced by the length of the enamelled copper wire that composes the inductive sensor and its short $\sim 10\ cm$ transmission line. It might be possible to compensate also these peaks by realizing more filters, matched with the impedance of the sensor, but the overall adapter circuit will be excessively complex.

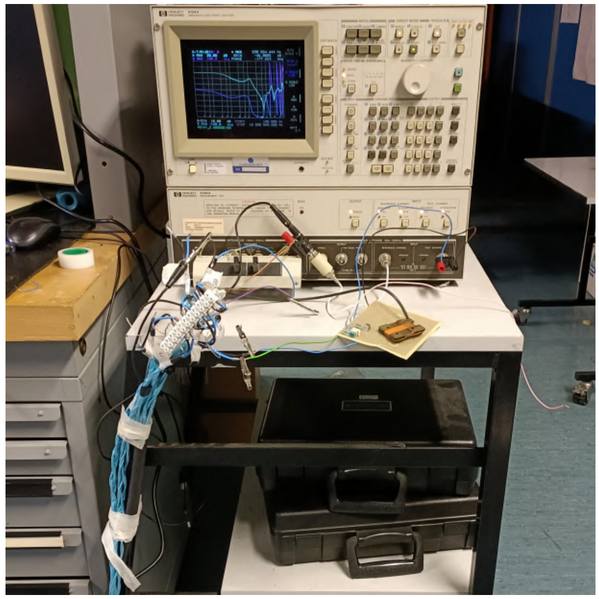

Figure 5.26: Impedance measurement setup with HP4194A with the entire acquisition line and adapter circuit.

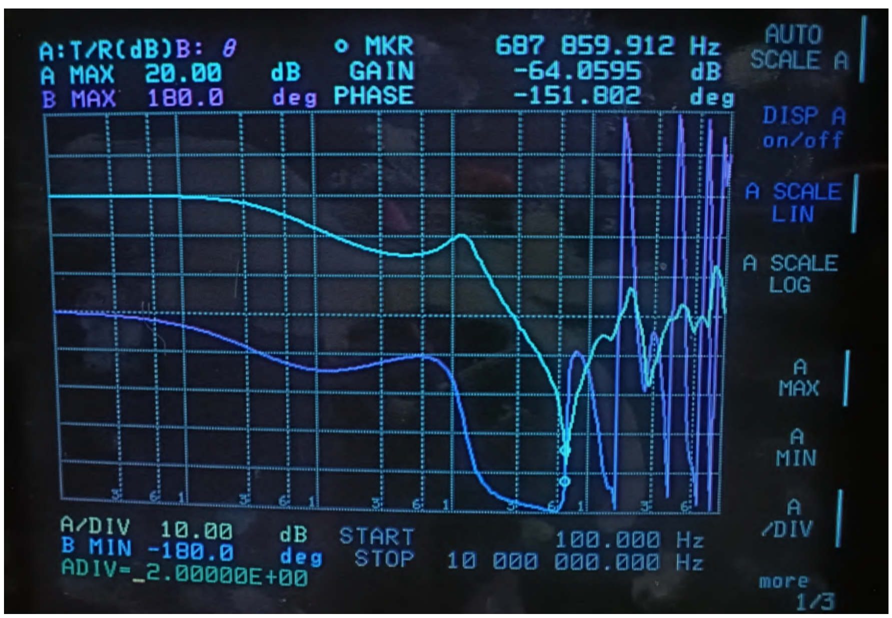

Figure 5.27: Frequency response of the complete system.

Chapter 6

Integration testing

6.1 Measurement setup

During the development activities for the new magnetic diagnostic system, the need arose to measure the effective area of the electromagnetic probes [22]. This parameter represents one of the main factors influencing the accuracy of magnetic measurements on RFX; an effort was therefore made to evaluate the precision with which this calibration could be performed using the available equipment.
The analyses were performed on the straight solenoid shown in 6.1, previously used for magnetic field tests, to achieve an accurate characterization of the field it generates, so that the device can be used as a reference source. This source has immediate application in the development of electromagnetic diagnostics, but may be of more general interest whenever it is necessary to produce a magnetic field known with high precision.
The solenoid must respect several requirements strictly linked to the magnetic probe to characterize:

- Ability to produce stationary fields with an intensity up to 10 mT;
- Ability to produce sinusoidal fields with an intensity up to 3 mT and a frequency up to 10 kHz;
- Uncertainty in the intensity of the produced field (both DC and AC) of less than 0.5 %;
- Uncertainty in the direction of the produced field of less than 0.1;
- A volume in which the field can be considered uniform spanning at least 5 cm in all three spatial directions.

The electrical and geometrical parameters of the solenoid are reported in table 6.1.

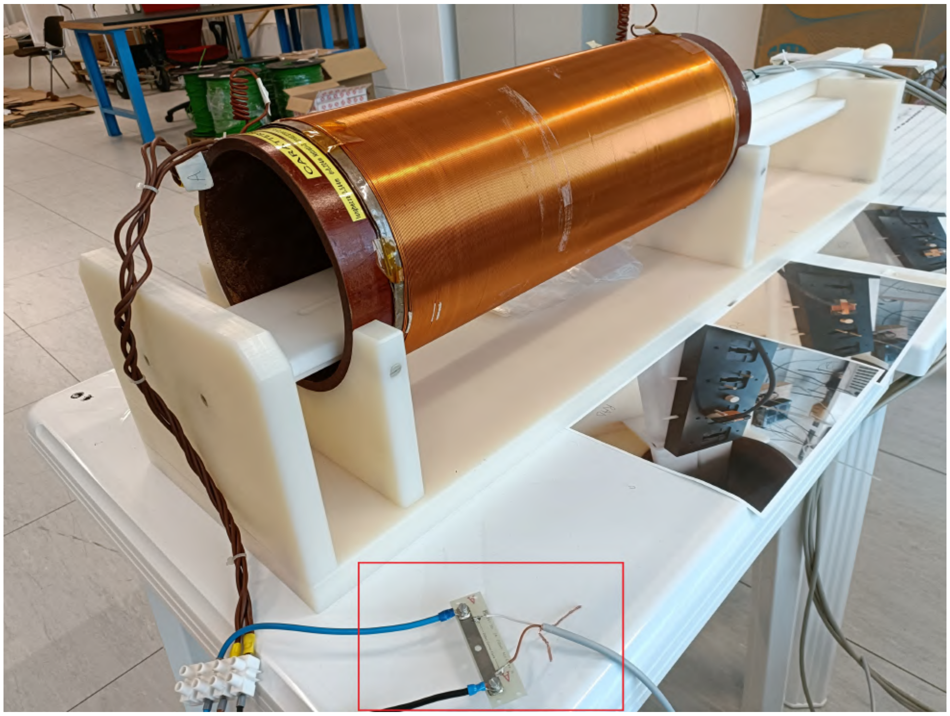

Figure 6.1: Straight solenoid used to generate a magnetic field for reference. Note that the shunt resistor highlighted in the red box is used to visualize the input waveform.

	Internal layer	Middle layer	External layer	Layers in series connection
Length $[mm]$	545	545	545	545
Wire diameter $[mm]$	1.2	1.2	1.2	1.2
Turns	453	453	453	1359
Coil Diameter $[mm]$	221.4	224.2	227	224.2
Series resistance $[\Omega]$	5.50	5.54	5.61	20.1
Series inductance $[mH]$	15.38	15.74	16.02	140.4
Shunt capacitance $[pF]$	66.8	72.4	84.1	4798
Resistance in DC $[\Omega]$	5.69	5.80	5.86	17.35

Table 6.1: Electrical and geometrical parameters of the copper solenoid.

The shunt capacitance takes into account the parasitic capacitance between the turns and in the connection cables.

In this thesis work, the device was used to test the operation and the reliability of the integrators by using the response of a magnetic sensor, immersed in the magnetic field generated by the solenoid. In order to visualize just one component at a time, a removable plastic support with four slots slides inside the solenoid. In this way each coil can be oriented in order to induce an electromotive force just across it, while the other two coils are still connected to the integrator. Of course, the cross-section of the coil to analyze must be orthogonal to the generated magnetic field.

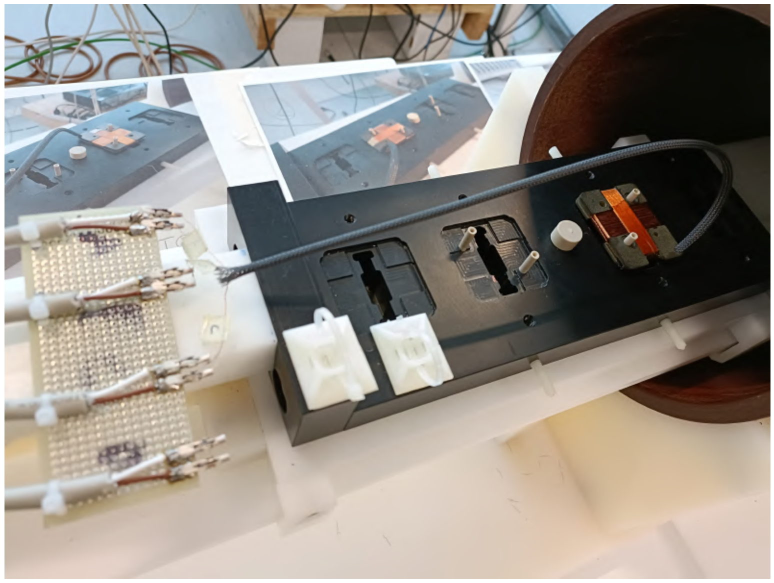

Figure 6.2: A magnetic sensor inserted in a slot of the removable plastic support.

Figure 6.3: The function generator CAENels used to supply the solenoid.

The instrument used to supply the solenoid was the CAENels FAST-PS-1K5 15-100 programmable power supply, shown in 6.3. It is substantially an independent current or voltage-controlled digital bipolar power supply module that can supply up to 1.5 kW (± 15 A and ± 100 V) [23]. The control board houses a dedicated FPGA and the SFP-ports are directly connected to the FPGA logic, allowing a very high update rate of the setpoint, giving the user more flexibility and excellent rates for the digital control of the power supply. The power supply can work both in local or remote mode, via Ethernet interface. The current or voltage setting of the unit can also be performed in four different modes from its dedicated software:

- **normal**: the update of the set-point is performed as soon as a new set-point is received via the remote, local or fast interfaces;
- **waveform**: the update of the set-point is performed on a specific timing;
- **trigger**: the set-point is updated by an external event coming from the rear BNC connector;
- **analog input**: the unit is controlled by an external signal that is fed to the rear BNC connector. The unit acts as a constant current or constant voltage generator.

6.2 Signal visualization

The control of the programmable power supply is performed from its dedicated online software. The device (which must be in remote mode) can be activated and deactivated from here. The electrical quantities supplied (voltage, current and power) are measured and reported in real time, while the waveform can be visualized by means of an internal oscilloscope. Each working mode can be selected from here and, furthermore, faults and diagnostics are reported on a dedicated section. A screenshot of the environment is provided in 6.4.

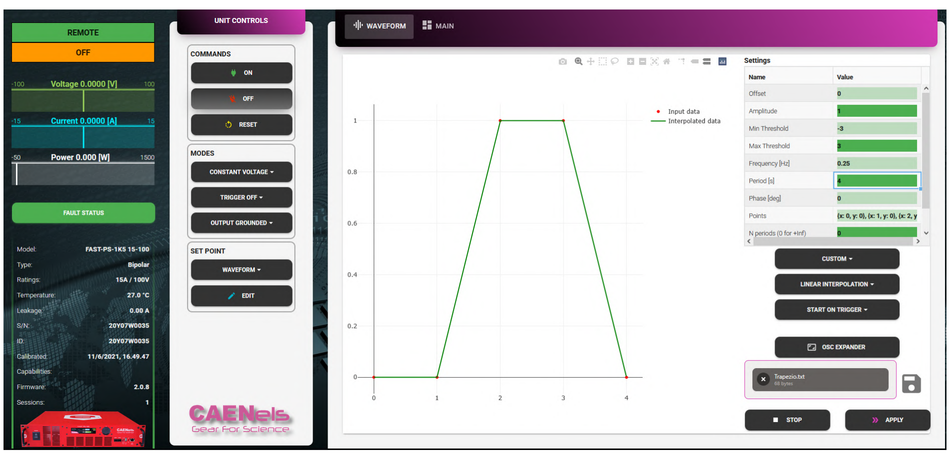

Figure 6.4: CAENels dedicated software environment.

The current or voltage waveform can be selected by uploading a text file with the cartesian coordinates (time and quantity) of the desired shape. In order to test the sensors, a trapezoidal periodic waveform with 5 V maximum value was selected, as shown in 6.4, so, knowing that the inductive sensors produce a voltage signal proportional to the rate of change of the magnetic flux, a square wave signal is expected as output (in other words, the time derivative of the trapezoidal waveform).
The device can be controlled automatically with command lines in a dedicated section of the software, although, in this thesis, it was preferred to develop a stand-alone Python script that controls autonomously the activation and deactivation of the supply, the voltage waveform (the supply is in

constant voltage mode) and plots it together with the three integrator outputs (the scripts are provided in B).

The applied waveform can be visualized by measuring the voltage drop produced by the current flowing through a 2 $A/200\ mV$ shunt resistance and then plotted by the script as reference.

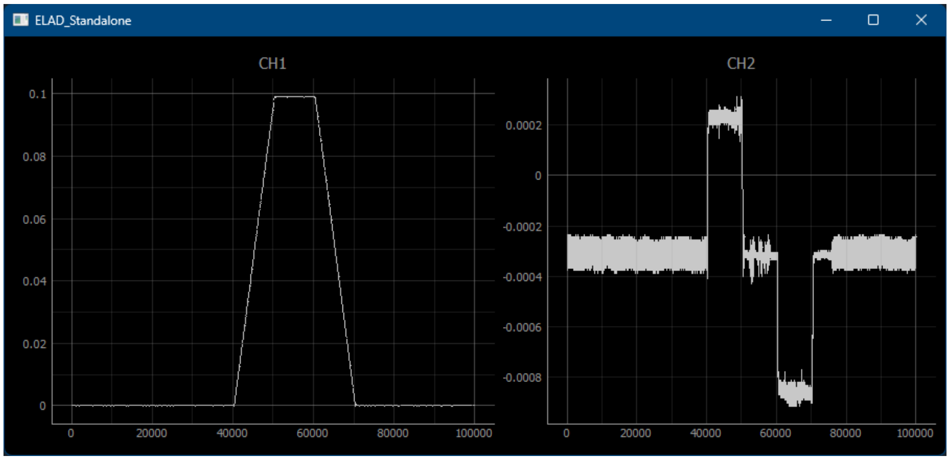

Figure 6.5: On the left the input signal obtained from the shunt resistor, on the right the induced electromotive force across the sensor.

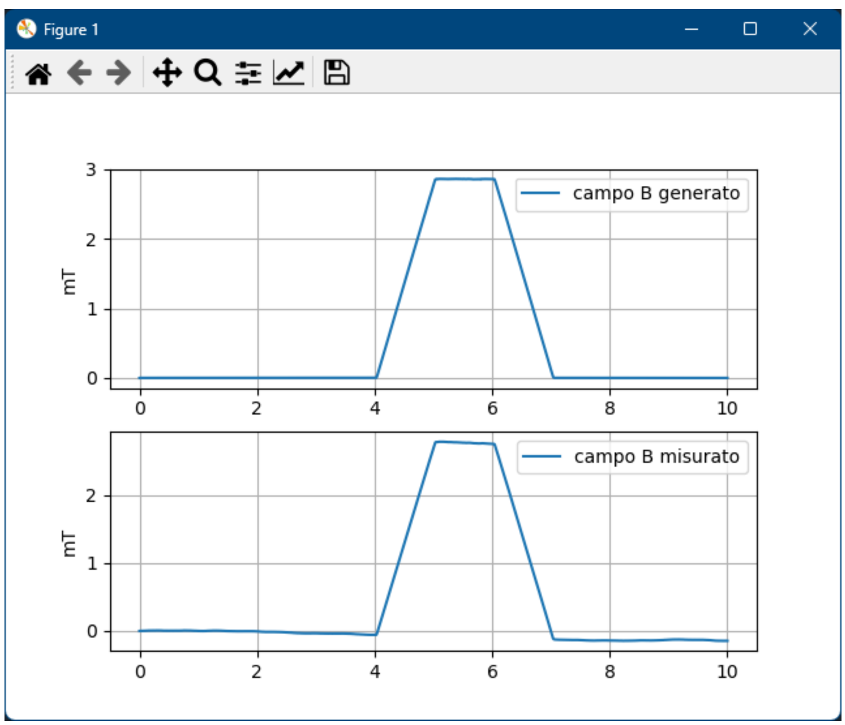

Figure 6.6: The integrated signal is similar to the generated one. Note that the drifts are modest, thanks to the implementation of the numerical integration.

Chapter 7

Conclusions

In this dissertation, the upgraded magnetic diagnostic system installed on the RFX-mod2 experiment and its signal acquisition system were analyzed, with particular attention to the pick-up coil probes, their transmission lines, adapter circuits for each magnetic component and the newly adopted digital integrators.

Concerning the digital integration device, the new design offers technical advantages because it significantly reduces the overall size of the system, makes signals available for real-time control of the RFX-mod2 experiment, and eliminates the calibrations required by the analog integrator system. From a measurement standpoint, the measurement bandwidth allows for new types of analysis on plasma instabilities, significantly reducing the noise level and electronic drifts. So, it is possible to achieve better integration performance for the acquired signals with the same characteristics as the previous analog integration system.

The characterization of the acquisition chain and the measure of the electrical parameters of the transmission cable were necessary to know at which frequency f_{cut} the reflection phenomena start to appear. Starting from the acquired data, the adapter circuit can be designed using the LTspice simulation software: this circuit ensures to match the acquisition line input impedance in order to reduce resonance peaks due to reflection phenomenon and obtain the required bandwidth. The attenuator circuit before the output (and so, connected directly to the integrator device) is required to obtain a signal with peaks inside an operational safe voltage range for the integrator electronics.

Finally, a real circuit for the adapter has been realized on a matrix board and the entire acquisition chain (magnetic sensor, transmission line, adapter circuit) impedance has been measured using the HP4194A analyzer: the expected results (in this case, for the toroidal and poloidal components) were obtained. However, reflection phenomena are still present at very high frequencies, introduced by the intrinsic characteristic impedance of the copper wire that composes the winding of the inductive sensor and, of course, the frequency-dependent behaviour of the characteristic impedance, considered constant in the simulations. To improve the model, a non-constant $Z_c(f)$ could be introduced in the transmission line model, via a behavioural element or a table interpolated from the data, in order to reproduce the experimentally observed frequency dependence more faithfully.

Appendix A

Effective cross-section of the coils

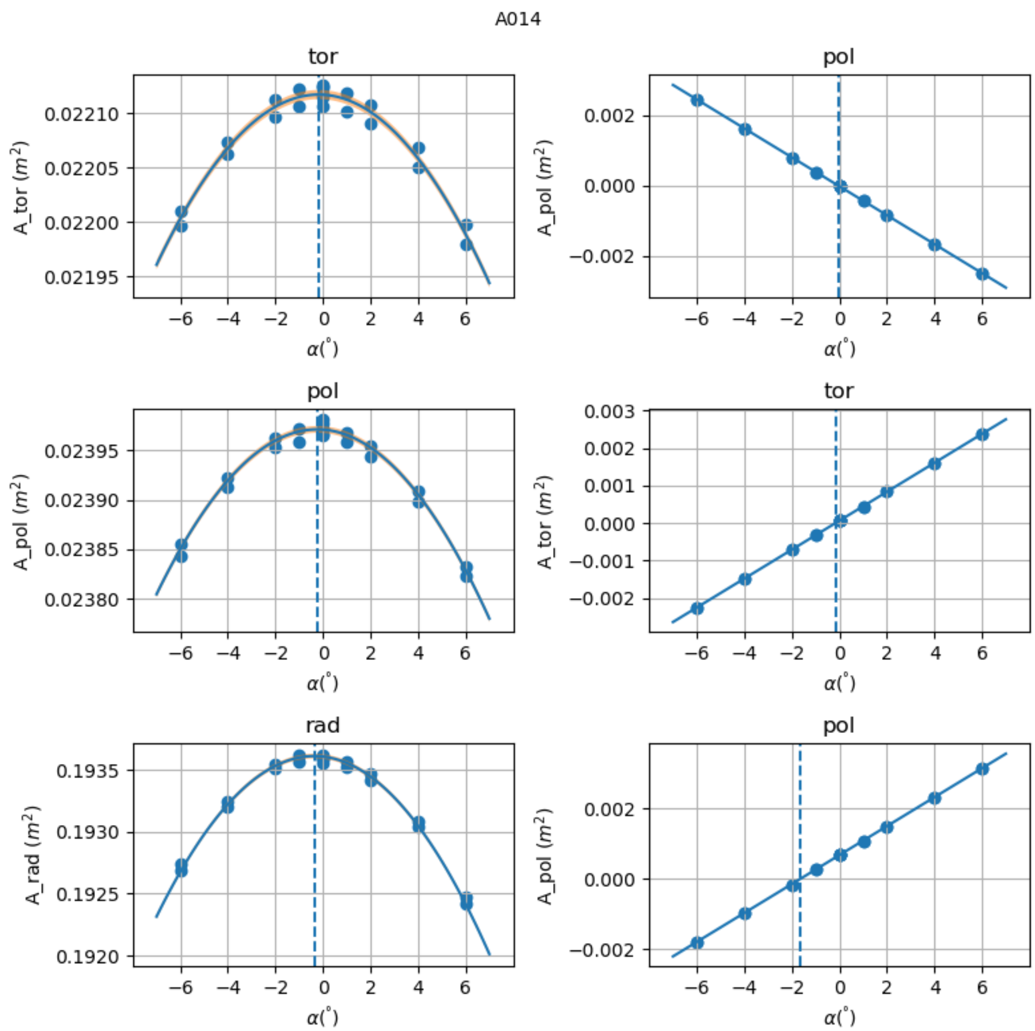

Figure A.1: Effective cross-section of the coils in function of the angle between the axis orthogonal to the coil area and the longitudinal axis of the measuring coil (respectively toroidal, poloidal and radial, from top to bottom).

Winding	Area $[m^2]$	Minimum value $[mH]$	Maximum value $[mH]$	Measured value $[mH]$
Radial	0.193611	2.09	2.21	2.14
Poloidal	0.023971	0.227	0.241	0.230
Toroidal	0.022117	0.184	0.195	0.187

Table A.1: Inductance values for each coil of the sensor.

Appendix B

Stand-alone scripts for the power supply control

The program used to plot the integration results is divided into three different Python scripts:

- the main script "acq_mag_test_ps.py", it recalls the stand-alone scripts, then it plots the integration result;

```
import pyqtgraph as pg
import numpy as np
from time import sleep
from PyQt5.QtWidgets import QApplication

from ELAD_Standalone import ELAD_Standalone
from CAENelsDevice import CAENelsDevice

# ---------------------------------------------------

elad = ELAD_Standalone( ip="192.168.72.12", port=8888 ) # Use your hardware IP
caen = CAENelsDevice( ip_address="192.168.72.77" )

# 2. Modify parameters before connecting
elad.pts = 110_000
elad.tr_freq_div = 100
elad.tr_cic_ena = 'YES'
elad.chan_lh_mode[0] = 1 # Set Channel 1 to LH Mode = 1
elad.chan_lh_mode[1] = 0 # Set Channel 1 to LH Mode = 1
elad.chan_lh_mode[2] = 0 # Set Channel 1 to LH Mode = 1
elad.chan_lh_mode[3] = 1 # Set Channel 1 to LH Mode = 1
elad.chan_lh_mode[4] = 0 # Set Channel 1 to LH Mode = 1 Low=0 (+-5V), High=1
```

```
                                          (+-10V)

fs0 = 1E6
fs = fs0/elad.tr_freq_div
dt = 1/fs
acq_window = elad.pts*dt

Vset = 6.2  # 6V ~1 mT
V_sr = Vset # slew rate in tensione
I_sr = Vset / 10 # slew rate in corrente, Rcoil e' 17 ohm la uso come
                                          protezione

cmd = f"MSRV:{V_sr:.2f}"
caen.send_cmd( cmd )
cmd = f"MSRI:{I_sr:.2f}"
caen.send_cmd( cmd )
t1 = 5.0 + 1.0
t2 = 2.0
try:
# 3. Connect, Arm, and Trigger
elad.connect()
elad.arm()

caen.send_cmd('LOOP:V')
caen.send_cmd('UPMODE:NORMAL')
caen.send_cmd('MON')
caen.send_cmd('MWV:0.0')


sleep( 0.5 )

elad.trigger()
print( f"acquiring for {acq_window:.1f} sec ... ")
sleep( t1 ) # Wait for transient buffer to fill
cmd = f"MWVR:{Vset:.2f}"
caen.send_cmd( cmd )
sleep( t2 ) # Wait for transient buffer to fill
cmd = f"MWVR:0.0"
caen.send_cmd( cmd )

sleep( 0.5 + acq_window - t1 - t2 ) # Wait for transient buffer to fill

caen.send_cmd('MOFF')
```

```
# 4. Fetch the data natively
print( "getting data ... ")
result = elad.get_acq_data()

print("\nAcquisition Complete:")
print(f"Time Axis Shape: {result['time'].shape}")
print(f"Channel 1 Data Length: {len(result['data'][0])}")
# print(f"Channel 1 Volts (first 5): {result['data'][0][:5]}")
print(f"Status Array: {result['status']}")
print(f"Autozero Sums: {result['autozero']}")

except Exception as e:
print(f"Error during acquisition: {e}")
finally:
elad.close()

# --------------------------------------------------
k_shunt_cal = 0.1144 / 0.01149542
k_Bref = 3 * 0.96421E-3  # Tesla / A

# --------------------------------------------------

d = np.transpose( np.asarray( result['data'] ) )
t = result['time']

channels = [1,2,3,4,5]

win = pg.GraphicsLayoutWidget(show=True, title="ELAD")
win.resize(900,600)
win.setWindowTitle('ELAD_Standalone')

# Enable antialiasing for prettier plots
# pg.setConfigOptions(antialias=True)

plots = []
# np = 0
for ch in channels :
row = (ch-1) // 3; col = (ch-1) %  3
pl = win.addPlot( row=row, col=col, title=f"CH{ch}" )
pl.setXRange( 0,5000, padding=0)
pl.setYRange( -1000000,1000000, padding=0)
pl.enableAutoRange('xy', True )
```

```
pl.showGrid( x=True , y=True )
plots.append( pl )
# np = np + 1



# pw.plot( data , clear=True)


for ch , pl in zip( channels , plots ) :
# pl.plot( d[::10,ch-1], clear=True)
pl.plot( d[:,ch-1], clear=True)

QApplication.processEvents()





import matplotlib.pyplot as plt


Bref = d[:,0]*k_shunt_cal*k_Bref
s = d[:,3]
nz = 10000
z = np.mean( s[0:nz] )
si = np.cumsum( s-z ) * dt
#As = 0.193611
As = -0.022117

Bmis = si / As
fig = plt.figure( 1 )
fig.clf()
ax = fig.add_subplot(211)
ax.plot( t-1, Bref*1E3, label='Bref' )
ax.grid()
ax.set_ylabel( 'mT')

ax = fig.add_subplot(212)
ax.plot( t-1, Bmis*1E3 )
ax.grid()
ax.set_ylabel( 'mT')
ax.set_xlabel( 's')
```

- “CAENelsDevice.py”, the stand-alone script for the CAEN supply;

```
import socket
```

```python
class CAENelsDevice:
"""
A class to manage communication with CAENels units over TCP/IP.
"""
def __init__(self, ip_address="192.168.72.77", port=10001, timeout=2.0):
self.ip_address = ip_address
self.port = port
self.timeout = timeout

def send_cmd(self, cmd, echo_response=True):
"""
Sends a command to the device and returns the response.
"""
try:
# Using 'with' ensures the socket is closed automatically after the block
with socket.socket(socket.AF_INET, socket.SOCK_STREAM) as s:
s.settimeout(self.timeout)
s.connect((self.ip_address, self.port))

# Commands must be terminated with a Carriage Return (\r)
full_cmd = f"{cmd}\r"
s.sendall(full_cmd.encode())

# Receive and decode the response
response = s.recv(1024).decode().strip()

if echo_response:
print(f"Response: {response}")

return response

except Exception as e:
error_msg = f"Error communicating with {self.ip_address}: {e}"
print(error_msg)
return error_msg

# --- Example Usage ---
if __name__ == "__main__":
# Initialize the device
device = CAENelsDevice(ip_address="192.168.72.77")

# Send a query command
```

```
ver = device.send_cmd("VER")

# Send a standard command
device.send_cmd("MON", echo_response=False)
```

- "ELAD_Standalone.py", the stand-alone script for the ELAD integrator.

```
import socket
import numpy as np
import time
from threading import Thread

def recvall(sock, n):
"""Helper function to recv n bytes or return None if EOF is hit"""
data = bytearray()
while len(data) < n:
packet = sock.recv(n - len(data))
if not packet:
return None
data.extend(packet)
return data



class ELAD_Standalone:
def __init__(self, ip="127.0.0.1", port=8000):
# Network settings
self.ip = ip
self.port = port
self.sock = None

# General Acquisition Parameters (Defaults mimic MDSplus parts list)
self.pts = 1000
self.freq_div = 10000
self.autozero_tim = 2.0
self.act_chans = 12
self.calibration = 'NO'
self.chop_ena = 'NO'
self.clock_mode = 'INTERNAL'
self.cic_enabled = 'NO'

# Trigger Modes
self.trg_mod = 'INTERNAL'
```

```
self.trg_ev = 0
self.trg_tim = 0.0
self.strg_mod = 'INTERNAL'
self.strg_ev = 0
self.atrg_mod = 'INTERNAL'
self.atrg_ev = 0

# Transient specific
self.tr_freq_div = 1
self.tr_cic_ena = 'NO'

# Streaming specific
self.stream_mode = 'UDP'
self.stream_ip = socket.gethostbyname(socket.gethostname())
self.stream_port = 8111

# Channel specific lists (Index 0 is Channel 1, etc.)
self.chan_lh_mode = [0] * 12
self.chan_chop_ena = [0] * 12
self.chan_stream_on = [True] * 12
self.chan_strint_on = [True] * 12

# Runtime Info
self.fpga_ver = ""
self.chan_id = [""] * 12
self.chan_eprom = [""] * 12

# Threading controls
self.stop_acq = False
self.worker_thread = None

def connect(self):
"""Initializes connection and sends configuration to hardware"""
trigModeDict = {'INTERNAL': 0, 'HW_LOCAL': 1, 'EVENT': 2, 'HW_GLOBAL': 3}
streamTrigModeDict = {'INTERNAL': 0, 'EVENT': 1}
autozeroTrigModeDict = {'INTERNAL': 0, 'EVENT': 1}
clockModeDict = {'INTERNAL': 0, 'HW_LOCAL': 1, 'HIGHWAY': 2, 'HW_GLOBAL': 2}
cicEnabledDict = {'YES': 1, 'NO': 0}

trigMode = trigModeDict.get(self.trg_mod, 0)
streamTrigMode = streamTrigModeDict.get(self.strg_mod, 0)
autozeroTrigMode = autozeroTrigModeDict.get(self.atrg_mod, 0)
clockMode = clockModeDict.get(self.clock_mode, 0)
```

```
cicEnabled = cicEnabledDict.get(self.cic_enabled, 0)
trCicEnabled = 0 if self.tr_freq_div == 1 else cicEnabledDict.get(self.
                                        tr_cic_ena, 0)

# Build hardware mode register
modeReg = int(0)
chopActive = False
globalChopEnable = (self.chop_ena == 'YES')

for chan in range(12):
if globalChopEnable and self.chan_chop_ena[chan] > 0:
modeReg |= (1 << (chan+1))
chopActive = True
if self.chan_lh_mode[chan] > 0:
modeReg |= (1 << (chan+16))

if chopActive:
modeReg |= 1
if self.calibration == 'YES':
modeReg |= (1 << 30)

print(f"Connecting to {self.ip}:{self.port}....")
self.sock = socket.socket(socket.AF_INET, socket.SOCK_STREAM)
self.sock.connect((self.ip, self.port))

# Send configuration sequence
self._send_cmd(b'CHK', 1)
self._send_cmd(b'PTS', self.pts)
self._send_cmd(b'DIV', self.freq_div)
self._send_cmd(b'TIV', self.tr_freq_div)

autoTicks = np.int32(self.autozero_tim * 1000)
self._send_cmd(b'AUT', autoTicks)

# IPP command requires a specific byte structure
self.sock.send(b'IPP')
ipLen = np.int32(len(self.stream_ip))
self.sock.send(ipLen.item().to_bytes(4, 'little'))
self.sock.send(bytes(self.stream_ip, 'utf-8'))
self.sock.send(np.int32(self.stream_port).item().to_bytes(4, 'little'))
print("IPP Reply:", self.sock.recv(2).decode(errors='ignore'))

self._send_cmd(b'TEX', trigMode)
```

```
if trigMode == 2:
self._send_cmd(b'EVT', self.trg_ev)

self._send_cmd(b'SEX', streamTrigMode)
if streamTrigMode == 1:
self._send_cmd(b'EVS', self.strg_ev)

self._send_cmd(b'TAU', autozeroTrigMode)
if autozeroTrigMode == 1:
self._send_cmd(b'EVA', self.atrg_ev)

self._send_cmd(b'CEX', clockMode)
self._send_cmd(b'CIC', cicEnabled)
self._send_cmd(b'TIC', trCicEnabled)
self._send_cmd(b'MOD', modeReg)

# Read EPROM IDs and FPGA Version
self.sock.send(b'IDS')
ids_buffer = recvall(self.sock, 16 * 12 + 32 * 12 + 8)
ids = np.frombuffer(ids_buffer, dtype=np.int8)

for chan in range(12):
c_id = "".join([chr(c) for c in ids[(chan*(16+32)):(chan*(16+32))+16]]).strip('\x00')
c_eprom = "".join([chr(c) for c in ids[(chan*(16+32))+16:(chan*(16+32))+16+32]]).strip('\x00')
self.chan_id[chan] = c_id
self.chan_eprom[chan] = c_eprom
# print(f"Chan {chan+1} - ID: {c_id}, EPROM: {c_eprom}")

fpga_str = "".join([chr(c) for c in ids[(12*(16+32)):]]).strip('\x00')
self.fpga_ver = fpga_str
print(f"FPGA Version: {self.fpga_ver}")

def _send_cmd(self, cmd, val):
"""Helper to send a standard 3-byte command followed by a 4-byte little-endian int"""
self.sock.send(cmd)
val_int = np.int32(val)
self.sock.send(val_int.item().to_bytes(4, 'little'))
reply = self.sock.recv(2)
print(f"{cmd.decode()} Reply: {reply.decode(errors='ignore')}")
```

```
def arm(self):
self.sock.send(b'ARM')
print("ARM Reply:", self.sock.recv(2).decode(errors='ignore'))

def trigger(self):
self.sock.send(b'TRG')
print("TRG Reply:", self.sock.recv(2).decode(errors='ignore'))

def autozero_trigger(self):
self.sock.send(b'TRS')
print("TRS Reply:", self.sock.recv(2).decode(errors='ignore'))

def get_acq_data(self):
"""Retrieves transient data, equivalent to the MDSplus store() action"""
if self.tr_cic_ena == 'YES':
rightBits = np.round(np.log2(np.power(self.tr_freq_div, 3)))
cicCorrection = np.power(2, rightBits) / np.power(self.tr_freq_div, 3)
else:
cicCorrection = 1

self.sock.send(b'STA')
statusReg = int.from_bytes(self.sock.recv(4), 'little')
activeChans = statusReg & 0x0000000F
self.act_chans = activeChans

chan_status = []
for chan in range(12):
chan_status.append("ERROR" if (statusReg & (1 << (4+chan)) > 0) else "OK")

self.sock.send(b'STR')
numSamples = int.from_bytes(self.sock.recv(4), 'little')
numChanSamples = int(numSamples / activeChans)

dma_buffer = recvall(self.sock, 4 * numSamples)
dmaSamples = np.frombuffer(dma_buffer, dtype=np.int32)

channel_data_volts = []

# Demultiplex, apply CIC, and scale to Volts
for chan in range(activeChans):
chan_raw = dmaSamples[chan::activeChans] * cicCorrection
scale_factor = 5E-6 if self.chan_lh_mode[chan] > 0 else 1E-5
chan_volts = chan_raw * scale_factor
```

```
channel_data_volts.append(chan_volts)

# Read Autozero sums
self.sock.send(b'CAU')
autozeroSums = []
for chan in range(activeChans):
autozeroSums.append(int.from_bytes(self.sock.recv(4), 'little'))

# Create timebase array natively
dt = 1E-6 * self.tr_freq_div
time_array = self.trg_tim + (np.arange(numChanSamples) * dt)

return {
  "time": time_array,
  "data": channel_data_volts,  # List of numpy arrays in Volts
  "status": chan_status,
  "autozero": autozeroSums
}

# ============================================================
# ASYNCHRONOUS STREAMING METHODS (Optional for standalone testing)
# ============================================================

def start_stream(self, callback_func=None):
"""Starts streaming and pushes chunks to callback_func(start_time, end_time,
                                        data_arrays)"""
self.stop_acq = False
if self.stream_mode == 'UDP':
self.worker_thread = Thread(target=self._udp_stream_worker, args=(
                                        callback_func,), daemon=True)
else:
self.worker_thread = Thread(target=self._tcp_stream_worker, args=(
                                        callback_func,), daemon=True)

self.worker_thread.start()
time.sleep(0.5)

self.sock.send(b'STS')
print("STS Reply:", self.sock.recv(2).decode(errors='ignore'))

def stop_stream(self):
self.stop_acq = True
self.sock.send(b'STO')
```

```
print("STO Reply:", self.sock.recv(2).decode(errors='ignore'))

def _udp_stream_worker(self, callback):
stream_sock = socket.socket(socket.AF_INET, socket.SOCK_DGRAM, socket.
                                        IPPROTO_UDP)
stream_sock.setsockopt(socket.SOL_SOCKET, socket.SO_REUSEADDR, 1)
stream_sock.bind(('', self.stream_port))

# Omitted full worker translation for brevity, but you would replace MDSplus
# makeSegment calls with `if callback: callback(startTime, endTime,
                                        convertedData)`
print("UDP Stream listener running (Standalone callback mode pending)...")
# ... logic mirrors AsynchStoreUdp from v2

def _tcp_stream_worker(self, callback):
# Implementation mirrors AsynchStoreTcp, passing arrays to callback
print("TCP Stream listener running (Standalone callback mode pending)...")
pass

def close(self):
if self.sock:
self.sock.close()
self.sock = None


if __name__ == "__main__":
print("Initializing standalone ELAD v2 driver...")

# 1. Instantiate
elad = ELAD_Standalone(ip="192.168.162.12", port=8888 ) # Use your hardware IP

# 2. Modify parameters before connecting
elad.pts = 5000
elad.tr_freq_div = 2
elad.chan_lh_mode[0] = 1 # Set Channel 1 to LH Mode = 1

try:
# 3. Connect, Arm, and Trigger
elad.connect()
elad.arm()
elad.trigger()
time.sleep(0.5) # Wait for transient buffer to fill
```

```
# 4. Fetch the data natively
result = elad.get_acq_data()

print("\nAcquisition Complete:")
print(f"Time Axis Shape: {result['time'].shape}")
print(f"Channel 1 Data Length: {len(result['data'][0])}")
print(f"Channel 1 Volts (first 5): {result['data'][0][:5]}")
print(f"Status Array: {result['status']}")
print(f"Autozero Sums: {result['autozero']}")

except Exception as e:
print(f"Error during acquisition: {e}")
finally:
elad.close()
```

Acknowledgments

Anyone who knows me will certainly know that I'm not a very extroverted person and that writing these words isn't easy for me, but *in primis* I would like to thank my entire family (Mama, Tata, Papino, ...) for their constant support throughout all these years of hard work, with a special thought for my Nonna Luisa.

Next, I want to thank the whole "*Big Boyz Crew*", my family of friends and "drinking team": we've been through so much together, and tonight we'll raise our glasses to the sky to toast this milestone.

Thank you to "*No Hiding Place*", my band, for all the gigs and shenanigans we made together: touring through the deepest Balkans with you was absolutely lit!

I'd like to thank my university classmates for all the mutual help.

Best wishes as well to Gaia, who is also on the home stretch toward her much-coveted bachelor's degree.

I thank Ing. Nicolò Marconato for giving me the opportunity to work on this thesis, and Dott. Roberto Cavazzana along with the entire "*Consorzio RFX*": I would have been completely lost without your help.

And I also want to thank you, R., you are so important to me and you are truly a part of my life. You know very well that I could never hate you.

Gianluca, 11/09/2026

Bibliography

[1] M. A. Lieberman and A. J. Lichtenberg, *Principles of plasma discharges and materials processing.* John Wiley & Sons, 2024.

[2] G. Pucella and S. E. Segre, *Fisica dei Plasmi.* Zanichelli, 2010.

[3] G. Zollino and G. Chitarin, “Nuclear fission and fusion plants,” 2026.

[4] T. J. M. Boyd and J. J. Sanderson, *The physics of plasmas.* Cambridge university press, 2003.

[5] S. E. Wurzel and S. C. Hsu, “Continuing progress toward fusion energy breakeven and gain as measured against the lawson criteria,” *Physics of Plasmas*, vol. 32, no. 11, 2025.

[6] J. Wesson and D. J. Campbell, *Tokamaks.* Oxford university press, 2011, vol. 149.

[7] P. Zanca and D. Terranova, “Reconstruction of the magnetic perturbation in a toroidal reversed field pinch,” *Plasma physics and controlled fusion*, vol. 46, no. 7, pp. 1115–1141, 2004.

[8] B. P. van Milligen, “Analysis of equilibrium and topology of tokamak plasmas,” Rijksuniversiteit Utrecht (Netherlands), Tech. Rep., 1991.

[9] D. A. Daniel, “Derivation and applications of grad-shafranov equation in magnetohydrodynamics (mhd),” *Quest Journals*, vol. 7, no. 4, pp. 34–38, 2021.

[10] S. Zheng, A. Wootton, and E. Solano, “A tokamak equilibrium with arbitrary aspect ratio,” University of Austin, Chinese Academy of Sciences of Beijing, Tech. Rep., 1995.

[11] E. Ramsden, *Hall-effect sensors: theory and application.* Elsevier, 2011.

[12] N. Marconato, R. Cavazzana, P. Bettini, and A. Rigoni, “Accurate magnetic sensor system integrated design,” *Sensors*, vol. 20, no. 10, p. 2929, 2020.

[13] M. H. Samimi, A. Mahari, M. A. Farahnakian, and H. Mohseni, “The rogowski coil principles and applications: A review,” *IEEE Sensors Journal*, vol. 15, no. 2, pp. 651–658, 2014.

[14] A. Wootton, "Magnetic fields and magnetic diagnostics for tokamak plasmas," *Pvt Rep*, vol. 64, 2012.

[15] D. Abate, N. Marconato, and R. Cavazzana, "Specifica tecnica per la realizzazione degli avvolgimenti dei sensori magnetici pick-up coils per rfx-mod2," Consorzio RFX, Tech. Rep., 2021.

[16] *Zero-Drift Amplifiers: Features and Benefits*, Texas Instruments, 2022.

[17] R. Cavazzana, A. Rigoni, and G. Manduchi, "Requisiti tecnici per il sistema di acquisizione diretta e integrazione digitale per le misure magnetiche di rfx-mod2," Consorzio RFX, Tech. Rep., 2021.

[18] R. Benato, *Basics of Power Systems Transmission*. Independently published, 2024.

[19] M. Guarnieri *et al.*, *Elettrotecnica circuitale*. Webster srl, 2017, vol. 1.

[20] D. Abate, "Calcolo e misura di induttanza dei flux-loops in rfx-mod2," Consorzio RFX, Tech. Rep., 2026.

[21] *LCR-6000 Series User's Manual*, GW Instek, 2024.

[22] N. Pomaro, P. Fiorentin, S. Peruzzo, and L. Grando, "Messa a punto di una sorgente di riferimento di campo magnetico," Consorzio RFX, Tech. Rep., 2001.

[23] *FAST-PS-1K5 User's Manual*, CAENels, 2025.